Single-Molecule Investigations of Enzyme Dynamics: RecBCD Helicase Motion and *glmS* Ribozyme Cleavage

by

Martha Hosotani

B.A., University of California at Berkeley, 2004

M.S., University of Colorado at Boulder, 2007

A thesis submitted to the

Faculty of the Graduate School of the

University of Colorado in partial fulfillment

of the requirements for the degree of

Doctor of Philosophy

Department of Physics

2011

ProQuest LLC
789 East Eisenhower Parkway
P.O. Box 1346
Ann Arbor, MI 48106-1346

This thesis entitled:
Single-Molecule Investigations of Enzyme Dynamics: RecBCD Helicase Motion and *glmS* Ribozyme Cleavage
written by Martha Hosotani
has been approved for the Department of Physics

Thomas T. Perkins

Matthew A. Glaser

Date

The final copy of this thesis has been examined by the signatories, and we find that both the content and the form meet acceptable presentation standards of scholarly work in the above mentioned discipline.

Hosotani, Martha (Ph.D., Physics)

Single-Molecule Investigations of Enzyme Dynamics: RecBCD Helicase Motion and *glmS* Ribozyme Cleavage

Thesis directed by Professor Thomas T. Perkins

Enzyme dynamics are a critical factor in enzyme function. Probing individual enzymes and enzymatic systems elucidates the mechanistic basis of their dynamics. Here, with two distinct single-molecule, biophysical approaches, we examine two particular enzymatic systems.

RecBCD is a multifunctional enzyme that repairs double-stranded DNA breaks and degrades unwanted DNA in *Escherichia coli*. To probe how this superfamily-1 helicase couples ATP binding and hydrolysis to unwind and directionally translocate along double-stranded DNA, we used optical tweezers featuring 1-base-pair resolution ($\Delta f = 0.1$–2.3 Hz, $F = 6$ pN) to directly measure interactions between single RecBCD helicases and their DNA substrate. Surprisingly, the RecBCD·DNA complex exhibited large, multi-base-pair conformational dynamics (4.4 ± 0.3 bp, mean $\pm\ \sigma_{\bar{x}}$, $\Delta f =$ 0.1–10 Hz) that were present both between unwinding steps and in the complete absence of ATP. To understand the origin of the conformational dynamics, we made three observations. First, the onset of the conformational dynamics depended on 5′-ssDNA length, which interacts with the RecD motor, and were consistent with the onset of helicase activity, as established in prior biochemical studies. Second, conformational dynamics of RecBCD bound to a cross-linked DNA construct were suppressed, indicating that the RecBCD "pin," which interacts with the junction, undergoes rapid back-and-forth translocation along the DNA. Third, conformational dynamics were reduced in the presence of nonhydrolyzable ATP analogs. These results indicate that when RecD is engaged RecBCD actively destabilizes the duplex, and that these conformational dynamics are modulated by the nucleotide-bound state of the enzyme. These studies signify the first real-time measurements of previously-unseen destabilization dynamics of the DNA duplex by RecBCD and provide insight into the unwinding mechanism of superfamily-1 helicases.

In the effort to develop highly-sensitive biosensors for medical diagnostics, environmental monitoring, and industrial quality control, nucleic-acid-based biosensors offer a number of competitive advantages over antibodies for sensing applications. We explored a naturally-occurring biosensor, the *glmS* ribozyme, a RNA molecule that has the remarkable ability to recognize a specific metabolite, catalyze self-cleavage upon its binding, and regulate gene expression. We developed a new, single-molecule assay to detect individual *glmS* ribozyme cleavage events with video microscopy that can be generalized to other nucleic-acid-based biosensors.

Dedication

I would like to dedicate this dissertation to my sister, my mother, and my father.

Acknowledgements

I would like to thank my Thesis Advisor, Professor Thomas T. Perkins, without whom this work would not have been possible. I greatly appreciate his many contributions, which have been instrumental in the single-molecule biophysics projects presented in this dissertation. His knowledge has been of great resource throughout the years during which I have had the opportunity to work with him.

I would also like to thank the many people with whom I have had the opportunity of working directly and indirectly, for sharing experimental techniques and methods, partaking in helpful scientific discussion, and contributing to a positive research environment. I would like to thank Collaborators: Hung-Wen Li, Hsiu-Fang (Bendy) Fan, Christopher J. Wilds, Anne M. Noronha, and Robert T. Batey; Postdoctoral Researchers: Yeonee Seol, Gavin M. King, D. Hern Paik, Rebecca K. Montange, and Ruby M. A. Sullan; Graduate Students: Amanda E. Carpenter, Ashley R. Carter, Justin A. Kuczynski, and Allison B. Churnside; Professional Research Assistant: Wayne A. Halsey; and Undergraduate Students: Andrew Leifer, Louisa Eberle, George A. Emanuel, Duc Minh Nguyen, and Matthew S. Bull. I would like to thank Hung-Wen and Bendy, for characterizing and providing biotinylated RecBCD enzymes; Chris and Anne, for synthesizing the cross-linked DNA constructs; Rob, for training and guidance on the *glmS* ribozyme project; Ashley, for introducing the RecBCD optical-trapping assay and analysis methods to me, making time not only to work side-by-side on the RecBCD project through numerous late nights, but also to engage in invigorating, memorable experiences together outside of the lab; Amanda, for training me on trapping instrumentation, programming, and surface-chemistry technique, helping me with innu-

merable scientific details, and for sharing her perceptive and sincere insight in both lighthearted and thought-provoking interactions; Wayne, for teaching his excellent biochemical technique as well as sharing his goofy sense of humor and conscientious perspective; Yeonee, for sharing her RNA-assay-development knowledge, her scientific expertise, and her kind encouragement; Justin, for engaging in intellectual debate, entertaining banter, and frank discussion; Gavin, for sharing his sense of the big picture and open demeanor; Hern, for sharing his great knowledge of science, sports, and fine cuisine; and Allison, Andy, Louisa, George, Rebecca, Duc, Ruby, and Matt, for sharing their technical knowledge and good-natured, friendly energy.

The members of the JILA shops and staff have added to the technical success of this work as well as to an upbeat working environment. I would like to thank the JILA Instrument Specialists, with special thanks to David Alchenberger, for his substantial assistance in the nanofabrication processes required in our experiments, and Blaine P. Horner, Hans Greene, and Thomas P. Foote, for their work building various parts for the apparatuses used in the experiments; the JILA Electronics Shop, with thanks to Carl J. Sauer, James Fung-A-Fat, and Terry J. Brown; the JILA Computing Staff, with thanks to James D. McKown, Michael D. Paige, and James R. Raith; the JILA Supply Office, with special thanks to Jeffrey J. Sauter, Brian C. Lynch, Randall T. Holliness, and David C. Errickson; the JILA Scientific Reports Office; and the JILA Administrative Staff, with additional thanks to Agnieszka K. Lynch and Maryly L. Dole.

I would also like to thank the director and deputy directors of the NSF-IGERT Optical Science and Engineering Program, Dana Z. Anderson, Barbara Tennis, and Ricki W. Hadow. OSEP not only provided a source of funding for this work, but additionally provided opportunities for my expanded learning and training in research, including opportunities such as an internship at Nikon Instruments in Japan and extended coursework in an array of topics.

I would like to offer my deepest thanks to my Thesis Committee: Amy E. Palmer, John P. Cumalat, Margaret M. Murnane, Matthew A. Glaser, Meredith D. Betterton, and Thomas T. Perkins. Thank you so much for supporting me in this work.

Many friends I made before and during graduate school have influenced and enhanced my

doctoral experience: Ben Zhao, Elisa K. Berry, Nguyen Hoang, Holly A. Magdanz, Peter Bell, Laura Horovitz Strashny, Heriberto Vargas, Terence ManChun Tong, Chul-Kyun Park, Po-Wei Chen, Nicole M. Anthony, Esteban Gomez, Sean Haq, Samuel E. Wurzel, Rajiv Bhat, Samik Dasgupta, Manuel Castellanos Beltran, Kassandra Neff Castellanos, Javier von Stecher, Leila Gomez, Ashley R. Carter, Gregory Herman, Amanda E. Carpenter, Martin M. Boyd, Justin A. Kuczynski, Yeonee Seol, Gavin M. King, Karen L. King, Byungmoon Cho, Laura C. Sinclair, Galen C. O'Neil, Shihkuang Tung, Ching-yu Claire Wu, Juan M. Pino, Russell Stutz, Giacomo Lamporesi, Aaron E. Leanhardt, D. Hern Paik, Julie L. Fiore, Haemi Li, Stephanie A. Meyer, Qudsia Quraishi, Emily Gibson, Carl J. Sauer, Kristine Abeyta, Ignacio Castellanos Beltran, Huanqian Loh, Kunio Toshimitsu, Yoko Fukuda, Norie Fujita, Janet E. McCombs, Meghana Rangan, Lora Nugent-Glandorf, Allison B. Churnside, Vasiliy Fomenko, James Fung-A-Fat, Terry J. Brown, Maritza Sales, Laura K. Mortimer, Matthew D. Seaberg, Michael S. Foss-Feig, Jesse C. Marcum, Rebecca K. Montange, Genevieve Park, and Juthika Khargharia. I would like to especially thank Julie, Amanda, Meghana, Janet, Zhao, Juthika, and Matt for their friendship and support. You have been a great source of genuine encouragement, invaluable support, hearty laughter, and true inspiration.

Finally, I cannot thank my family enough, including Hannah Hosotani, Akiko Hosotani, Yutaka Hosotani, Suzuko Hosotani, Seigo Hosotani, Masako Hosotani, Yoko Arima, and Ronald Uno for their support. I would like to give special thanks to my compassionate and unfailing sister who has rallied and been there for me throughout, my caring and inquisitive mother for her deep love of learning, and my thoughtful and warmhearted father who has inspired me and my interest in science.

Contents

Chapter

Tables

Table

Figures

Figure

Chapter 1

Introduction

Life is governed by enzymes, remarkable molecular devices that are central to every biochemical process. Enzymes are absolutely essential to human existence, whether they are functioning in human cells, in the microbiota of microorganisms living in our bodies, or in the ecosystems in which we live. These highly-specialized molecules coordinate the patterns of development, regulation, and repair within cells by accelerating a vast diversity of chemical reactions by 6–17 orders of magnitude [1, 2]. When enzyme function is altered, the effects can be disastrous. Malfunction or deficiencies of a single critical enzyme can lead to disease [3].

Enzyme dynamics have been shown to be a significant factor in enzyme function [4]. To study the conformational changes of enzymes, either in isolation or complexed with their substrates, computational and experimental studies are needed. Techniques such as X-ray crystallography, NMR studies, and biochemical and mutational analysis have provided critical insights into the characterization of the dynamics of enzymes. The emergence of single-molecule techniques is complementary to the aforementioned techniques in the pursuit to probe and understand the dynamics of various enzymatic systems.

The advent of single-molecule manipulation [5, 6, 7, 8, 9] and single-molecule detection [10, 11, 12] methods have made highly-sensitive, real-time measurements of individual biomolecules and cellular processes possible. In comparison to conventional ensemble methods, single-molecule experiments offer several advantages [13, 14, 15, 16]. Molecular properties of inhomogeneous systems can be measured, revealing information that is often hidden by ensemble-averaged results.

Single-molecule studies permit real-time observation of rarely-populated transients that are difficult or impossible to measure with conventional methods, such as the study of the movement, force generation, response to external force, and unfolding of biomolecules. In conjunction with ensemble techniques, single-molecule techniques have been instrumental in unveiling the underlying molecular mechanisms of various biomolecular systems.

For example, single-molecule methods have permitted observation of the dynamics of numerous enzymes and provided insight into their mechanisms, as highlighted in the following cases. In one case, the first measurements of the individual steps of a virus packaging motor in the bacteriophage $\Phi 29$ were observed with high-resolution optical tweezers [17]. Packaging of double-stranded DNA (dsDNA) by this ring ATPase was found to occur in 10 base-pair (bp) increments composed of four 2.5-bp steps via a mechanism requiring contacts primarily with the phosphate backbone [17, 18]. In a second case, Cornish *et al.* used single-molecule fluorescence resonance energy transfer (FRET) to observe the first real-time intersubunit rotations of the ribosome [19], a universal RNA-based molecular machine that performs protein synthesis. The 30S and 50S subunits, which comprise the ribosome, were found to spontaneously rotate between two conformational states shown to be the intermediate steps involved in translation. These two studies exemplify the scope of single-molecule techniques to investigate enzyme dynamics unseen by ensemble methods.

1.1 Destabilization Dynamics of a Helicase

One area being explored by single-molecule work is the study of helicases and translocases [20]. DNA helicases are protein enzymes that translocate directionally through dsDNA substrates to catalyze the separation of the complementary DNA strands. A DNA helicase harnesses the energy from nucleoside $5'$ triphosphate (NTP) binding and hydrolysis to destabilize the hydrogen bonds between complementary base pairs within a dsDNA molecule while undergoing translocation along the dsDNA. The mechanism of this mechanochemical coupling is still not fully understood [21, 22].

The mechanism of one particular DNA helicase, the RecBCD enzyme, has several unresolved questions [23]. One of the outstanding questions is its translocation step size. The step size of

RecBCD has been debated due to seemingly conflicting studies. Rapid reaction techniques to monitor the unwinding kinetics of a series of DNA duplexes of different lengths [24] with global fitting of the unwinding time courses yield the RecBCD "kinetic step size," the average distance unwound between two successive rate-limiting steps in the unwinding cycle [25], as 3.9 ± 0.5 bp, independent of temperature and ATP concentration [26]. However, crystallographic studies of similar helicases bound to DNA in ATP-analog-bound and ATP-analog-free states suggest a 1-bp step size [27, 28, 29].

To investigate this discrepancy, we aimed to measure the physical step size of RecBCD directly using a high-precision optical-trapping assay. In addition to the ability to measure the dynamics of individual molecules, optical-trapping assays can explore the force dependence of unwinding and allow measurements of the energy landscape. Previous measurements of RecBCD with an optical trap were limited to 6-bp resolution [30]. To improve resolution, active stabilization of the sample and laser intensity was incorporated to achieve sensitivity to 1-bp movements [31]. With this improved single-molecule assay, RecBCD translocation along DNA was measured. In doing so, we observed large, multi-base-pair conformational dynamics of the RecBCD·DNA complex. The nature of these dynamics is discussed here.

We interpret the large RecBCD·DNA conformational dynamics as conformational changes of the enzyme and rapid back-and-forth translocation of the enzyme pin along the DNA, modulated by the enzyme's nucleotide state. Five key observations support this interpretation. First, the large conformational dynamics were present in the absence of ATP. Second, the onset of these dynamics was coincident with previously-determined kinetic studies of the onset of unwinding activity, which demonstrate requirement of a sufficiently-long $5'$ DNA strand ($\geq$ 10 nucleotides) to engage the RecD helicase [32]. Third, the conformational dynamics were reduced in the presence of three particular nonhydrolyzable ATP analogs, ADP·BeF_x, AMPPNP, and ADP + P_i. Fourth, the conformational dynamics were modulated by the GC-content of the DNA. Finally, these dynamics were suppressed in the presence of an engineered, interstrand cross link in the DNA. Taken together, these results suggest a mechanism in which large conformational dynamics of the RecBCD·DNA complex, including dynamic destabilization of the DNA duplex by the helicase, are modulated by

the nucleotide-bound state of the enzyme.

1.2 Real-Time Ribozyme Cleavage

Ribozymes are RNA molecules that have intrinsic enzyme-like activity. Their discovery [33, 34] drastically expanded the view of RNA molecules from simply a messenger that passed genetic information from DNA to proteins, to catalytic molecules able to function in the complete absence of protein cofactors [33, 34]. It has since been shown that RNA performs major catalytic functions in the ribosome [35, 36, 37] and spliceosome [38, 39], two essential ribonucleoprotein complexes in cells. In addition, RNA can play a remarkable role in regulating gene expression [40]. Hundreds of small noncoding RNAs, microRNAs, and endogenous small-interfering RNAs have been discovered that perform transcriptional and posttranscriptional regulation [41, 42, 43, 44]. As a result, RNA applications have been developed in biotechnology and medicine [45, 46, 47], including development of RNA-based biosensors [48, 49, 50].

RNA-based biosensors have been proposed to offer a robust alternative to protein-based binding molecules, e.g., antibodies. In comparison to monoclonal antibodies, nucleic-acid-based biosensors carry distinct advantages, such as the ability to sense toxic target molecules, high stability, and ease of synthesis and modification [49, 51, 52, 53]. Single-stranded DNA and RNA molecules have been shown to be able to bind target molecules with high affinity and high specificity, rivaling the binding properties of antibodies [51, 52].

One particular naturally-occurring, RNA-based biosensor that has catalytic and gene regulatory functions is the *glmS* ribozyme [54]. This ribozyme functions by responding to binding of its target ligand by undergoing self-cleavage, which then destabilizes the mRNA in cells to reduce gene expression [54, 55]. The investigation of the *glmS* ribozyme provides insight into a mechanism for gene regulation by a ribozyme, as well as potentially aiding the development of synthetic, RNA-based biosensors. Here, we developed a single-molecule cleavage assay of the *glmS* ribozyme to measure cleavage of single ribozymes, providing demonstration of an assay that may be applied to other nucleic-acid-based biosensors.

1.3 Overview of Thesis

In Chapter 2, we describe the experimental techniques in detail. First, we discuss the characteristics of DNA and RNA, the nucleic acids that are central elements in this thesis, nucleic-acid processing, catalytic activity, and precise manipulations. Next, we explain the underlying physical principles of optical trapping, the instrument design involved in 1-bp stabilization, and the key procedures for optimization of and measurements using the trap. Details of sample preparation, data acquisition, and data analysis are described.

In Chapter 3, we explore the motion of individual RecBCD helicases with a 1.5-bp resolution optical-trapping assay. First, we discuss background information on helicase, including structural features common to helicases, proposed models of unwinding and directed translocation, as well as the importance of the role of RecBCD in DNA replication and maintenance in *Escherichia coli*. Next, we present measurements of the conformational dynamics of RecBCD·DNA complexes. We measure large, multi-base-pair-sized conformational dynamics that are consistent with RecBCD back-and-forth translocation along DNA. These conformational dynamics are suppressed when an interstrand cross link is incorporated into the DNA substrate. Furthermore, the amplitude of the conformational dynamics is shown to depend on the GC content of the dsDNA near the ssDNA-dsDNA junction. The amplitude and frequency of the translocation are shown to be modulated by the nucleotide state of the enzyme, as well as by the force applied by the optical trap.

In Chapter 4, we present single-molecule measurements of *glmS* ribozyme cleavage. First, we discuss background information on RNA as a catalytic molecule and gene-regulatory element, as well as background information on the *glmS* ribozyme, including its function in the cell and three-dimensional structure. Next, we detail the experimental techniques of the single-molecule RNA-based biosensor. Synthesis of the detection element is discussed. Cleavage signals were measured using video microscopy and utilization of tethering a nanoparticle to a surface via a ribozyme-containing RNA:DNA construct. Finally, we interpret the cleavage data of single *glmS* ribozymes and conclude with future directions for this type of study.

In Chapter 5, we discuss several future prospects for study of the RecBCD enzyme.

The major results of this work are threefold: 1) Direct measurement of destabilization dynamics of the RecBCD·DNA complex that are qualified by new measurements of RecBCD bound to a cross-linked DNA substrate; 2) Modulation of the destabilization dynamics in the presence of an ATP analog signifying altered conformational dynamics of the complex dependent on the nucleotide-bound state of the enzyme; and 3) Development of a new single-molecule biosensor assay utilizing the *glmS* ribozyme. Although destabilization of DNA substrates has been inferred in studies of other helicases, the work presented here is, to our knowledge, the first real-time measurement of multiple-base-pair destabilization dynamics of a helicase·DNA complex. This measurement was possible due to the high precision of our RecBCD optical-trapping assay, which was capable of measuring conformational changes at the level of 0.50 ± 0.05 nm (1.5 ± 0.2 bp, mean ± $\sigma_{\bar{x}}$, at Δf = 0.01–1 Hz on 993-nm DNA under a 6-pN load). The measurements reported here quantify conformational dynamics that are greater than 4 bp on a 100-ms time scale and indicate translocation of the helicase pin relative to the DNA substrate, contrasting crystallographic studies that suggest discrete 1-bp translocation of superfamily-1 and superfamily-2 helicases along their DNA substrates.

Additionally, this thesis presents a new biosensor sensitive to catalytic events of individual ribozymes. The exploration of biosensors that use nucleic acids as the detection element is proving to be a viable alternative to traditional biosensors, which utilize antibodies as the sensing domain. The assay presented here enables self-cleavage to be measured in real time by visualizing each ribozyme attached to a surface with a nanoparticle. This assay is versatile enough to be applicable to a variety of nucleic-acid-based biosensors in addition to the *glmS* ribozyme, making it an important addition to the single-molecule toolbox available for studying catalytic nucleic acids.

Chapter 2

Experimental Technique: Precision Optical-Trapping Assay

This chapter discusses the techniques of optical-trapping instrumentation to conduct single-molecule studies of a helicase. To calibrate our optical-trapping apparatus, it is important to understand the physical properties of DNA under study (Section 2.1.1) and the underlying physical principles of optical trapping (Section 2.2). Section 2.3 discusses precision optical-trapping instrumentation, Section 2.4 describes alignment and calibrations, and Section 2.5 discusses sample preparation. Section 2.6 discusses the acquisition of RecBCD data and controls and Section 2.7 discusses methods of analysis.

2.1 Nucleic-Acid Characteristics

2.1.1 DNA

The maintenance and repair of deoxyribonucleic acid (DNA) is essential for eukarya, archaea, and bacteria. DNA stores genetic information important for the development and functioning of all known living organisms. Damage to DNA can be caused both endogenously and exogenously, causing DNA lesions. Unrepaired lesions can lead to mutagenesis and carcinogenesis [56, 57] and contribute to neoplastic transformation of cells, i.e., malignant tumors [58, 59, 60].

Studies of the elastic properties of DNA [61, 62, 63] serve as a basis for studies of DNA remodeling by helicases, nucleases, nucleosome packaging enzymes, and other remodeling and repair enzymes. B-form DNA, composed of two complementary single strands of DNA, is the most common form of DNA found in biology. It assumes a right-handed double-helical structure of 10 base pairs

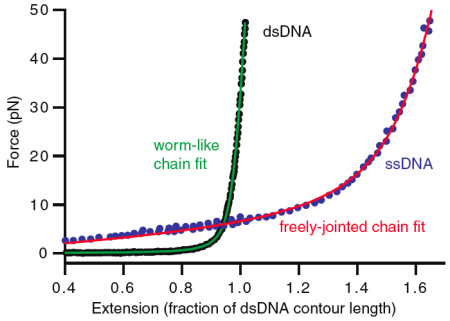

Figure 2.1: Force extension curves (FECs) of dsDNA and ssDNA. Reproduced from Woodside and Valentine (2009) [68] with kind permission of Springer Science and Business Media. The dsDNA FEC (*black*) is well fit by a worm-like chain model, Equation 2.1 (*green*), whereas the ssDNA FEC (*blue*) is fit by a freely jointed chain model (*red*). [Adapted from Wang *et al.* (1997) for dsDNA and Smith *et al.* (1996) (ssDNA).]

(bp) per turn [64], a pitch of 3.4 nm, and radius of 1.0 nm [65]. The bending stiffness of DNA is quantified by the persistence length [66], which depends on the molecule's local elastic behavior. The persistence length for B-form double-stranded (ds) DNA is ~50 nm, whereas that of single-stranded (ss) DNA ranges between 0.8–1.4 nm at 0.1 M salt concentrations [67].

A single dsDNA molecule subjected to force shows a characteristic relationship between force and extension, described by the force-extension curve [68] (Figure 2.1). This behavior is best fit by the worm-like chain model, which treats the dsDNA as an elastic rod [63, 69]. A useful interpolation formula for worm-like chains has been developed for fitting a force-extension curve [70]:

$$F = \frac{k_\mathrm{B}T}{L_\mathrm{p}}\left[\frac{1}{4}\left(1 - \frac{x}{L} + \frac{F}{K}\right)^{-2} - \frac{1}{4} + \frac{x}{L} - \frac{F}{K}\right], \tag{2.1}$$

where L_p is the persistence length, L is the contour length, and K is the elastic modulus of the dsDNA. At low forces, entropic elasticity of the polymer chain dominates, whereas at high forces, enthalpic elasticity of the bonds in the backbone dominates.

A nucleic acid is a biopolymer composed of nucleotides. A nucleotide is composed of a pentose sugar ring, a phosphate group, and either a purine or pyrimidine base that is linked to the $1'$ carbon on the pentose sugar (Figure 2.2). The alternating sugar and phosphate groups make up the backbone of the nucleic acid. The phosphate group links the $3'$ carbon and $5'$ carbon of adjacent

sugar molecules, giving single-stranded (ss) nucleic acids a polarity. The bases found in DNA and RNA are different: adenine (A), cytosine (C), and guanine (G) are found in both DNA and RNA; thymine (T) occurs only in DNA; and uracil (U) only occurs in RNA. Base pairing occurs through hydrogen bonding between bases. In dsDNA, adenine and thymine form an "AT" bp, which has two hydrogen bonds, and guanine and cytosine form a "GC" bp, which has three hydrogen bonds. The free energy to open a single base pair was determined from DNA unzipping experiments fit to a theoretical model [71], yielding best-fit values of 1.2 $k_{\mathrm{B}}T$ for an AT bp and 3.4 $k_{\mathrm{B}}T$ for a GC bp at 25 °C in 7 mM $MgCl_2$ and 50 mM NaCl [72].

Proteins that bind DNA and recognize specific DNA sequences do so by interacting with potential hydrogen-bond donor and acceptor atoms in the two grooves within the double helix, designated as the major and minor grooves [1] (Figure 2.3). The minor groove contains the pyrimidine O-2 and the purine N-3 of the base pair, and the major groove is on the opposite side of the pair. These grooves arise because the glycosidic bonds of a base pair are not diametrically opposite each other [1] (Figure 2.4). The larger size of the major groove in B-DNA makes it more accessible for interactions with proteins that recognize specific DNA sequences [1].

2.1.2 RNA

RNA is found in a variety of forms including messenger RNA (mRNA), transfer RNA (tRNA), RNA bound to proteins to form ribonucleoproteins, and even RNA molecules that adopt complex three-dimensional structures to perform chemical reactions or regulate gene expression. The best known type of RNA, mRNA, is single stranded and contains sequence information for protein biosynthesis, i.e., translation. Some RNA is double stranded (e.g., some viral RNA, micro RNA, and small interfering RNA) and contributes to the immune response to viruses, as well as the regulation of gene expression. Transfer RNA molecules contain an anticodon region that base pairs to the corresponding codon on mRNA during translation. Ribonucleoproteins are nucleoproteins that contain RNA. RNA molecules that assume tertiary structures, such as ribozymes and riboswitches, are discussed in Section 4.1.

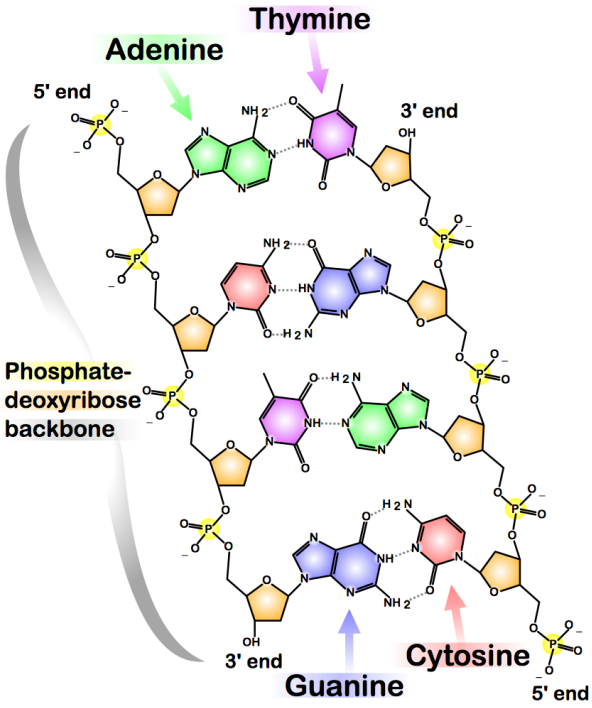

Figure 2.2: Chemical structure of DNA.

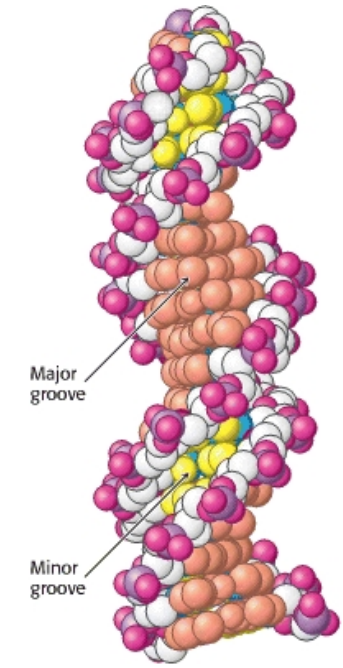

Figure 2.3: Major and minor grooves in B-form DNA. Figure from Berg *et al.* (2002) [1]. The major groove (*orange*) and the minor groove (*yellow*) are depicted. The carbon atoms of the backbone are shown (*white*).

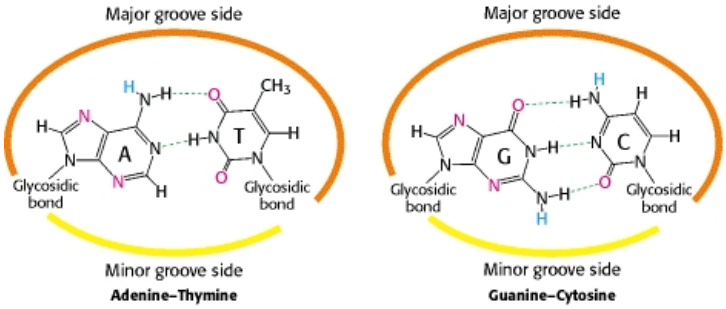

Figure 2.4: Major and minor grooves in B-form DNA. Figure from Berg *et al.* (2002) [1]. Because the two glycosidic bonds are not diametrically opposite each other, each base pair has a larger side that defines the major groove and a smaller side that defines the minor groove. The grooves are lined by potential hydrogen-bond donors (*blue*) and acceptors (*red*).

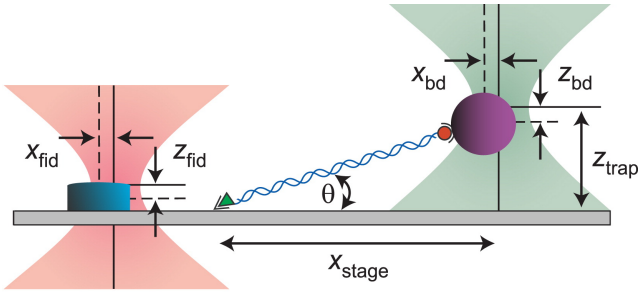

Figure 2.5: Surface-coupled optical-trapping assay. Reprinted from Carter *et al.* (2009) [31] with permission from Elsevier. A DNA molecule is held between two points, a cover slip and a trapped bead (*purple*). One laser (*red*) monitors the position of a fiducial mark in three dimensions (e.g., x_{fid}) to actively suppress mechanical perturbations. A second laser (*green*), collinear to the trap, measures bead position (x_{bd}). The x_{stage} is the distance between the DNA's anchor point to the cover slip and the center of the optical trap.

The molecular composition of RNA is very similar to that of DNA. As mentioned in 2.1.1, the base, uracil (U), only occurs in RNA. RNA nucleotides contain a ribose while DNA nucleotides contain a deoxyribose. The additional 2′-hydroxyl group increases the susceptibility to spontaneous hydrolysis of the phosphodiester bonds in RNA. Some ribozyme catalytic activity involves nucleophilic attack of a 2′-hydroxyl on the adjacent 3′-phosphate group [73, 74], such as that of small RNA ribozymes of ~40–160 nucleotides that catalyze site-specific self-cleavage.

2.2 Principles of Optical Trapping

Optical trapping of dielectric particles, also referred to as optical tweezers, is one of the most sensitive tools for manipulating single molecules and measuring their properties [68, 75]. An optical trap consists of a strongly focused light beam that can apply forces in the piconewton range to micron-sized, neutral particles [76, 77]. In a typical surface-coupled optical-trapping assay, a DNA molecule is attached to a surface at one end while attached to an optically-trapped bead at the other [78] (Figure 2.5).

A dielectric particle near the focus of a laser will experience a force due to the transfer of momentum from the radiation pressure of incident photons. Traditionally, this optical force is decomposed into two components: a scattering force and a gradient force [70]. The scattering

component of the force, in the direction of light propagation, arises from momentum transfer from the incident photons to the particle. The gradient component of the force, in the direction of the spatial light gradient, arises from the fact that a dipole in an inhomogeneous electric field experiences a force in the direction of the field gradient [79]. It follows that due to balance between the scattering force and the gradient force, the trapped particle axial equilibrium position is located slightly down-beam from the trap focus. The gradient trapping force arises from fluctuating dipoles in the dielectric particle induced by the laser, which interact with the inhomogeneous electric field at the focus [70].

In developing a theoretical treatment of optical trapping, it is useful to examine the two limiting cases for which the force on a sphere can be calculated, the Mie and Raleigh regimes. The conditions for Mie scattering are satisfied when the trapped sphere radius (r_0) is much larger than the trapping laser wavelength (λ), i.e., $r_0 >> \lambda$. The forces in this regime can be calculated from ray optics [80]. For a single ray of power P hitting a dielectric sphere at an angle of incidence θ_1 with incident momentum per second $n_{\mathrm{m}}P/c$, the forces acting through the origin are

$$F_{\mathrm{scatt}} = \frac{n_{\mathrm{m}}P}{c}\left\{1 + R\cos 2\theta_1 - \frac{T^2[\cos(2\theta_1 - 2\theta_2) + R\cos 2\theta_1]}{1 + R^2 + 2R\cos 2\theta_2}\right\} \tag{2.2}$$

and

$$F_{\mathrm{grad}} = \frac{n_{\mathrm{m}}P}{c}\left\{R\sin 2\theta_1 - \frac{T^2[\sin(2\theta_1 - 2\theta_2) + R\sin 2\theta_1]}{1 + R^2 + 2R\cos 2\theta_2}\right\}, \tag{2.3}$$

where n_{m} is the index of refraction of the medium, θ_1 and θ_2 are the angles of incidence and refraction, the quantities R and T are the Fresnel reflection and transmission coefficients of the surface at θ_1, n_{m} is the index of refraction of the medium, and c is the speed of light in vacuum.

The conditions for Raleigh scattering are met when the trapped sphere is much smaller than the wavelength of the trapping laser, i.e., $r_0 << \lambda$. In this approximation, the optical forces can be calculated by treating the particle as a point dipole. For a sphere of radius r_0, the scattering force is [70]

$$F_{\mathrm{scatt}} = \frac{I_0\sigma n_{\mathrm{m}}}{c}, \tag{2.4}$$

$$\sigma = \frac{128\pi^5 r_0^6}{3\lambda^4}\left(\frac{m^2-1}{m^2+2}\right)^2, \tag{2.5}$$

where I_0 is the intensity of the incident light, σ is the scattering cross section of the sphere, m is the ratio of the index of refraction of the particle to the index of the medium ($n_\mathrm{p}/n_\mathrm{m}$), and λ is the wavelength of the trapping laser. The scattering force is proportional to the intensity. The time-averaged gradient force is given by

$$F_\mathrm{grad} = \frac{2\pi\alpha}{cn_\mathrm{m}^2}\nabla I_0, \tag{2.6}$$

$$\alpha = n_\mathrm{m}^2 r_0^3\left(\frac{m^2-1}{m^2+2}\right), \tag{2.7}$$

where I_0 is the intensity of the incident light and α is the polarizability of the sphere. The gradient force is proportional to the intensity gradient and points up the gradient when $m > 1$.

For small displacements, the gradient restoring force is proportional to the offset from the equilibrium position, describing a Hookean spring with a characteristic stiffness that is proportional to the light intensity.

2.3 Instrument Design

To enable measurement of bp-scale displacements, we needed an optical-trapping assay with 1-bp stability. A typical optical-trapping instrument cannot achieve 1-bp resolution [31]. However, many biophysical systems exhibit dynamics that are on the scale of a single base pair, including enzymes that translocate along DNA. For instance, the 1-bp step of RNA polymerase was measured [81] using a dual-beam optical-trapping assay to reduce surface-induced noise [81, 82]. To determine whether RecBCD takes 1-bp steps along DNA, a surface-coupled optical-trapping assay with atomic-scale (~0.1 nm) stability was developed [31]. An inverted microscope (Nikon, TE-2000) was modified to allow trapping at the specimen plane, dynamic control of the lasers and sample, improved stability, and high-resolution detection [31, 83].

2.3.1 Trapping

Our essential components for optical trapping included a high-powered neodymium-doped yttrium orthovanadate crystal laser (Spectra-Physics, Millennia IR, 10 W, $\lambda = 1064$ nm), beam expansion optics (New Focus, $f = 8$ mm Aspheric Lens, and Thorlabs, Plano-Convex Lens, $f = 100$ mm), two stabilized diode lasers (Blue Sky Research, VPSL, 50 mW, $\lambda = 785$ and 850 nm), two-axis PZT mirrors to steer the lasers (Physik Instrumente, S330.2SL), a high numerical aperture objective (Nikon, PlanAPO-100X-IR, numerical aperture = 1.4), a sample holder, and quadrant photodiodes for detection (PerkinElmer Optoelectronics, YAG-444-4A with custom electronics). The trap stiffness was controlled by an acousto-optic modulator (AOM; Isomet, 1205C), which consists of a crystal with an optical diffraction grating that is generated by an acoustic wave. The amplitude of the acoustic wave was modulated to control the intensity of the deflected first-order diffracted light, thus controlling the trap intensity over a broad range. Similarly, the intensity of each detection laser was controlled by separate AOMs (generally set to constant values). The AOMs additionally served as part of feedback loops used for intensity stabilization (see Section 2.3.4).

2.3.2 Position detection

Precise, high-bandwidth position detection of the trapped polystyrene bead was achieved through back-focal-plane (BFP) detection [84, 85, 86]. BFP detection provides the three-dimensional position of the trapped object with nanometer-scale resolution and a bandwidth up to several MHz, only limited by the photodiode performance and amplifying electronics [84, 85]. Laser light passing through the specimen was collected on a quadrant photodiode (QPD) placed on the optical axis in a position that is optically conjugate to the BFP of the microscope condenser [78]. The diode quadrants are summed pairwise, normalized, and the lateral, differential signals were derived from the pairs for both x and y dimensions. Normalization served to reduce the effect of intensity amplitude changes on the QPD. The axial motion (z) was deduced from the total QPD signal, hereon referred to as the sum signal (i.e., the total light impinging upon the four quadrants of

the QPD). The sum signal was offset amplified with a differential amplifier with a voltage offset. Specifically, a reference voltage V_0 was subtracted from the original sum signal V_{sum} and multiplied by a gain g of 1000, i.e., $g(V_{\text{sum}} - V_0)$. The QPDs featured 250 kHz bandwidth. Detection laser power at the QPD was ~40 μW.

2.3.3 Position control

Lateral motion of the lasers was controlled by scanning mirrors. The lateral positions of the optical trap and fiducial mark detection laser in the specimen plane were controlled by two feedback-stabilized, lead-zirconate-titanate (PZT) piezoelectric scanning mirrors placed in planes optically conjugate to the back focal plane of the objective lens. Pure rotations in this plane lead to pure translations in the image plane. This allowed dynamic computer control over the positions of the optical trap and detection laser.

Incorporation of a piezoelectric stage allowed dynamic positioning of the sample chamber relative to the trap and facilitated calibration. A three-axis, closed-loop PZT stage (Physik Instrumente, P517.3CD) with stage controller (Physik Instrumente, E-710.P3D) was used to position the sample chamber, calibrate the instrument, and stabilize the microscope [78].

2.3.4 Stabilization technique

To stabilize the optical-trapping assay to 0.1 nm in three dimensions, several stabilization techniques were used [31]. An inverted optical microscope was stabilized to 0.1 nm in three dimensions [78]. Two detection lasers were used to establish a local, differential measurement reference frame to actively stabilize the surface [78] (Figure 2.6). One detection laser monitored the trapped bead position, while the other measured fiducial position, which was fed to the stage controller that moved the stage. Local detection suppresses thermal expansion and differential measurement suppresses noise common to both lasers, such as air currents and objective lens drift [83]. Finally, trap and detection laser noise were reduced.

Decreasing multiple types of trap laser noise was critical to achieving atomic-scale resolution

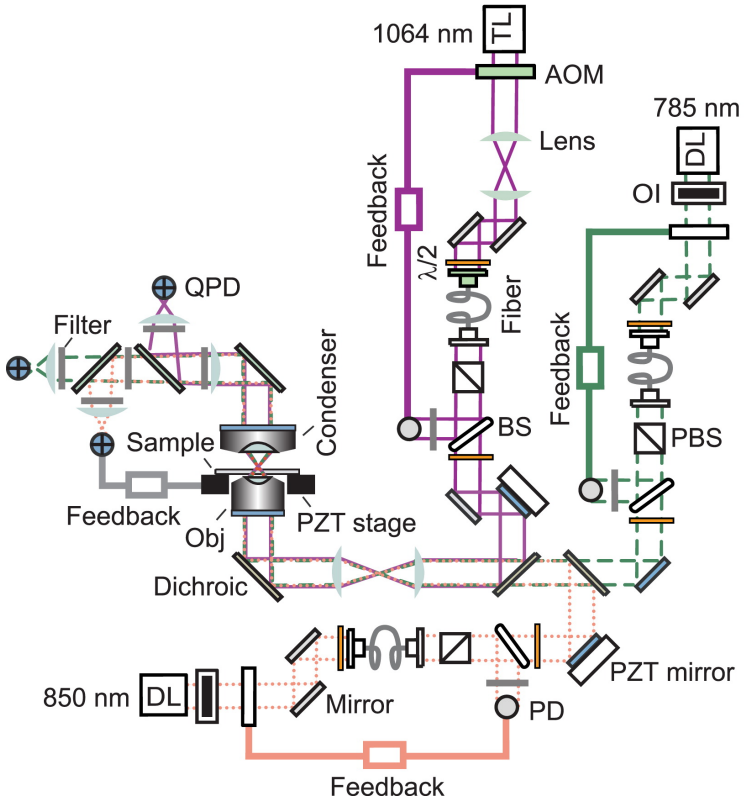

Figure 2.6: Optical layout for stabilized optical trapping. Reprinted from Carter *et al.* (2009) [31] with permission from Elsevier. Two detection lasers (DL, λ = 785 nm and 850 nm) were stabilized using an acousto-optic modulator (AOM) based feedback loop [78]. The trap laser (TL, *purple*) was stabilized using a modified version of this method that imaged the AOM onto the fiber-coupling lens (optically conjugate planes shown in *light green*). All three lasers were combined with dichroics to couple them into the objective (Obj). Mirrors in conjugate planes (*light blue*) to the back-focal plane of the objective enabled independent beam steering of the three beams. We measured bead and sample position in three dimensions using back-focal-plane detection. Acronyms represent the following: OI, optical isolator; PBS, polarizing beamsplitter; PD, photodiode; BS, beam sampler; PZT, piezo-electric; QPD, quadrant photodiode; and $\lambda/2$, half-wave plate.

[31]. Pointing, intensity, mode, and polarization noise were reduced by similar intensity stabilization methods used for the detection lasers [78]. Pointing, mode, and polarization noise of the trapping laser was translated into intensity noise through the combination of a single-mode, polarization-maintaining fiber and polarizing beam splitter. The resulting intensity was sampled and actively stabilized with a feedback loop to AOM that stabilized the intensity. The steady-state trap intensity noise was decreased to 0.01% root mean-square at moderate laser powers [31]. With this instrument, 1-bp positional precision over the frequency range 0.03-2 Hz and sensitivity to 1-bp steps along DNA at moderate force were achieved [31].

2.4 Alignment, Calibration, and Characterization

Alignment and calibration of the precision optical-trapping instrument requires a series of steps that may need several iterations (summarized in Appendix B). Also, corresponding LabVIEW programs to run the instrument, IGOR analysis procedures, and example data records are noted (Appendix B).

2.4.1 Coarse alignment

For optimal alignment, laser beams must be level, not clipping on any optics, and parallel to the screw holes in the optical table. Lenses and detectors should be aligned to the optical axis of the laser beam. Optics should be positioned to minimize the beam path and placed in accordance to standard optical imaging principles. For example, telescoping lenses are positioned for imaging the PZT mirrors to the objective back focal plane. Beams should hit the center of the PZT mirrors. Fiber coupling of the laser into the fiber should be adjusted such that the output from the AOM is imaged onto the angle-cleaved fiber tip. For this system, the collimated trap laser is ~1 inch in diameter, so care must be taken so that clipping of the beam is minimized, especially because most optics are 1 inch in diameter. A charge-coupled device (CCD) camera is used to image the specimen plane and should be positioned to be optically conjugate to the trapping plane.

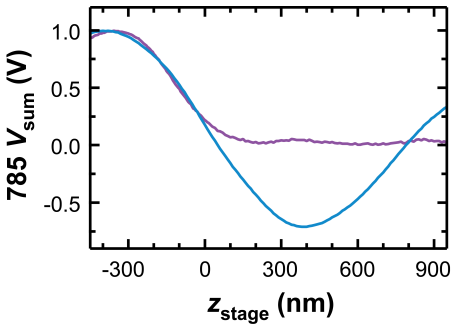

Figure 2.7: Axial QPD signals of a free (*purple*) and stuck (*blue*) bead as the stage was moved in the axial direction.

2.4.2 Trap-laser collimation

If the trap laser is not optimally collimated prior to entering the objective, then the trapping efficiency will be dependent on the bead height above the sample surface. To adjust the collimation of the trapping laser (λ = 1064 nm) such that it keeps a trapped, free (non-tethered) bead at a constant axial position when lowering the stage position, translate the second lens after the trap fiber output in the axial direction, and translate the output end of the trap fiber in the axial direction. Measure the 1064 sum signal (V_{sum}) of a trapped free bead versus stage position (z_{stage}), scanning from when the bead leaves the surface to when z_{stage} is several microns away (Figure 2.8). The position detector sum signal measured by the QPD is proportional to the total incident intensity at the back focal plane of the condenser, providing a means of locating the surface of the trapping chamber and measuring the focal shift. As the bead moves through the focus of the trap laser, the phase of light scattered from the bead changes by 180° relative to the unscattered light due to the Gouy phase shift. A stuck bead signal undergoes the full shift, whereas a trapped free bead maintains a relatively constant axial position [70] (Figure 2.7).

2.4.3 Detection-laser focal-position optimization

Steps in Section 2.4.2 were repeated using the signals for the bead detection laser (λ = 785 nm) (Figure 2.8). A coarse adjustment was performed by making the image of the bead detection

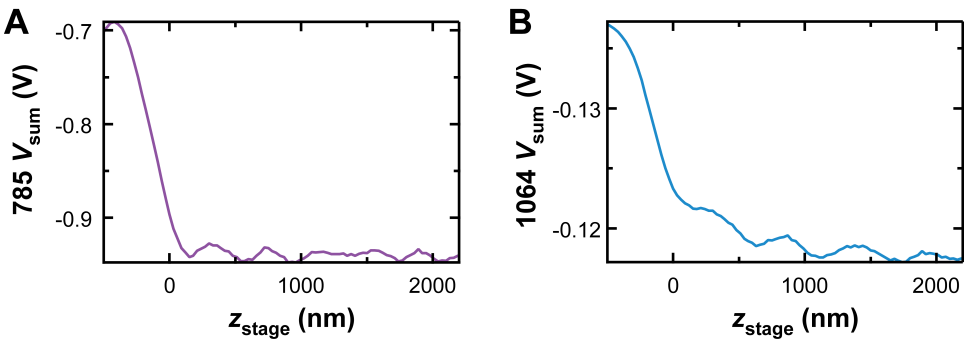

Figure 2.8: Axial QPD signals of a free bead. (A) The sum voltage signal measured by the 785 nm detection laser QPD as a function of stage position. (B) The sum voltage signal measured by the 1064 nm trap laser QPD as a function of stage position.

laser focus on the CCD camera in the same image plane as that of the trapped bead. We measured the 785 sum signal ($V_{785,\mathrm{sum}}$) of a trapped, free bead versus stage position (z_{stage}), scanning from when the bead left the surface to when z_{stage} was several μm away. Then, we translated the second lens after the fiber output in the axial direction, and translated the output end of the fiber in the axial direction to "flatten" the bead position signal such that it stayed constant as z_{stage} increased.

The CCD camera was positioned in a plane conjugate to the trapping plane. We determined the z position at which a trapped bead leaves the cover slip surface by overlaying a 785-nm z scan of a free bead with that of a stuck bead (e.g., surface-to-peak ~340 nm). We set the CCD camera position to be at the image plane of when a stuck bead was at that position (Figure 2.7).

We positioned the fiducial mark detection laser (λ = 850 nm) focus at ~300 nm below the trapping plane (i.e., below the trap focal position) for optimal sensitivity to measure sample position relative to the trap, used for active sample stabilization. The trap position can be determined using the aligned 785 QPD sum signal off a stuck bead. We measured the sum signal off the bead with the stage detection laser (λ = 850 nm). The 850 nm second lens and fiber tip were axially moved to optimize the 850 nm position of the focus (e.g., to be in line with the 785 laser focus, or, in the case of the RecBCD assay, to be 300 nm below the 785-nm laser focus).

2.4.4 Position calibration

Position calibrations were performed to determine the bead or fiducial mark position from the response of the QPD detector signals of the detection lasers. To calibrate position of a fiducial mark, the fiducial mark is moved across the detector region by the stage in x (Figure 2.9), y (Figure 2.9), and z (Figure 2.10). To calibrate the position of a trapped bead, the bead is moved across the detector region by steering the trap. During fiducial or bead movement, the detector output signal is recorded and then plotted as a function of position. The position calibration is performed each time a bead or fiducial mark measurement is made.

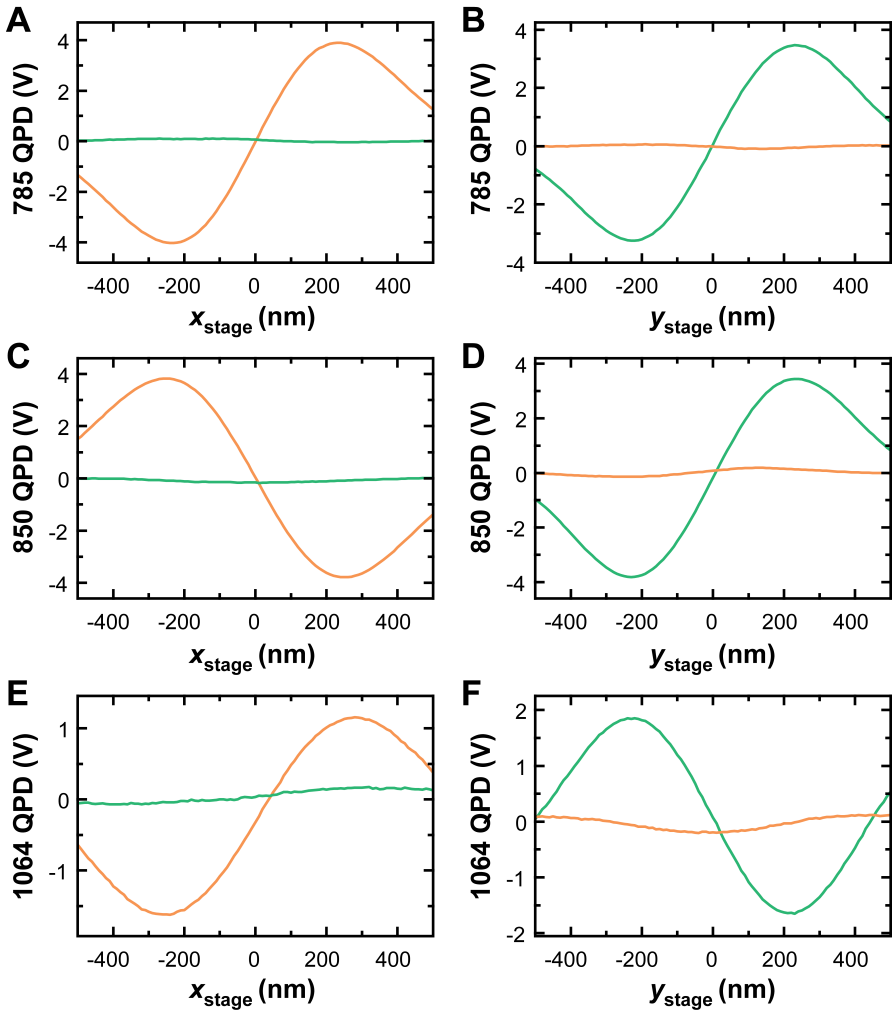

Figure 2.9: QPD signals of a stuck bead translated laterally. QPD x signals are shown in *orange*, and QPD y signals are shown in *green*. (A) 785 nm laser QPD lateral signals of a bead translated in x. (B) 785 nm laser QPD lateral signals of a bead translated in y. (C) 850 nm laser QPD lateral signals of a bead translated in x. (D) 850 nm laser QPD lateral signals of a bead translated in y. (E) 1064 nm laser QPD lateral signals of a bead translated in x. (F) 1064 nm laser QPD lateral signals of a bead translated in y.

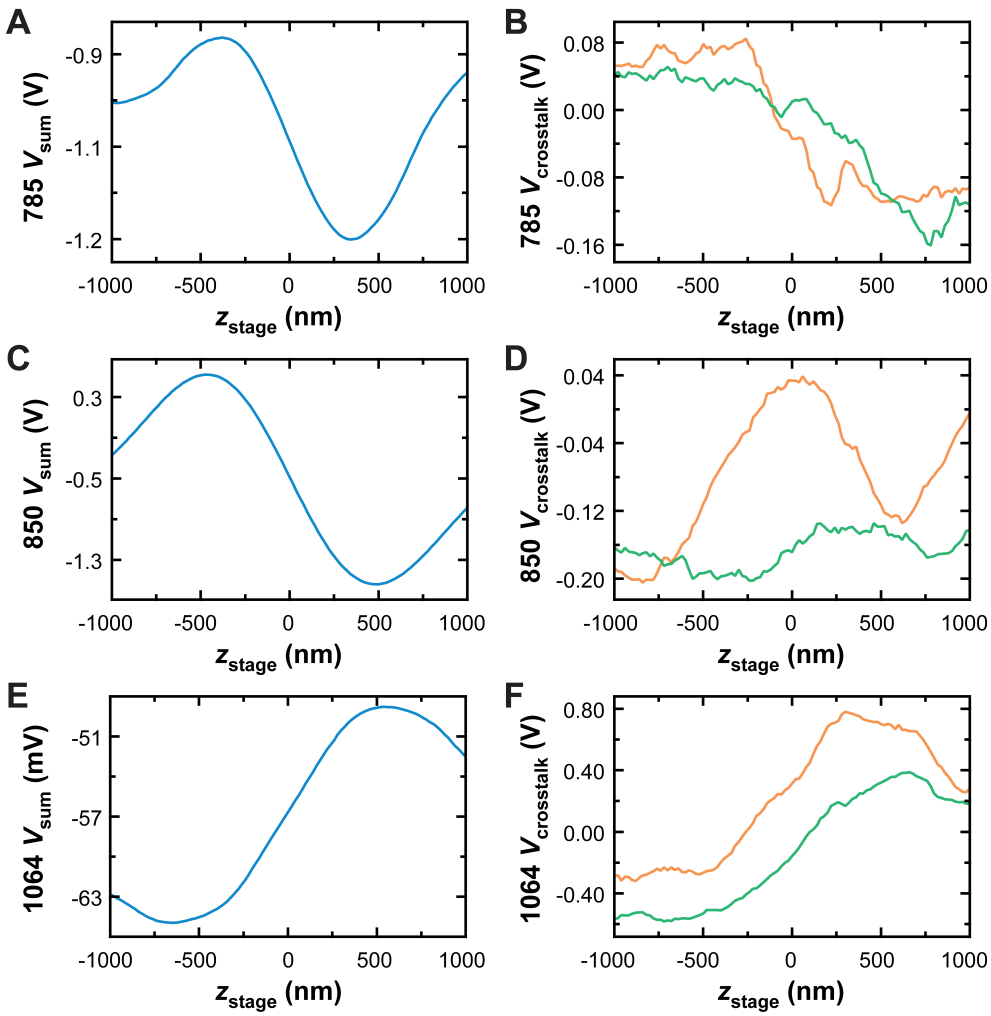

Figure 2.10: QPD signals of a stuck bead translated axially. The x, y, and z signals are displayed in *orange*, *green*, and *blue*, respectively. (A) 785 nm laser QPD sum signal. (B) 785 nm laser QPD crosstalk signals for the trace in (A). (C) 850 nm laser QPD sum signal. (D) 850 nm laser QPD crosstalk signals for the trace in (C). (E) 1064 nm laser QPD sum signal. (F) 1064 nm laser QPD crosstalk signals for the trace in (E).

2.4.5 Laser-crosstalk minimization

We measured the V_{x}, V_{y}, and V_{z} voltage signals of a stuck bead when moving the stage (varying x_{stage}, y_{stage}, and z_{stage}). To minimize the crosstalk during lateral movement (i.e., minimize V_{x} versus y_{stage} and V_{y} versus x_{stage}), we optimized the rotational position of the QPD detectors. The crosstalk values obtained over a range of $\pm$ 200 nm for x_{stage} and y_{stage} region were $< 2\%$ ($\lambda = 785$ nm), $< 3\%$ ($\lambda = 850$ nm), and $< 8\%$ ($\lambda = 1064$ nm). To minimize the crosstalk during axial movement (i.e., minimize V_{x} versus z_{stage} and V_{y} versus z_{stage}), we adjusted the lateral position of the fiber output with the 3D-translation stage upon which it was mounted. The values obtained over a $\pm$ 200 nm range for z_{stage} were $< 1\%$ ($\lambda = 785$ nm), $< 1\%$ ($\lambda = 850$ nm), and $< 13\%$ ($\lambda = 1064$ nm).

2.4.6 PZT-mirror calibration

PZT mirrors were used to steer the trapping and fiducial mark lasers. The mirror controller reads two voltage inputs (V_{x}, V_{y}), which correspond to translational motion of the laser in the specimen plane. Each PZT mirror was calibrated by recording the QPD signals for a grid of PZT mirror voltage inputs [87], e.g., $\pm$ 3 V with 5 iterations per side. At each requested PZT mirror voltage coordinate, (V_{x}, V_{y}), the stage moved correspondingly and laterally scanned and centered a fiducial mark. The centered positions, (X_{cen}, Y_{cen}), were recorded and plotted (Figure 2.11). The distance the laser moved per volts requested from the PZT mirror were determined for each axis, along with the crosstalk values. The volts-to-nm calibrations were deduced from fitting the coordinate data along each axis, as well as from the crosstalk coordinate data. Typical calibration values were are noted in Table 2.4.6.

We measured the calibration error by requesting a grid of coordinates to the PZT stage, scanning a fiducial mark in both x and y via moving the PZT stage, and scanning the fiducial mark again in both x and y via moving the PZT mirror. The scanned signals were compared. Here, the x and y error values for $y_{\mathrm{mirror}} = 0$ and $x_{\mathrm{mirror}} = 0$ are plotted (Figure 2.11). The error values were

Table 2.1: PZT mirror calibration values.

Mirror calibration (nm/V)		
	PZT_{850nm}	PZT_{1064nm}
x	-816.8	-815.14
y	-557.9	699.68
$x_{crosstalk}$	-9.25	-17.88
$y_{crosstalk}$	11.11	-13.36

typically < 10 nm. Each PZT mirror can be rotated by orienting the mirror to different screw holes in its gimbal mount. When in an optimal position, the grid was minimally tilted along the x and y axes.

2.4.7 Differential pointing stability

To determine the pointing stability of each laser, we calculated the differential signal between two lasers as a function of time when monitoring a common object. For example, recording the differential signal between the 785 nm laser and 850 nm laser (e.g., $(x_{785} - x_{850})$ versus time) when monitoring a stuck bead quantifies the relative pointing stability between the 785 nm and 850 nm detection lasers. For the differential measurement between the two detection lasers, the average standard deviation was (0.05 nm, 0.06 nm) in (x, y) for 1–10 Hz (averaged 10 s). For the differential measurement between the trap and bead detection laser, the average standard deviation measured was (0.13 nm, 0.13 nm) in (x, y) for 1–10 Hz (averaged 10 s) (Figure 2.12). Data were smoothed with a gaussian filter that convolved the input 100-Hz data with normalized coefficients derived from Pascal's triangle at the 10^{th} level [88].

2.4.8 Active stage stabilization

We measured the performance during active stage stabilization by recording the 785 nm signal when stabilizing with the 850 nm laser for stage-position lock. We used a DAQ rate of 10.4 kHz, averaged 104 points (to average to 100 Hz), and set the anti-alias filter to 2 kHz. First, the 785 nm laser was centered on a stuck bead ($d \sim 400$ nm) with StageDrift_1_Beam_Multi.vi and the 850

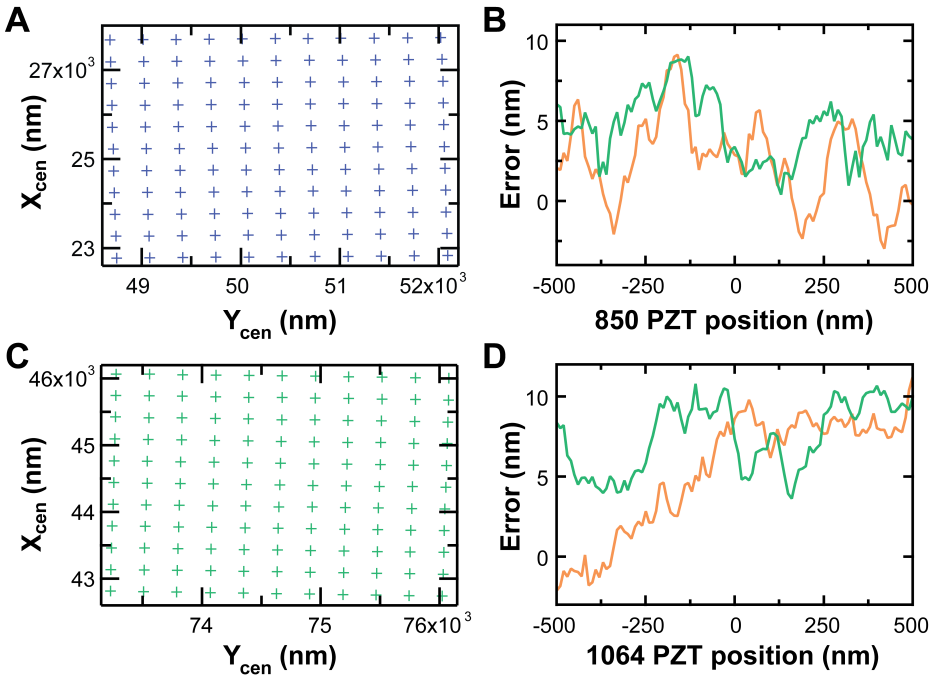

Figure 2.11: PZT mirror calibrations. (A) 850 nm laser PZT mirror calibration. (B) 850 nm laser PZT mirror calibration check. x and y error values are shown in *orange* and *green*, respectively. (C) 1064 nm laser PZT mirror calibration. (D) 1064 nm laser PZT mirror calibration check. Colors as in (B).

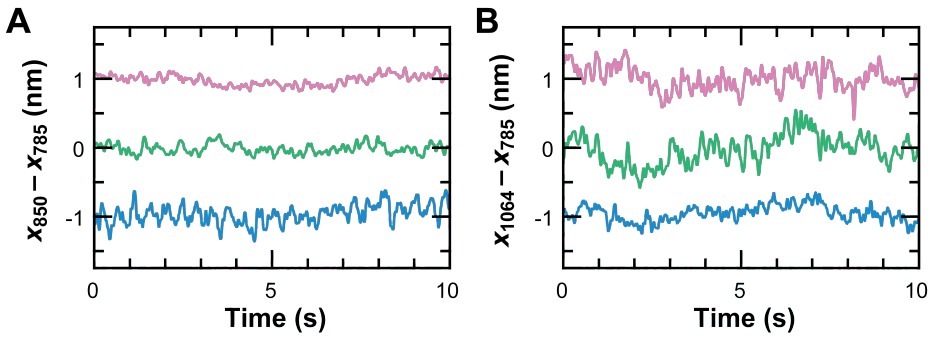

Figure 2.12: Laser differential pointing stability in three dimensions. Difference in the position signals of a common stuck bead. (A) Differential measurements between the 850 nm and 785 nm lasers in x (*fuchsia*), y (*green*), and z (*blue*). (B) Differential measurements between the 1064 nm and 785 nm lasers in x (*fuchsia*), y (*green*), and z (*blue*). 100 Hz data were smoothed with binomial (Gaussian filter) smoothing with 10 smoothing operations applied [88].

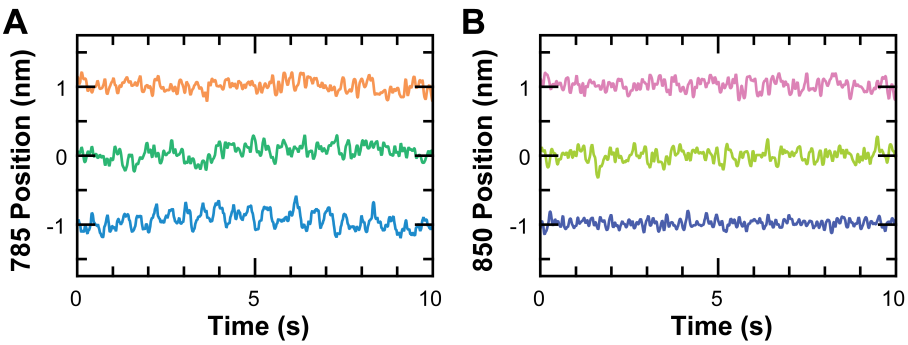

Figure 2.13: Stability with active stage stabilization. While actively stabilizing the stage with the 850 nm laser (in-loop), the position of a stuck bead was independently monitored with the 785 nm laser (out-of-loop). (A) x (*orange*), y (*green*), and z (*blue*) positions of a stuck bead as monitored with the 785 nm laser. (B) x (*fuchsia*), y (*light green*), and z (*dark blue*) positions of a stuck bead as stabilized with the 850 nm laser.

was centered on the same bead with BeamAlignment.vi (PZT 850, detector beam 850) after setting the 850 PZT mirror to (5 V, 5 V). In ZCal2BeamStageStream_Rezero.vi, we enabled stabilization (click the ReZero-enabled button) and turned on the position clamps in x, y, and z (click those 3 buttons). We then observed the 785 (out-of-loop) signals. Positional signals for a bandwidth of 0.1–10 Hz exhibited a standard deviation of (0.1 nm, 0.1 nm, 0.1 nm) in (x, y, z) (Figure 2.13 B). For optimal stabilization, the 785 and 850 were both run at AOM servo voltages of -9 V (although 785 servo is typically -3 V).

2.4.9 Trap ellipticity

The trap ellipticity can be determined by measuring the position of a free bead in a trap and plotting the y position versus x position. The elliptical axes of the trap should align with the x and y axes of the PZT stage. Poor trap ellipticity alignment hampers proper calibration of the trap stiffness. Orientation of the elliptical axes of the trap can be adjusted by rotating the post-fiber trap laser half wave plate. A linear fit of the data should extract a slope < 0.01. Trap ellipticity slope was measured for a bead with $d = 400$ nm at AOM_{1064} voltage of 2 V, to be –0.001 (Figure 2.14).

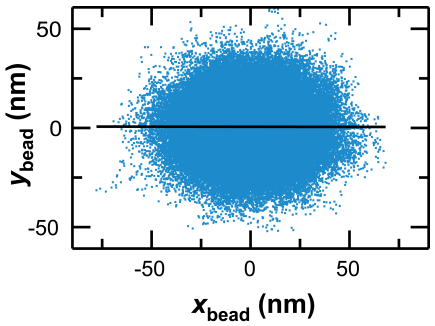

Figure 2.14: Trap ellipticity. (x, y) coordinates of a trapped bead (*blue*) measured with the 785 nm detection laser with 1064 AOM servo at 1 V. Data were linearly fit (*black*).

2.4.10 Trap linearity

To measure the region in which the trap can be approximated by a harmonic potential, we performed a hydrodynamic drag measurement in which the displacement of the bead from the trap center is measured as a function of the viscous drag force exerted by fluid flow. This drag force was produced by moving the sample at a series of constant velocities with the PZT stage. The drag force on an object moving through a fluid at velocity $\dot{y}$ is $F_{\text{drag}} = \beta\dot{y}$, where β is the drag coefficient. The drag coefficient for a sphere near a surface can be estimated by Faxen's law [77]:

$$\beta = \frac{6\pi\eta r_0}{1 - \frac{9}{16}\left(\frac{r_0}{h}\right) + \frac{1}{8}\left(\frac{r_0}{h}\right)^3 - \frac{45}{256}\left(\frac{r_0}{h}\right)^4 - \frac{1}{16}\left(\frac{r_0}{h}\right)^5}, \tag{2.8}$$

which depends on the bead radius r_0, the distance above the surface h, and the viscosity of the liquid η. When the trapping potential is harmonic, the drag force is described by a Hookean spring, defining the relationship between bead displacement and drag force

$$y = -\frac{F_{\text{drag}}}{k_{\text{trap}}} = -\frac{\beta\dot{y}}{k_{\text{trap}}}, \tag{2.9}$$

where y is the displacement of the bead from the trap center. Thus, the trap stiffness may be approximated by the force-displacement relationship. We measured the linear region of the trap $\pm$100 nm range in x and y (Figure 2.15).

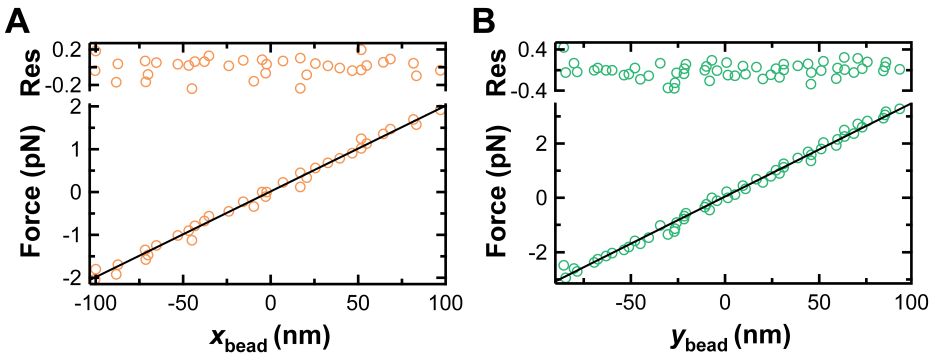

Figure 2.15: Trap linearity. The trapping potential is described by the the Force-displacement relationship. The trapped bead was displaced in either (A) the x or (B) the y direction by a hydrodynamic-drag force. The residual values are displayed in pN.

2.4.11 Stiffness calibration

The stiffness (k_{trap}) of the optical trap for a trapped particle at a particular trap power can be measured by three methods [77]: the Lorentzian Power Spectrum method, the Equipartition Theorem method, and the Hydrodynamic Drag method. When the optical-trapping potential is approximated as a harmonic potential, $U(y) = \frac{1}{2}k_{\text{trap}}y^2$, where y is the displacement of the bead from the trap center, the equation of motion of a trapped particle subject to thermal motion can be solved exactly [77]. At low Reynolds number the equation of motion is

$$\beta\dot{y} + k_{\text{trap}}y = F(t), \tag{2.10}$$

where β is the viscous drag (Equation 2.8) and $F(t)$ is a time-dependent external driving force. The dynamics of a trapped bead undergoing Brownian motion in a parabolic potential well is characterized by a Lorentzian power spectrum [89]:

$$S_{\text{yy}}(f) = \frac{k_{\text{B}}T}{2\pi^3\beta(f_0^2 + f^2)}, \tag{2.11}$$

$$f_0 = \frac{k_{\text{trap}}}{2\pi\beta}, \tag{2.12}$$

where f_0 is the corner frequency. The mean square displacement of the particle is

$$\langle y^2 \rangle = 2\pi \int_0^{+\infty} S_{\text{yy}}(f)df. \tag{2.13}$$

By the Equipartition Theorem, the mean square displacement is [77]:

$$\langle y^2 \rangle = \frac{k_{\text{B}}T}{k_{\text{trap}}}. \tag{2.14}$$

where k_{B} is Boltzmann's constant and T is the temperature.

From equations (2.9), (2.13), and (2.14), three different methods were used to calibrate the k_{trap} dependence on trap servo voltage.

We used uncoated, 400 nm diameter polystyrene beads to measure the trap stiffness using the power spectrum, equipartition, and hydrodynamic drag methods (Figure 2.16). The three stiffness

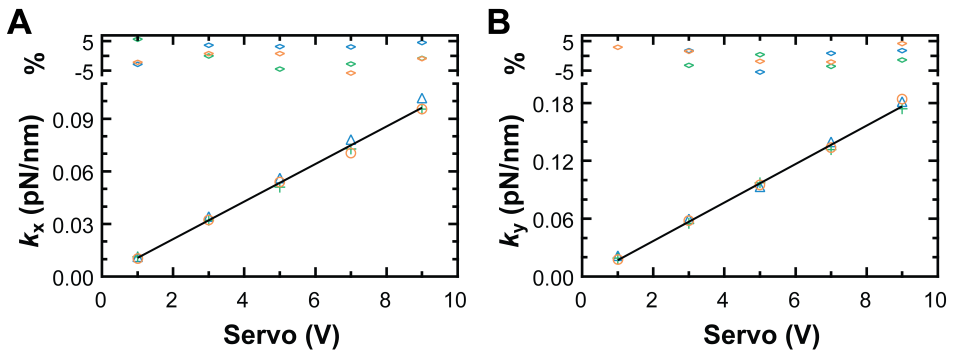

Figure 2.16: Stiffness calibration of $d = 400$ nm beads. The three methods of equipartition theorem (*orange*), power spectrum (*green*), and hydrodynamic drag (*blue*), were used to calibrate the stiffness-to-volt values. The data were averaged and fit to a line. The percentage difference of the measured values to the fit values is plotted (%). (A) Stiffness calibration in the x axis. (B) Stiffness calibration in the y axis.

values at each servo voltage agreed to ±5%. We also calibrated the trap stiffness of streptavidin-coated 320 nm diameter beads using the power spectrum and equipartition methods. The power spectrum and equipartition methods agreed to within 10% (10%) for 400 nm (320 nm) beads. To check the calibration error, three beads were used (Figure 2.17).

2.4.12 Stiffness versus height

We measured the trap stiffness as a function of bead height above the surface. The trap stiffness was found to decrease by $< 15\%$ at 1 μm above the surface in y and remained constant in x.

2.4.13 Sensitivity

The sensitivity of the QPD signal from a bead or fiducial mark depends on the axial position relative to the laser focus. The sensitivity was characterized by measuring the lateral signals of a fiducial mark at a range of set axial stage positions (e.g., –1000 nm$< z_{\text{stage}} <$ +1000 nm). The lateral signals were fit to a 7th order polynomial (e.g., $V_{\text{y}}(y) = A_0 + A_1 y + A_2 y^2 + \ldots + A_7 y^7$). The sensitivity (V per nm) can be described by the inverse of the coefficient of the linear term, A_1^{-1}

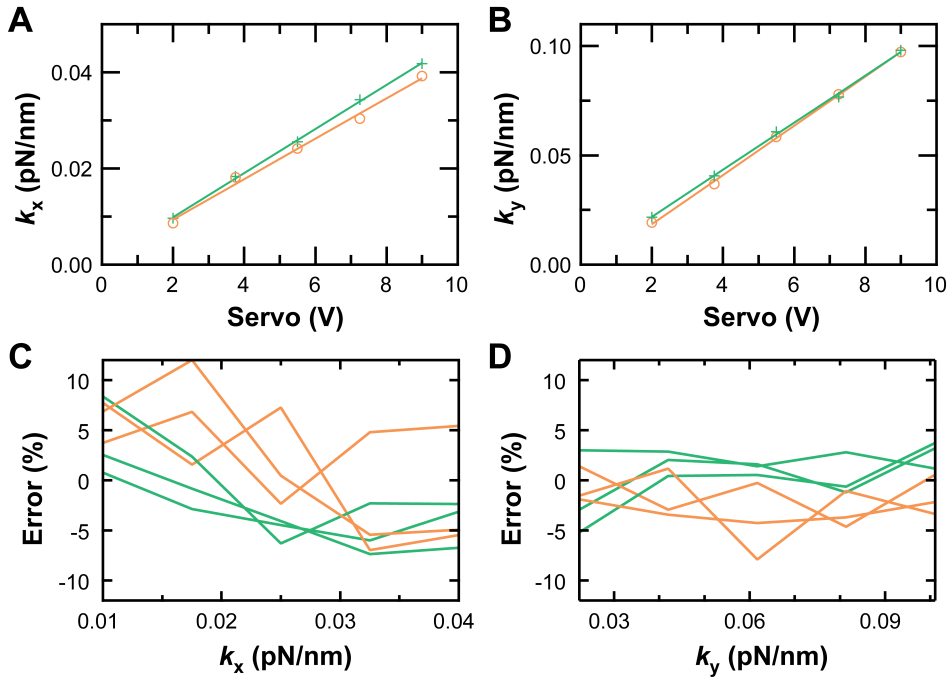

Figure 2.17: Stiffness calibration of $d = 320$ nm beads. The equipartition theorem (*orange*) and power spectrum (*green*) were used to calibrate the stiffness-to-volt values. The data were averaged and fit to a line. (A) Stiffness calibration in the x axis. (B) Stiffness calibration in the y axis. (C) The % error when the k_x stiffness calibration was tested on 3 beads. (D) The % error when the k_y stiffness calibration was tested on 3 beads.

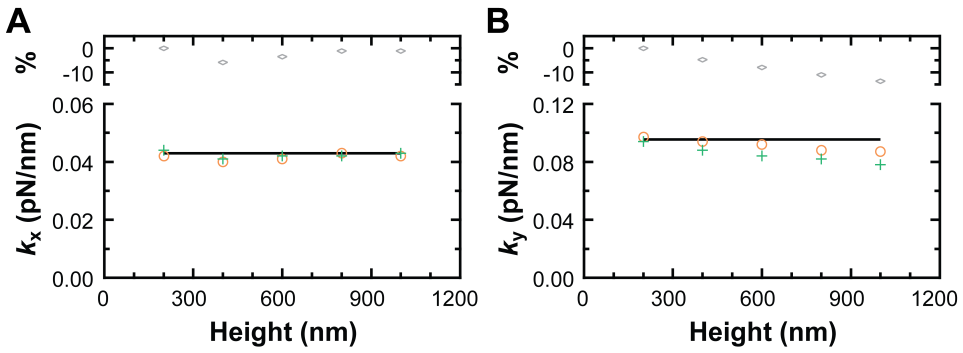

Figure 2.18: Trap stiffness versus height. (A) The trap stiffness in the x axis as measured by the equipartition method (*orange*) and the power spectrum method (*green*). (B) The trap stiffness in the y axis as measured by the equipartition method (*orange*) and the power spectrum method (*green*). Constant trap stiffness values (*black*) displayed for reference.

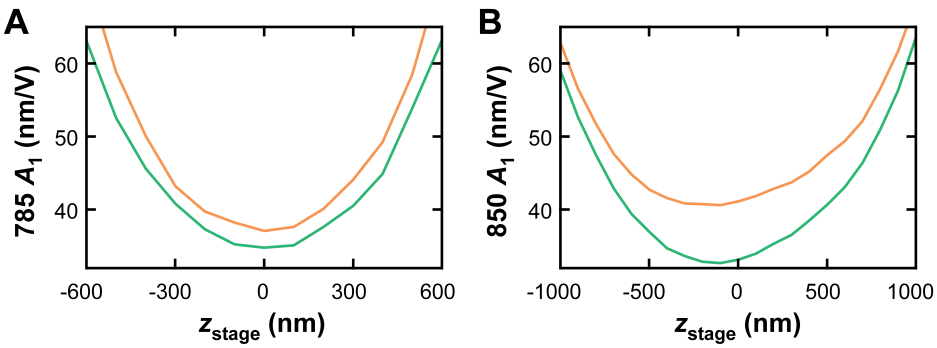

Figure 2.19: Lateral sensitivity measurements of a stuck bead. The A_1 coefficients in x (*orange*) and y (*green*) of a 400-nm diameter stuck bead as a function of stage position.

(Figure 2.19).

For a trapped, free bead, the sensitivity should not vary as a function of height above the surface. The A_1 coefficient of a 400-nm diameter trapped, free bead in water increased by 5% in both x and y at a 1000-nm height above the surface (Figure 2.20).

2.4.14 Stretching long DNA

The force versus extension relationship requires measurements of both force and extension in the direction of the applied stretch, which lies at a variable angle θ in the x-z plane and changes during the course of an experiment. From the geometrical relationship of these parameters to the interferometer signals, the axial position of the bead (x_{bead}), the DNA extension (x_{DNA}), and the force exerted by the bead on the DNA (F) can be derived [63]. The force-extension curve for stretching a relatively long DNA molecule (e.g., $L >> L_{\text{p}}$) can be described by the worm-like chain model (Equation 2.1). Fitting to this model, one can extract the persistence length (L_{p}) and contour length (L), which is useful for distinguishing between beads tethered to the surface via one DNA molecule or via multiple DNA molecules.

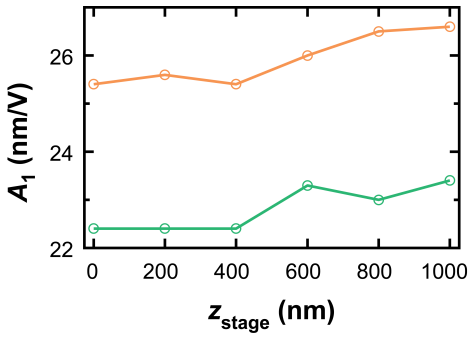

Figure 2.20: Lateral sensitivity measurements of a free bead. The A_1 coefficients in x (*orange*) and y (*green*) of a 400-nm diameter free bead in water as a function of stage position.

2.4.15 Trap fiber coupling

Because the trap stiffness was dynamically changed by varying the requested 1064 servo voltage (i.e., PD_{1064} voltage), the fiber coupling needs to be such that the coupling efficiency is sufficient over a range of AOM voltages. This was done by optimizing the fiber coupling of the trapping laser at an AOM voltage of 0.6 V such that the PD_{1064} read > 7 V. When fiber alignment is optimized, at a servo value of 0.9 V, the PD_{1064} should be > 10 V. To optimize fiber coupling, the positioning of the laser beam was adjusted via two mirrors upbeam of the fiber and the positioning of the fiber tip was adjusted via its mount [90].

2.4.16 Trap power

The power of the optical trap prior to entering the microscope should depend linearly on the 1064 nm laser AOM Servo voltage. We measured the trap power versus servo voltage, fit the data using a linear fit, and retrieved a slope of 70 mW/V (Figure 2.21).

2.4.17 Free-bead measurement

The stability of a trapped, free bead was measured to quantify the trapping stability, independent of the PZT stage. A 320-nm diameter free bead was trapped and the QPD signal was analyzed by calculating the integrated fluctuations. The integrated fluctuations ($\Delta f = 0.02$–10 Hz)

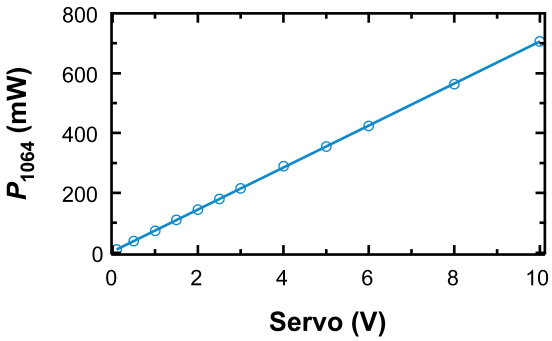

Figure 2.21: Trap power versus servo voltage.

was 0.12 nm^2 and 0.02 nm^2 at trap stiffnesses of 0.09 pN/nm and 0.23 pN/nm, respectively.

2.4.18 DNA-tether stability

We measured the stability of a trapped bead tethered to a surface via a DNA molecule (Figure 2.22). For more data, see Section 3.3. Either a force clamp or "pseudo force clamp" (see Section 2.6) was implemented. Typical settings were a force of $F = 6$ pN, bead diameter size of $d = 320$ nm, DNA length of $L = 1007$ nm, data acquisition rate of 10 kHz, anti-aliasing low-pass filter of 2 kHz, in Wash Buffer (see Section 2.5.5). For these settings, we demonstrated a DNA contour length stability of 0.50 ± 0.01 nm ($\Delta f = 0.1$–10 Hz).

2.5 Sample Preparation

2.5.1 Fiducial mark fabrication

We primarily used two methods to make fiducial marks. For both methods, we constructed epoxy-rigidified flow chambers (internal volume 15 µl) for enhanced stability using double-stick tape (3M) as a spacer and 5-min epoxy (Devcon) for rigidity. For taking diagnostics of the trapping instrument, we used a 400-nm diameter bead baked onto a cover slip.

For studying RecBCD with active stabilization we used a second method, fabrication of fiducial marks onto glass cover slips. An array of low-index glass posts of 1 µm diameter with 15 µm-

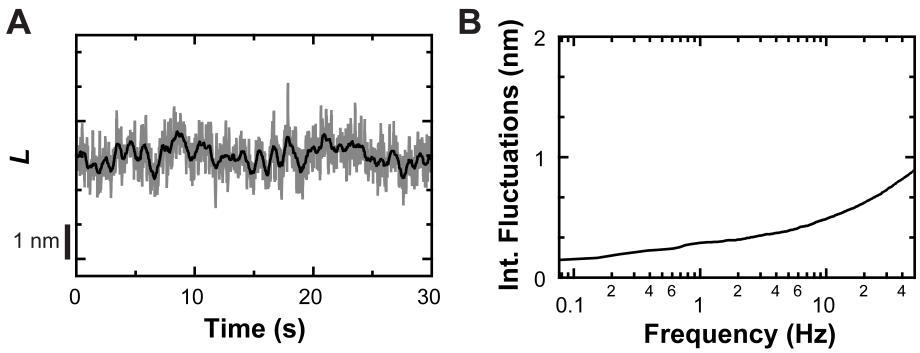

Figure 2.22: Stability of a DNA tether at 6 pN. (A) Contour length versus time. Data were smoothed to 10 Hz (*grey*) and 1 Hz (*black*). (B) Integrated fluctuations of the record in A.

spacing were fabricated on glass cover slips using hydrogen silsesquioxane and *e*-beam lithography [78, 90]. After nanofabrication and use in single-molecule assays (e.g., the RecBCD tethered-particle assay, Section 2.5.5), the nanofabricated cover slips were re-used after cleaning with a 10-min piranha etch (100 mL sulfuric acid and 15 drops hydrogen peroxide at 80 °C). Cover slips were recovered (>20 times) and cleaned after use by soaking the flow chamber in water for 24 h, then boiling for 1 h (to remove the cover slip), and piranha cleaning the cover slip for 10 min. Surface chemistry after such cleaning was compatible with single-molecule biophysics experiments.

2.5.2 Bead preparation

To prepare the beads for free-bead and tethered-bead measurements, the beads were transferred to new buffer and were monodispersed with sonication. When using protein-coated beads, it was important to reduce the amount of free protein in solution by repeat washings which involved: i) mixing beads with 0.4 % Phos-Tween buffer, ii) centrifuging the bead-buffer solution, and iii) removing the supernatant. After the repeat washings, the beads were reconstituted to the desired concentration in the desired final buffer (usually Wash Buffer). Next, the beads were checked for monodispersion with an optical microscope and sonicated until adequately monodisperse.

2.5.3 Synthesis of DNA constructs

DNA was prepared with polymerase chain reaction (PCR) (EMD Chemicals, KOD Hot Start DNA Polymerase) with M13mp18 plasmid template and with one biotin-labeled primer and one unlabeled primer for DNA for the RecBCD tethered-bead assay. This created a blunt-ended DNA molecule (L = 2413 nm, 993 nm) with only one biochemical linkage for attachment to the streptavidin-coated optically-trapped bead.

To make tailed DNA we cut the 993-nm-length blunt-ended DNA with BsmBI restriction endonuclease (New England Biolabs) at a restriction site such that the purified product had a length of $L = 901$ nm. We purchased DNA oligos to make tailed substrates: one with a $3'$ poly-dT tail (dT = 6) and a $5'$ end that was complementary to the BsmBI overhang, the other with a $5'$ poly-dT tail (dT = 6, 8, 10, or 20) and a sequence that was complementary to the first oligo up until the $5'$ end. The two oligos were annealed at 70 °C, slowly cooled (4 °C increments held for 30 s) to room temperature, and ligated using T4 DNA ligase (Invitrogen) to the cut DNA (16 °C for 16 h, 50:1 molar ratio of tailed substrate to cut DNA). The final dsDNA length of the tailed substrates was 908 nm. We gel purified the product and concentrations were determined, as above. To verify that the final product was a tailed DNA we further cut an aliquot of the product with a DrdI restriction endonuclease (New England Biolabs) at a site upstream of the BsmBI site (Figure 2.23A). This produced an 829-nm-length DNA molecule containing the biotin label, and a 78-nm-length DNA molecule with the tailed substrate. If the digestion or ligation were faulty then bands would appear at other lengths (i.e., a 164-nm length indicated the blunt-ended DNA molecule and a 72-nm length indicated the DNA molecule with the BsmBI cut end and no ligation). There were multiple different tailed substrates that were created (see Figure 2.23B): a GC-rich substrate, an AT-rich substrate, a substrate with a mixed sequence, and cross-linked substrates.

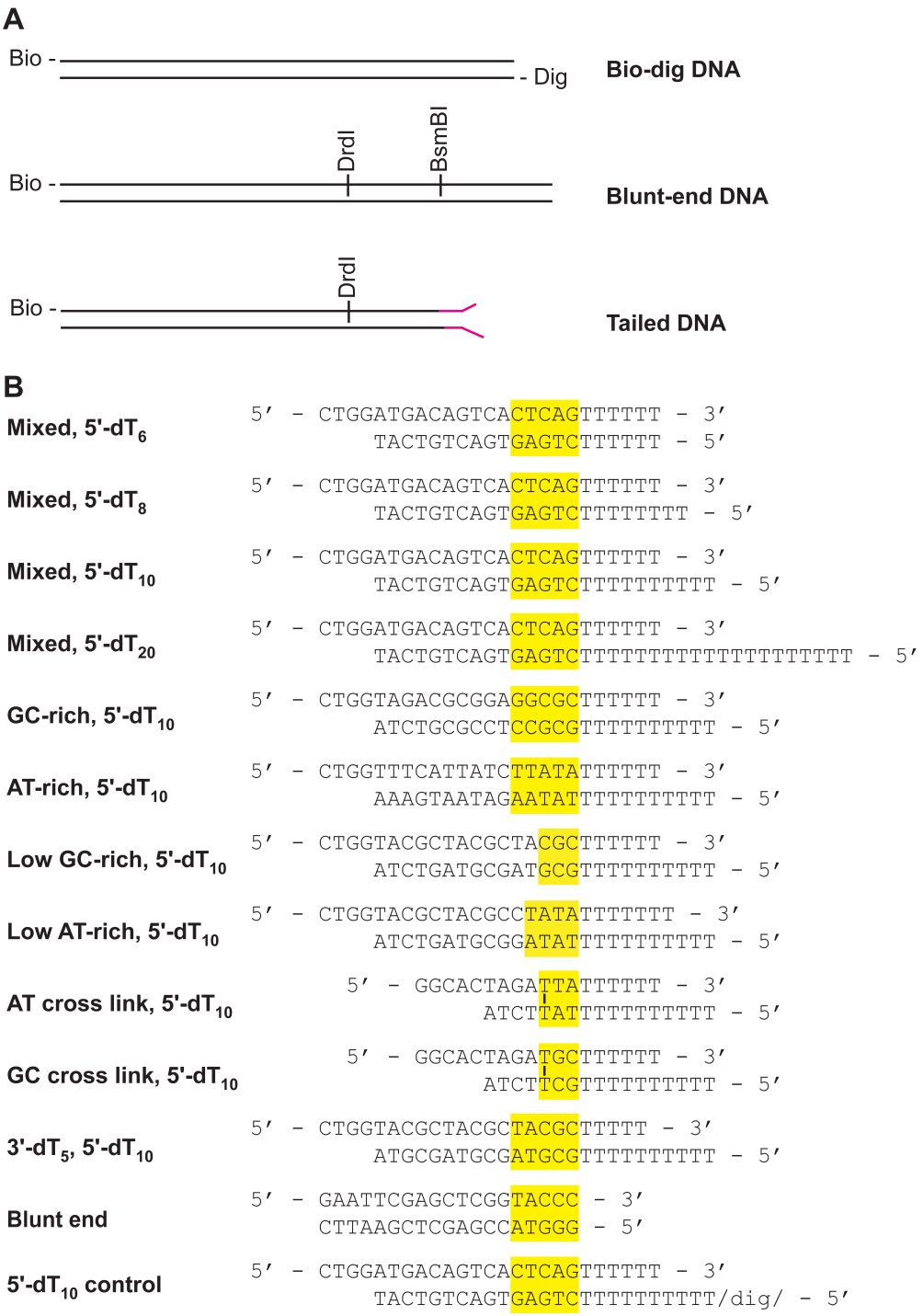

Figure 2.23: DNA substrates. Adapted from Carter (2008) [90]. (A) Three main types of DNA were used to tether streptavidin-coated beads to the surface via either a digoxigenin-antidigoxigenin linkage or via RecBCD bound to the surface: i) Bio-dig DNA; ii) Blunt-ended DNA; and iii) Blunt-ended DNA modified with noncomplementary ssDNA tails on the RecBCD-binding end. DNA constructs were labeled with biotin (Bio) and digoxigenin (Dig) tags and contained restriction sites as marked. (B) DNA end sequences of the (dT)-tailed DNA constructs that were ligated to create the Tailed DNA in A. The sequence of the RecBCD-binding end of the Blunt-ended DNA is also shown.

2.5.4 DNA tethered-particle assays

Our DNA tethered-particle assay was adapted from those in earlier single-molecule studies [31]. Double-stranded DNA was prepared by polymerase chain reaction using one digoxigenin-labeled and one biotin-labeled primer (Integrated DNA Technologies, Coralville, IA). These labels enabled us to attach one end of a DNA molecule (L = 1007 nm) to a streptavidin-coated bead (320-nm diameter; Spherotech, Lake Forest, IL) and the other end to an antidigoxigenin-coated coverslip. Coated coverslips were made by incubating 20 μg/mL antidigoxigenin antibody (from sheep, Roche Applied Science, Indianapolis, IN) suspended in 0.1 M sodium phosphate buffer for 1 h in flow chambers. Bead-DNA complexes were made by incubating streptavidin-coated beads (920 pM) at a 9:1 molar ratio with labeled DNA at room temperature. After washing the flow chamber with Wash Buffer, the bead-DNA mixture was flowed into the chamber and allowed to incubate for 1 h before washing again. Coverslips were reused (>20 times) by soaking the flow chamber room temperature water overnight and then in boiling water for ~1 h (to remove the coverslip) and then cleaning the coverslip with a 10-min Piranha etch.

2.5.5 RecBCD tethered-particle assay

Our RecBCD tethered-particle assay was adapted from those in earlier single-molecule studies [30, 91, 92]. We used the RecD biotin-tagged RecBCD derivative (RecBCD-bio), which has a biotin moiety near the carboxy terminus of the RecD subunit. This enzyme was shown to be functional *in vivo* [93] and exhibited nuclease, helicase, and DNA-dependent ATPase activities *in vitro* analogous to those of the wild-type enzyme [91].

This protocol is summarized below and a more detailed description is included in Appendix A.1. First, flow chambers were assembled using the piranha-cleaned, nanofabricated post cover slip described (Section 2.5.1). Next, bead-DNA complexes were prepared. Streptavidin-coated carboxyl beads (Spherotech, 320-nm diameter) were sonicated, then incubated for 1 h with DNA (9:1 mol ratio, 920 pM beads) in Wash Buffer [25 mM Tris (pH 7.5), 1 mM $Mg(CH_3COO)_2$, 1 mM NaCl,

1 mM dithiothreitol, 0.4% Tween 20 (Sigma-Aldrich, St. Louis, MO), and 3 mg/ml bovine serum albumin [BSA; concentration is that prior to filtration through a 0.22-μm filter; Millipore, Billerica, MA)]. Concurrent to bead-DNA preparation, RecBCD surfaces were prepared. Three steps were performed before introducing the bead-DNA complexes in the flow chamber, with the flow-chamber washed twice with 200 μl Wash Buffer and allowed to sit for 10 min after each step: (i) biotinylated BSA (Vector Laboratories, Burlingame, CA) at 100 mg/ml in 100 mM sodium phosphate buffer (pH = 7) was incubated within the flow chamber for 20 min at room temperature to promote adsorption, (ii) 5 mg/ml streptavidin (Vector Laboratories, Burlingame, CA) was incubated for 20 min, and (iii) 15 nM RecBCD-bio was incubated for 2 h. Finally, the bead-DNA mixture was introduced and incubated for 40 min and then washed with Wash Buffer. Conformational dynamics of the RecBCD·DNA complex could then be observed with these RecBCD·DNA tethers.

DNA unwinding by RecBCD was initiated by introducing Wash Buffer supplemented with 2 μM ATP, 1.1 mM *Escherichia coli* single-stranded binding protein (SSB) (Promega, Madison, WI), and an oxygen-scavenging system (6 mg/ml glucose (MP Biomedicals, Solon, OH), 0.2 mg/ml glucose oxidase (Roche Applied Science, Indianapolis, IN), 30 units/ml catalase), unless otherwise stated. Where indicated, 2 μM ATP was substituted with 2 mM of the following compounds (purchased from Sigma-Aldrich, St. Louis, MO): adenylyl imidodiphosphate (AMPPNP), adenosine diphosphate (ADP) with and without inorganic phosphate (P_i), adenosine 5′-O-(3-thiotriphosphate) (ATPγS), or ADP complexed with beryllium fluoride (ADP·BeF_x).

2.6 Data Acquisition

2.6.1 Measuring DNA contour length

Positional data of the trapped bead and fiducial mark were each collected on a QPD (250 kHz bandwidth with custom electronics; ~40 μW laser power at detector). Each QPD detected lateral motion from the normalized intensity difference between pairs of adjacent quadrants and axial motion from the offset-amplified sum signal of the four quadrants. The signals were filtered with

an 8th-order, low-pass, elliptic filter (Frequency Devices), and digitized at either 4 or 10 kHz with a 16-bit, 20-V-range data acquisition card (National Instruments, PCI-6052E). After digitization, calibration curves were used to convert the x, y, and z voltage signals into positional units (2.4.4). Customized software was written in LabVIEW (National Instruments, version 7.1) on a computer (Dell Dimension 9200) with a fast processor (Intel Core2-Duo, 2.66 GHz).

To measure DNA contour length (L) we first determined the axial position of the surface by monitoring the bead detection laser sum signal of a trapped, tethered bead as a function of z_{stage} as the bead was brought into contact with the cover slip surface [70]. The axial trapped-bead-position calibration was performed, and then the stage was lowered 300 nm. We located the lateral tether point position by performing a two-dimensional elasticity procedure, which also returned the persistence length (L_{p}). Bead-DNA complexes anchored by multiple DNA molecules, as determined by a low persistence length, were not studied. Next, we centered the fiducial-mark detection laser on a nearby fiducial mark by steering this laser with a PZT mirror and measured the volts-to-position calibration of the fiducial mark. Finally, we measured L as a function of time by stretching it along the y axis by positioning the PZT stage to a specified force, while moving the fiducial-tracking laser by the corresponding distance. The sample was actively stabilized using a software-based feedback loop with a 100 Hz update rate and 0.05 proportional gain. Software simultaneously measured trapped bead and fiducial mark positions and calculated DNA length [63].

2.6.2 Employing a force clamp

To study RecBCD motion, we applied a "pseudo force clamp" with active stage stabilization (Figure 2.24). RecBCD unwinding of DNA causes motion of the bead relative to the trap center, creating a force on the bead by the trap. To keep the force within 15% of the initial force value, we allowed the trapped bead to stray ± 10 nm from the clamp position, which was set to 70 nm. When the bead position differed >10 nm from the clamp position value, the stage was triggered to reset the bead position back to the clamp value and the fiducial detection laser was moved by a corresponding distance by a PZT mirror. Raw data were collected at either 4 or 10 kHz, filtered

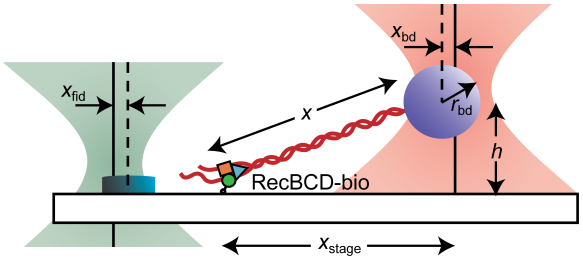

Figure 2.24: High-precision RecBCD optical-trapping assay. Figure from Carter (2008) [90]. A DNA molecule is stretched between the RecBCD helicase and an optically-trapped bead. One detection laser (*red*) measures the bead position (x_{bd}), which is used to calculate DNA length. The other detection laser (*green*) measures the position of a fiducial mark (x_{fid}), which is used to stabilize the surface relative to the optical-trapping laser. This RecBCD assay achieves 0.5-nm precision in DNA length measurements ($\Delta f = 0.1$–1 Hz).

using an 8th-order, low-pass, elliptic filter, and digitized with a 16-bit, 20-V-range data card.

2.7 Data Analysis

2.7.1 Quantifying fluctuations and conformational dynamics

To quantify the conformational dynamics of the RecBCD·DNA complex, we measured the integrated fluctuations over the frequency bandwidth 0.07–10 Hz. First, we measured ~200-s records of tethered nanoparticles (e.g., DNA contour length versus time). Next, we selected 30-s regions with minimal low-frequency noise (e.g., regions where the average contour length was constant). We calculated the power spectrum of 30 s of the raw data for a scaled power-spectrum function (see Appendix B.1 (22)), a Hann window, and the largest window size possible for the time span. Next, we calculated the square root of the definite integral of the power spectral density over a specified bandwidth (e.g., 0.07 Hz to f) to give the integrated fluctuations as a function of frequency, f. Finally, we used the integrated fluctuations at 10 Hz ($f = 10$ Hz; e.g., integrated over the frequency bandwidth $\Delta f = 0.07$–10 Hz) to characterize the amplitude of the fluctuations and conformational dynamics.

We used several criteria in the selection of our data. Although our assay featured high precision in measuring changes in DNA contour length, each individual data record contained greater levels of

absolute position uncertainty, partly due to variations in bead size (C.V. 2.2% for 320-nm-diameter streptavidin-coated beads). Data that were unusually noisy, designated "Type 2" noise [90], was not included in the analysis. Furthermore, we occasionally observed tethers that appeared to lack (dT) tails in our prepared samples of RecBCD bound to DNA with 3′-$(dT)_6$ and 5′-$(dT)_{10}$ ssDNA tails. To increase our confidence that only molecules with properly-ligated (dT) tails were included in our analysis, we selected contour-length records that were above a certain contour length threshold value at the beginning of recording. The threshold value was approximately 903 nm for DNA tethers that were 903 nm long.

2.7.2 Determining statistical significance between data sets

The statistical significance between data sets was determined using a t-test using the two-tailed distribution and heteroscedastic assumptions. Since not all sample sizes were equal, we used a t-test that assumed that the two population variances were different. This analysis assumes a null hypothesis that the two data sets being compared are from the same population. This t-test measures differences between data sets (but does not test equivalence) and calculates a P-value (P), the probability of obtaining a test statistic at least as extreme as the one observed. The P-value serves as an indicator of the confidence in which the compared data sets originated from the same population (e.g., $P < 0.05$ indicates that there is a 5% chance of rejecting the null hypothesis when it is true).

2.7.3 Quantifying distinct spikes within the conformational dynamics data

To quantify the spikes observed within the conformational dynamics data, we developed a computer algorithm to detect spikes. The main input of the algorithm was the spike size (δ_{spike}), defined by the user. We typically used a spike size that was the mean standard deviation of our control data, the conformational dynamics of RecBCD bound to blunt-ended DNA, which was 0.87 $\pm$ 0.08 nm for a 30-s DNA contour length (L) trace smoothed to 1 Hz with a Savitzgy-Golay window. This corresponds to a 2.6-bp spike. The criteria for a "spike" included: i) a change in DNA length

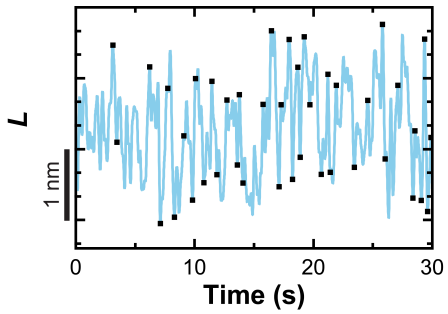

Figure 2.25: Quantifying spikes within the RecBCD·DNA conformational dynamics. An example data record of the DNA contour length of an example trace of RecBCD bound to DNA (*light blue*; cross-linked DNA with 3′-$(dT)_6$ and 5′-$(dT)_{10}$ tails) with spikes identified with an automated algorithm (*black dots*). The contour length data were taken at $F = 6$ pN and smoothed with a Savitzky-Golay window to 1 Hz. Here, 41 spikes were identified.

that had an absolute value that was greater than or equal to the specified spike size ($\Delta L \geq \delta_{\text{spike}}$) and ii) that the spike displayed a local maximum or minimum (see Figure 2.25). These criteria were used because the spikes were neither uniform in size nor duration. The total number of spikes per data trace were then noted. The computer algorithm was written in Igor Pro (WaveMetrics, Portland, OR).

Chapter 3

RecBCD Conformational Dynamics and Mechanism

3.1 Helicase Function and Mechanism

Helicases have been identified in various prokaryotes and eukaryotes, as well as in bacteriophages and viruses [94, 95]. Helicases and translocases function in nearly all aspects of DNA and RNA metabolism [96]. They are involved in various biological functions, including DNA replication, recombination, and repair; transcription; translation; ribosome synthesis; RNA maturation and splicing; and nuclear export.

Helicases unwind duplex DNA, RNA, and DNA-RNA hybrid molecules. To understand the mechanisms by which helicases function at the molecular level requires information on the mechanochemical coupling that occurs during nucleic-acid unwinding. To catalyze unwinding, a helicase cycles through a series of energetic (conformational) states driven by the binding and/or hydrolysis of NTP and subsequent release of products ($NDP + P_i$) [94, 97].

3.1.1 Structural features common to all helicases

Helicases and nucleic acid translocases were originally classified into five different superfamilies (SF) defined by several conserved structural motifs [98]. However, subsequent studies indicate that these motifs are present in enzymes that are not helicases and instead more generally identify nucleic-acid-stimulated NTPases [21, 96]. A development of the classification incorporates a sixth superfamily and descriptors of directionality indicated as either type A and type B, which describe translocation along DNA in the $3' \rightarrow 5'$ and $5' \rightarrow 3'$ directions, respectively [96].

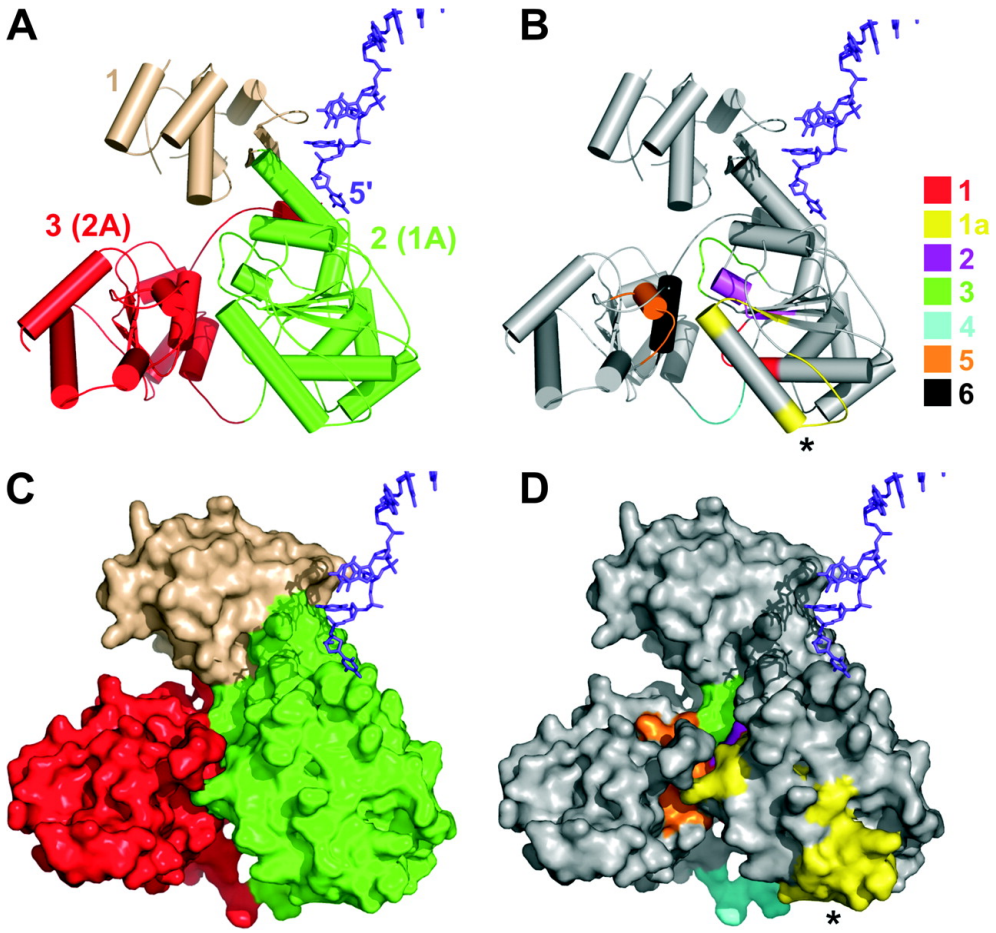

Figure 3.1: Locations of motifs in the RecD protein. Reproduced from Dillingham and Kowalczykowski (2008) [23] with permission from the American Society for Microbiology. (A) Cartoon representation of the three-subdomain structure of RecD. Subdomain 1 (*wheat*) contacts the RecC protein. Subdomains 2 (*green*) and 3 (*red*) are equivalent to subdomains 1A and 2A of SF1 DNA helicases. The 5′ ssDNA tail (*deep purple*) is shown approaching these core helicase domains. (B) Cartoon representation with the seven conserved helicase motifs indicated. (C) Surface representation colored as described above for A. (D) Surface representation colored as described above for B.

The conserved motifs coordinate the conversion of chemical energy to mechanical energy. They couple NTP binding and hydrolysis to enzyme conformational changes [99]. The structural motifs are a signature for core domains that form tandem RecA-like folds found near the NTPase catalytic site (Figure 3.1). They feature conserved residues involved in the binding and hydrolysis of ATP equivalent to the Walker A and B boxes of many ATPases [100] and a conserved arginine residue, termed an "arginine finger," required for energy coupling [101]. The core domains of SF1 and SF2 helicases, made up of subdomains 1A and 2A, are made up of a single polypeptide chain containing two RecA-like folds (Figure 3.2). The core domains of the other superfamilies are hexameric (or double-hexameric) rings formed from 6 (or 12) individual RecA folds. The core domains shown in Figure 3.2A constitute the minimal translocation motor.

3.1.2 Unwinding mechanisms of helicases

DNA helicases use the energy from NTP binding and hydrolysis to unwind DNA in a directional manner. Under physiological conditions (7.8 mM ATP, 1.04 mM ADP, and 7.9 mM P_i in *Escherichia coli* [3]), the free energy of ATP hydrolysis is –47.5 kJ/mol or –19.2 k_BT. The interaction between the helicase and the DNA that occurs when NTP binding and hydrolysis is coupled to directional translocation can be described by various models.

Since different DNA helicases exhibit differences in their mechanistic characteristics, such as in their translocation rate, processivity, directionality, step size, ATP-coupling stoichiometry, and oligomeric state, several models have been proposed to describe general helicase unwinding mechanisms [21]. In the "active" versus "passive" models, the helicase either plays a direct or indirect role in destabilizing its double-stranded DNA (dsDNA) substrate [94, 102, 103] (Figure 3.3). In the active model, the helicase directly destabilizes the dsDNA at the single-stranded-DNA-double-stranded-DNA (ssDNA-dsDNA) junction. This model requires that the helicase possess at least two DNA binding sites [94, 104] and can either interact directly with the dsDNA at the junction to destabilize the dsDNA, or can act indirectly by applying a torque on the duplex region through an NTP-induced conformational change [94, 105]. In the passive model, the helicase binds ssDNA

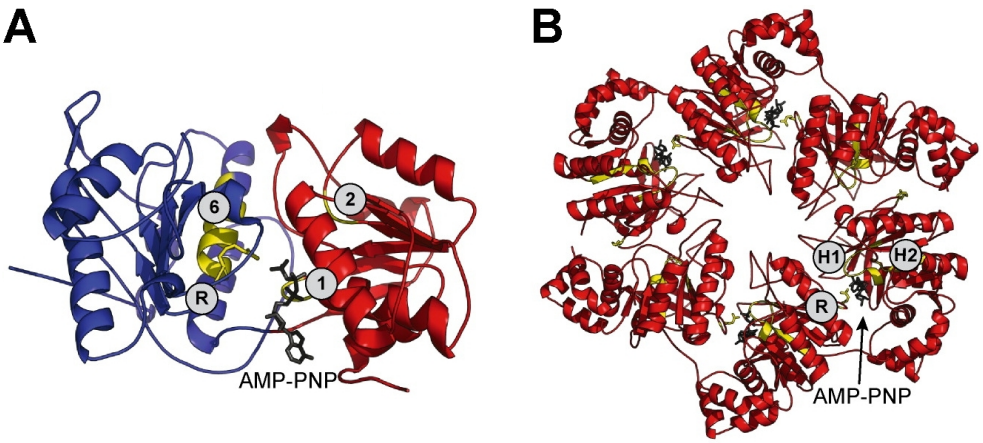

Figure 3.2: Representative core structures found in helicases and translocases. Adapted from Singleton *et al.* (2007) [96]. Universal structural elements involved in the binding and hydrolysis of NTP, and the coupling of this activity to conformational changes are shown in *yellow*. (A) The SF1 and SF2 enzymes contain a monomeric core formed from the tandem repeat of a RecA-like fold. An NTP analog (*black*) is bound at the interface of the core domains. This representative structure is the core of PcrA helicase from SF1. (B) The SF3-6 enzymes contain a core that consists of six individual RecA- or AAA+-like domains (*red*) arranged in a ring. Six nucleotide-binding pockets are present, one at each domain interface, and four are occupied with NTP analogs (*black*). This representative structure is of T7 gene 4 protein from SF4.

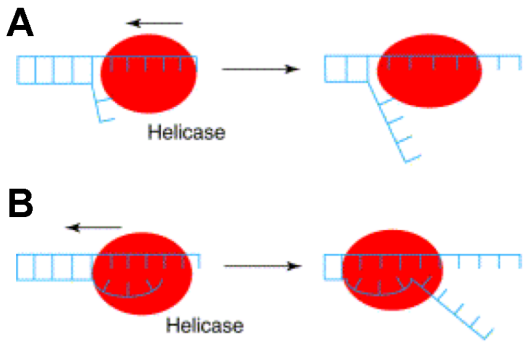

Figure 3.3: Passive and active mechanisms for helicase unwinding. Reprinted from from Soultanas and Wigley (2001) [108], with permission from Elsevier. (A) In the passive mechanism, the helicase does not make direct contacts with the duplex. Instead, it operates by trapping ssDNA at a thermally fraying ssDNA-dsDNA junction. (B) In the active mechanism the helicase interacts directly with the dsDNA and destabilizes the duplex, thus 'actively' unwinding the strands.

available when thermal fluctuations partially open the DNA at the ssDNA-dsDNA junction. These end-fraying thermal fluctuations have lifetimes of less than 1 ms [106, 107]. A passive mechanism requires the helicase to interact with the ssDNA using at least a single site and to translocate unidirectionally along ssDNA toward the duplex [94].

The extent to which the helicase destabilizes the junction can be described by its "interaction potential" [109, 110], which describes how the presence of the helicase modiÞes DNA opening. If the position of the helicase is given by n (indexing the base to which the helicase is bound) and the position of the ssDNA-dsDNA junction is denoted by m, then the interaction between the helicase and the junction can be characterized by an interaction potential, $U(m-n)$, which depends only on the separation of the helicase and the junction along the DNA. If the helicase moves toward increasing n, we expect $n \leq m$ because the helicase cannot move on the dsDNA. In the case of passive opening, the interaction potential is described by a hard-wall potential, $U = 0$ for $m > n$ and $U = \infty$ for $m \leq n$, in which the helicase can inhibit DNA closing but does not otherwise affect the dsDNA. The helicase can advance only if the dsDNA opens due to a fluctuation that increases m. During fraying events, the helicase moves forward (n increases) to prevent DNA closing. In the case of active opening, the interaction potential is described by a softer potential with nonzero range,

corresponding to helicase-assisted opening of DNA, e.g., $U = 0$ for $m > n$, $U = U_0 - (m - n)U_0$ for $-N \leq (m - n) \leq 0$, and $U = \infty$ for $(m - n) \leq -N$, for a interaction potential of potential energy that increases by energy U_0 per step for N steps, allowing the helicase to take N steps beyond the point $m = n$ to facilitate opening of the dsDNA. In this example, N characterizes the distance that the helicase interacts with the dsDNA past the junction and U_0 characterizes the amount of energy by which the helicase destabilizes the dsDNA. Choosing an interaction potential to maximize the unwinding rate, an optimized, active DNA helicase can unwind dsDNA as fast as it translocates on ssDNA.

A related approach to characterize active versus passive mechanisms is to use the ratio of the rate of unwinding of dsDNA (V_{un}) to the rate of translocation along ssDNA (V_{trans}) and their dependence on force and DNA sequence [111]. An active helicase displays similar unwinding and translocation rates, giving a ratio of $V_{\text{un}}/V_{\text{trans}} \sim 1$. A passive helicase is slowed by the presence of the dsDNA fork and unwinds dsDNA at a much slower rate, resulting in $V_{\text{un}}/V_{\text{trans}} << 1$. For a passive helicase, the upper bound for the rate of unwinding is given by $V_{\text{un}} \leq \frac{\alpha}{\beta} V_{\text{trans}}$ [109], where α and β denote the opening and closing rates of the DNA. The average value of $\frac{\alpha}{\beta}$ is approximately $\frac{1}{7}$ for DNA [94]. Thus, the unwinding rate of a passive helicase is at most 0.14 of its ssDNA translocation rate.

These methods have been used to analyze the unwinding of several helicases. SF1A helicases, PcrA, Rep, and UvrD, were found to be active helicases. Crystallographic studies of PcrA resolved destabilization of 4-5 bp near the junction [29] and footprinting and binding studies of PcrA with mutation of residues contacting the DNA duplex produced enzymes that were deficient in helicase activity due to reduced affinity to duplex DNA in the absence of a nonhydrolyzable ATP analog, but had translocation activities that were the same as those of the wild-type enzyme [112], together showing that PcrA actively engages and distorts the duplex DNA in an ATP-dependent process. Single-turnover kinetics experiments of Rep with its 2B domain replaced by three glycines (RepΔ2B) showed that RepΔ2B monomers exhibit a translocation rate of 530 ± 10 nt s^{-1} along ssDNA and an unwinding rate of 226 ± 28 bp s^{-1} [at 25 °C in 20 mM Mops (pH 6.5), 20 % (v/v) glycerol, 5 mM

2-mercaptoethanol, 200 mM NaCl, 4.2 mM $MgCl_2$, and 3 mM ATP] [113], resulting in a V_{un}/V_{trans} ratio of 0.43, which is greater than the upper-bound limit for a passive helicase.

Several studies of UvrD obtained translocation rates of UvrD along ssDNA and dsDNA. In a magnetic tweezer single-molecule study, UvrD exhibited an average unwinding rate of 248 ± 3 bp s^{-1} and an average rezipping rate, $\langle V_{zip} \rangle$, of 298 ± 3 bp s^{-1}, where the rezipping events were interpreted as enzyme-translocation-limited closing of the two DNA strands opened during unwinding, as $\langle V_{hyb} \rangle \approx 8 \langle V_{zip} \rangle$, where $\langle V_{hyb} \rangle$ is the average DNA rehybridization rate [at 25 °C in 20 mM Tris·HCl, 25 mM NaCl, 3 mM $MgCl_2$, 0.1 mM EDTA, 1 mM dithiothreitol, and 0.5 mM ATP] at $F = 35$ pN [114], resulting in a V_{un}/V_{trans} ratio of 0.83. In stopped-flow studies, UvrD dimers exhibited an average unwinding rate of 68 ± 9 bp s^{-1} [115] and UvrD monomers exhibited an average translocation rate of 189.0 ± 0.7 nt s^{-1} [116] [at 25 °C in 10 mM Tris·HCl (pH 8.3), 20 mM NaCl, 20 % (v/v) glycerol, 4 mg/ml heparin, and 0.5 mM ATP:Mg^{2+}]. In another magnetic tweezer study, UvrD exhibited an unwinding rate of 27 ± 4 bp s^{-1} at $F = 5$ pN and two translocation rates, a monomeric UvrD translocation rate of 150 nt s^{-1} at $F = 5$ pN, and a dimeric UvrD rewinding rate of 44 ± 3 bp s^{-1} at $F = 5$ pN [at 25 °C in 25 mM Tris·HCl (pH 7.4), 50 mM NaCl, 3 mM $MgCl_2$, 0.2 μg/μl BSA, 1 mM dithiothreitol, and 1 mM ATP] [117], resulting in a V_{un}/V_{trans} ratio of 0.61 for UvrD dimers at $F = 5$.

SF2 helicases were also found to be active, such as the hepatitis C viral NS3 helicase (NS3h) [118, 119] and the RecQ helicase [111]. Optical tweezers experiments of NS3h unwinding of an RNA hairpin with 52% GC-content were performed and measured an average unwinding rate of 51 ± 26 bp s^{-1} at $F = 17$ pN [118]. Interestingly, unwinding of the portion of an RNA hairpin with 100% GC-content was 22 ± 17 bp s^{-1} at $F = 7$ pN, which was >14,000-fold faster than a passive helicase, indicating that NS3h is an active helicase. Presteady-state kinetic studies of NS3h investigated the helicase activity dependence on base-pair stability [at 22 °C in 50 mM MOPS·Na (pH 7.0), 40 mM NaCl, 5 mM $MgCl_2$, 5 mM dithiotheitol, 0.1% Tween 20, 1 μM SSB, 100 nM NS3h, 2.5 nM unwinding substrate, and 5 mM Mg-ATP] [119]. Formulations of a single-step interaction potential derived by Betterton and Julicher [110] were used to model the unwinding rate versus

bp-stability dependences, with interaction energies per base pair of ~1.7 kcal mol^{-1} (2.9 k_BT per helicase) and ~0.9 kcal mol^{-1} (1.5 k_BT per helicase) for unwinding of dsDNA and RNA:DNA hybrid molecules, respectively. Comparison of the modeled and observed dependences show that the observed dependences are not described by the passive model, providing additional evidence that NS3h is an active helicase.

Several ring-shaped helicases were found to be passive, including the bacteriophage T4 helicase gp41 [120] and DnaB helicase [111]. Magnetic-trapping studies of the T4 helicase were performed and an unwinding rate at zero force was extrapolated to be 30 bp s^{-1} [at 25 °C in 25 mM Tris·Ac (pH 7.5), 150 mM KOAc, 10 mM $MgOAc_2$, 1 mM dithiothreitol, and 0.5, 1, 2, 4, or 5 mM ATP] from unwinding rate measurements at forces ranging 2–11 pN [120]. The rezipping rate versus [ATP] was fit retrieving a maximum rate of 400 ± 10 bp s^{-1}. The ratio of V_{un}/V_{trans} was 0.08, which indicates that the T4 helicase is a passive helicase.

The ring-shaped bacteriophage T7 gp4 helicase was measured to be partially active [72, 119]. Optical-trapping studies of the T7 helicase measure an average unwinding rate of 29 bp s^{-1} (σ not stated) with an assisting force of F = 5.2 pN, an average unwinding rate of 220 bp s^{-1} (σ not stated) with an assisting force of F = 11.2 pN, and an average ssDNA translocation rate of 322 ± 62 nt s^{-1} (mean ± σ) [at 25 °C in 20 mM Tris·HCl (pH 7.5), 50 mM NaCl, 7 mM $MgCl_2$, 3 mM EDTA, 0.02% Tween 20, and 2 mM dTTP] [72]. The observed force-velocity dependence is consistent with an active unwinding model [72]. Pre-steady-state kinetic studies of the T7 helicase measured the helicase activity dependence on base-pair stability [at 18 °C in 50 mM Tris·HCl (pH 7.6), 40 mM NaCl, 2 mM $MgCl_2$, 10% glycerol, 2 μM SSB, 100 nM hexamer, 2.5 nM unwinding substrate, and 2 mM dTTP] [119]. Formulations of a single-step interaction potential derived by Betterton and Julicher [110] were used to model the unwinding rate versus bp-stability dependences, with an interaction energy per base pair of ~1.2 kcal mol^{-1}. Comparison of the modeled and observed dependences indicate that the observed dependences are not described by the passive model, providing further evidence that the T7 helicase is an active helicase.

Sub-classes within the active and passive models propose more specific helicase mechanisms,

including the inchworm, rolling, thermal ratchet, and Brownian motor models. The inchworm model was proposed based on studies of Rep and helicase III [121] and has since been applied to PcrA [29, 122] and a refined "wrench-and-inchworm" model has been applied to UvrD [27]. In the inchworm model, a helicase possesses two non-identical nucleic acid binding sites that bind with polarity to the DNA substrate [94, 104, 105]. The leading site interacts with the duplex to be unwound and can bind both the duplex and ssDNA, and the tail site binds only the unwound ssDNA (Figure 3.4 [108]). Translocation along ssDNA with DNA unwinding occurs only through conformational changes coupled to binding and hydrolysis of one or more NTP molecules. In this model, the same leading site always interacts with the duplex DNA during successive unwinding cycles.

The rolling model was proposed based on observed allosteric effects of nucleotide cofactors on the DNA binding properties of the Rep dimer [105, 123]. The binding energetics and relative population distrubutions of different Rep-dimer-DNA complexes were determined in the presence and absence of nucleotide cofactors ADP and nonhydrolyzable ATP analog β-γ-imidoadenosine 5′-triphosphate [AMPP(NH)P]. Rep-dimer-DNA complexes included half-saturated bound states, consisting of one Rep protomer bound to either a ssDNA or a dsDNA and the other Rep protomer not bound to DNA, and fully-saturated bound states, consisting of both Rep protomers bound to ssDNA, both Rep protomers bound to dsDNA, or one Rep protomer bound to ssDNA and the other Rep protomer bound to dsDNA. Large allosteric effects were observed; binding of ADP favored Rep dimers in which both protomers bound ssDNA, whereas binding of AMPP(NH)P favored simultaneous binding of both ssDNA and dsDNA to the Rep dimer. Additional support for a rolling mechanism includes the observation that Rep can bypass regions within the 3′ ssDNA that would otherwise block the helicase if continuous sliding along the DNA were required for DNA unwinding [124], and the observation that binding of ssDNA to one subunit of the Rep dimer stimulates release of DNA from the other subunit, a DNA-exchange reaction that is further stimulated by ATP hydrolysis [125].

The rolling model can apply to any homo-oligomeric helicase and requires at least two identical

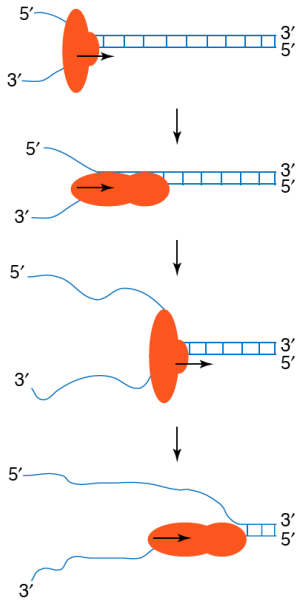

Figure 3.4: The inchworm model. Reprinted from from Soultanas and Wigley (2001) [108], with permission from Elsevier. A monomeric helicase is shown translocating unidirectionally along a DNA molecule, unwinding the duplex in the process.

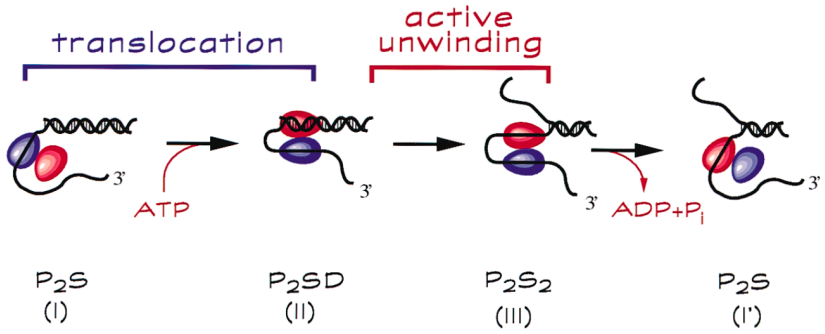

Figure 3.5: The rolling model. Reprinted from Korolev *et al.* (1997) [127], with permission from Elsevier. DNA unwinding and translocation by the dimeric *Escherichia coli* Rep DNA helicase is shown, with the subunits colored in different colors to distinguish between their alternating binding to the duplex as the protein moves forward. The letter (P) indicates the Rep monomer. The letters (S) and (D) indicate ssDNA and dsDNA, respectively [123].

DNA binding sites, both of which must be able to bind ssDNA as well as dsDNA (Figure 3.5). The rolling model assumes that each protomer of the helicase binds ssDNA with a defined polarity. At least one helicase subunit is always bound to the ssDNA at the fork, while the other subunit is bound either to the same single strand or to the adjacent duplex region ahead of the fork. In contrast to the inchworm model, each subunit alternates binding to the ssDNA and dsDNA. The evidence that led to the proposal of the rolling model is also consistent with the "dimeric inchworm model," which is currently favored for dsDNA unwinding by UvrD dimers *in vitro* [21, 126].

In the thermal ratchet (a.k.a. Brownian ratchet) model, the interaction potential is characterized by a hard-wall potential [109, 110]. In this scenario, the interaction potential $U = 0$ for $m > n$ and $U = \infty$ for $m \leq n$, requiring that the helicase does not move on the dsDNA. This model describes a passive helicase mechanism. In general, the interaction between a helicase and a ssDNA-dsDNA junction has nonzero range and corresponds to enzymatically-assisted opening, making the thermal ratchet model unlikely [109]. Crystal structures reveal that several helicases can interact with ≥ 5 bp in the duplex region of the ssDNA-dsDNA junction: PcrA [29], NS3 [128], Rep [127], [129], Dexx box DNA helicase [130], including the interaction between RecBCD with 12 bp in the duplex region past the junction [131]. Furthermore, in the case of the hard-wall potential,

it was shown that the ratio of the maximum average unwinding velocity to the translocation velocity along a junction-less DNA track is limited by the free energy required to open a base pair [109].

In the Brownian motor model, a helicase translocates directionally by undergoing alternating cycles of tight and weak binding to an inherently asymmetric DNA substrate [110, 132, 133, 134]. The SF2 NS3 helicase was found to meet the requirements of this model, in which NS3 binds tightly in the absence of ATP and more weakly in the presence of ATP [132, 135].

3.1.3 The versatility of the RecBCD enzyme

To study helicase mechanism, we studied the RecBCD enzyme, a superfamily-1 helicase with several unique characteristics. It is the most rapid and most processive helicase reported in the literature [23], unwinding DNA with velocities of ~1000 bp s^{-1} [136, 137, 138, 139]. Ensemble assays observe an average of 36,000 bp unwound per binding event [140], while single-molecule assays record processivities as high as 48,000 bp [136]. The RecBCD holoenzyme is substantially faster and more processive than RecB or RecD alone [141] or the isolated helicase subunits of SF1 helicases PcrA, Rep, and UvrD [96, 142]. Additionally, recent experiments demonstrated that during unwinding, RecBCD also has the ability to disrupt various nucleoprotein complexes (e.g., $EcoRI^{E111Q}$, RNAP, and nucleosomes) by pushing them thousands of base pairs or rapidly ejecting them from the DNA [143]. RecBCD recognizes and binds tightly to the ends of dsDNA molecules, with a dissociation constant in the subnanomolar to low-nanomolar range depending on the salt concentration and on whether the DNA ends contain short ssDNA overhangs on either the 3′- or 5′-terminated strands [137, 138, 144, 145]. The macroscopic efficiency of ATP hydrolysis is between 1.3 and 3 molecules of ATP per base pair unwound, depending on reaction conditions [137, 146].

The RecBCD enzyme plays a crucial role in chromosomal DNA replication and maintenance in certain proteobacteria, including *Escherichia coli* cells [23, 147, 148, 149, 150, 151, 152, 153]. This SF1 helicase salvages broken dsDNA replication forks via homologous recombinational DNA repair and degrades unwanted linear DNA in the cell through use of its helicase, nuclease, DNA sequence recognition, and protein recruiting abilities.

Homologous recombination is a relatively error-free process that can repair DNA lesions using an intact homologous donor molecule as a template (Figure 3.6). In recombination-dependent homologous replication, DNA replication is restarted from a detached replication fork, requiring only a single DNA end [102, 154, 149, 155]. The central step is DNA strand exchange, which involves a joining or "synapsis" between homologous DNA molecules. This step is catalyzed by the RecA protein, which forms a filament on ssDNA [156, 157]. This nucleoprotein filament is the active species in the homology search and subsequent invasion of a homologous duplex DNA [158, 159]. Prior to formation of the RecA filament, broken DNA must first be processed into ssDNA.

The RecBCD enzyme initiates the repair of dsDNA breaks by converting a blunt dsDNA end into a duplex DNA molecule possessing a 3′-terminated ssDNA tail [162, 163]. The RecBCD-catalyzed DNA-end-processing reaction is summarized as follows [23] (Figure 3.7). In step one, RecBCD binds tightly to a blunt (or nearly blunt) DNA end of a linear DNA duplex. In step two, RecBCD couples the hydrolysis of ATP to DNA translocation and unwinding. The ssDNA products are cleaved asymmetrically, with the degradation of the 3′-terminated ssDNA tail being much more vigorous than the degradation of the complementary tail. In step three, the enzyme continues to translocate until it pauses at a crossover-hotspot-instigator (Chi) site (χ), a *cis*-acting 8-nt regulatory DNA sequence serving as an initiation point for recombinational dsDNA repair [164, 165]. The Chi sequence is the ssDNA sequence 5′-GCTGGTGG-3′ on the 3′ DNA strand [166, 167] recognized when RecBCD approaches the 3′ side of the sequence as written [168]. The recognition of Chi dramatically alters the biochemical properties of the enzyme. In step four, RecBCD continues to translocate, but the nuclease polarity is switched; the degradation of the 3′ ssDNA tail is attenuated, whereas the hydrolysis of the 5′ ssDNA tail is upregulated. After Chi recognition, RecBCD facilitates the loading of the RecA protein onto the 3′ ssDNA tail. In step five, RecBCD repeatedly deposits RecA protomers, which act as nucleation points for filament growth primarily in the 5′ to 3′ direction. In step six, the RecBCD enzyme dissociates from the DNA. The product of the enzyme is a recombinogenic nucleoprotein complex of the RecA protein bound to the 3′ ssDNA tail with Chi at its terminus. This product is able to invade homologous duplex DNA

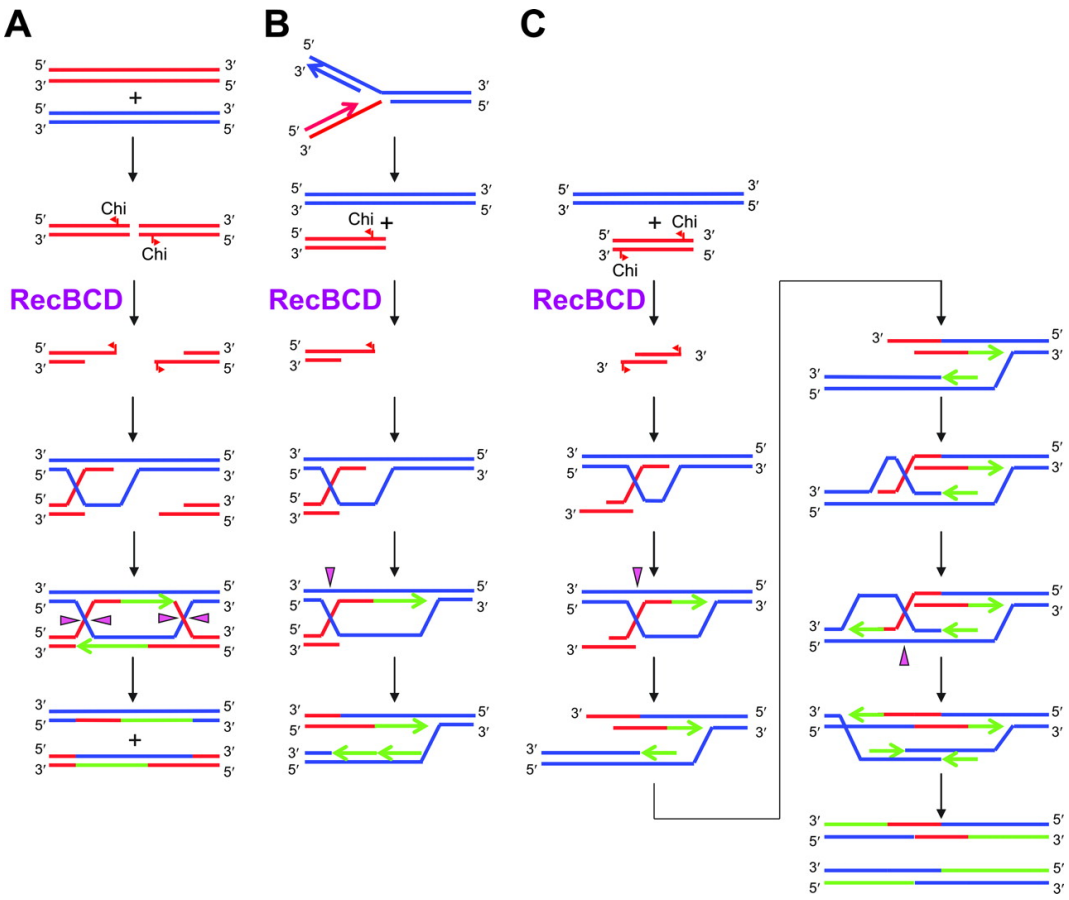

Figure 3.6: RecBCD-dependent homologous recombination pathways. Reproduced from Dillingham and Kowalczykowski (2008) [23] with permission from the American Society for Microbiology. (A) In recombination-dependent DSB repair, a broken DNA molecule containing two (previously contiguous) DNA ends is rejoined in several steps involving recombination with an intact homologous donor DNA ("ends-in" recombination) [160]. (B) In recombination-dependent replication, a single DNA end is formed upon the collapse of a replication fork [161]. (C) Integration of linear dsDNA occurs by an "ends-out" mechanism [160]. Note that in all three panels, for clarity, the location of the Chi sequence is shown only during the initial stages of each pathway.

to promote the recombinational repair of a dsDNA break or to restart DNA replication.

RecBCD is composed of three heterogeneous subunits. Its crystal structure was solved to 3.1 Å in the absence of a nucleotide cofactor [131] (Figure 3.8). In the crystal structure, the DNA substrate is unwound by 4 bp, with each ssDNA tail inserted into a different entry tunnel in the complex. As RecBCD translocates, DNA enters as duplex, is split into two nascent ssDNA strands that are channeled through these tunnels, and are presented to the nuclease domain at the rear. Each of the three subunits contains important structural and biochemical features in the complex. RecB, a DNA-dependent ATPase [169], has an "arm" that stretches to contact the incoming duplex DNA ~12 bp ahead of the junction [131] (Figure 3.9), a motor domain (containing core domains, Section 3.1.1) that undergoes translocation along DNA in the $3' \rightarrow 5'$ direction [170], and a C-terminal domain that has a $3'$ and $5'$ DNA strand endo- and exonuclease role [171, 172, 173, 174] as well as a RecA recruitment role [175, 176]. RecC, a catalytically-dead helicase-nuclease [131, 177] acting as a core scaffolding protein in RecBCD, forms one large hole that contacts domain 2B of RecB, two smaller tunnels that accept the $3'$- and $5'$-terminated ssDNA strands, and protein-protein contacts with RecD, serving as a structural interface between RecB and RecD. RecC contains a dual-methionine "pin" that acts as a wedge to split the duplex at the ssDNA-dsDNA junction [131] (see Figure 3.8) and has exhibited evidence of housing a "Chi-scanning site" [178, 179]. RecD, a ssDNA-dependent ATPase [141, 180], has a motor domain that undergoes translocation along DNA in the $5' \rightarrow 3'$ direction [141]. The two motor domains of opposite directionality make RecBCD a "bipolar" helicase [141, 181].

Previous single-molecule investigations on RecBCD directly measured DNA unwinding and in doing so, observed pausing and slipping on the DNA, events unmeasurable by ensemble methods. RecBCD was observed to pause at Chi sites and change unwinding velocities preceding and following Chi recognition [182, 183, 184]. In addition, RecBCD switched lead motors from RecD to RecB before and after Chi [139]. Higher-resolution studies (~6 bp at 1 Hz) observed force-dependent, Chi-independent pausing and backsliding of the enzyme [30].

One of the outstanding questions regarding the RecBCD helicase is its stepping mechanism.

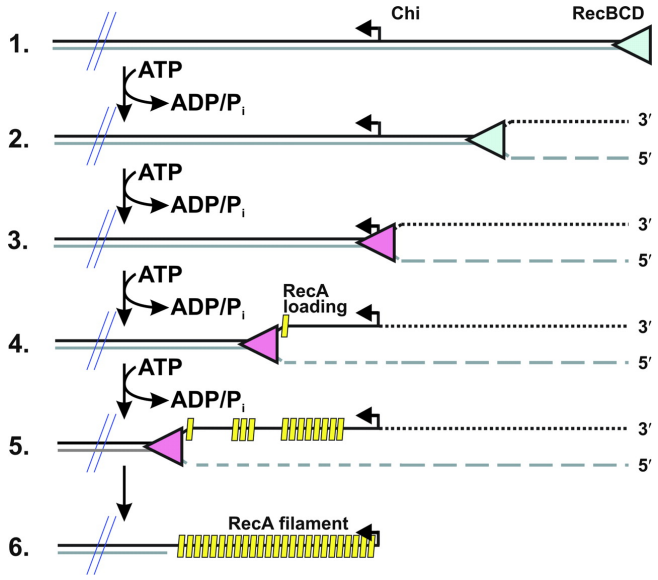

Figure 3.7: The RecBCD-catalyzed DNA-end-processing reaction. Reproduced from Dillingham and Kowalczykowski (2008) [23] with permission from the American Society for Microbiology. (1) RecBCD (*light blue*) binds to the end of a blunt or nearly blunt duplex DNA. (2) RecBCD couples ATP hydrolysis to its helicase activity. The ssDNA products are asymmetrically cleaved. (3) RecBCD translocates until it pauses at and recognizes Chi, during which the enzyme's biochemical properties are altered (*pink*). (4) RecBCD continues to translocate, but with switched nuclease polarity. After Chi, RecBCD facilitates RecA (*yellow*) loading onto the 3′ ssDNA tail. (5) RecBCD deposits RecA protomers, which act as nucleation points for filament growth. (6) The RecBCD enzyme dissociates from the DNA.

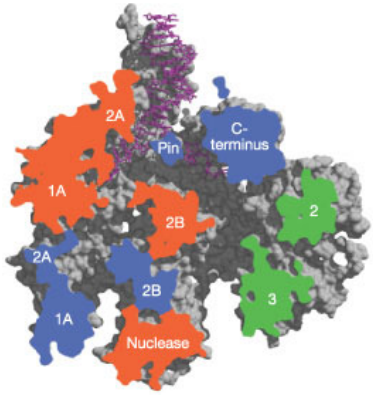

Figure 3.8: Cutaway view showing the channels through the RecBCD·DNA complex. Reprinted from Singleton *et al.* (2004) [131], with permission from Macmillan Publishers Ltd: Nature, Copyright 2004. The cutaway surface of subunits RecB (*orange*), RecC (*blue*), and RecD (*green*) are shown. RecBCD is bound to DNA (*purple*). Numbers refer to the domains of the appropriate subunits. Domains 2 and 3 of RecD are equivalent to canonical helicase domains 1A and 2A.

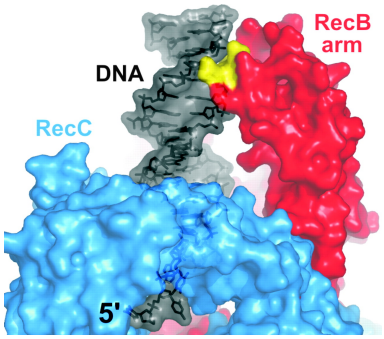

Figure 3.9: The RecB arm. Reproduced from Dillingham and Kowalczykowski (2008) [23] with permission from the American Society for Microbiology. Shown is a close-up view of the "arm" structure (*red*) formed by an auxiliary subdomain (subdomain 1B) of RecB. The arm contacts duplex DNA ahead of the translocating enzyme. A conserved patch of residues in close proximity to the minor groove of the DNA substrate (*black* semitransparent model) is shown (*yellow*). The RecC protein is in the foreground (*blue*). The 5′ ssDNA tail is pointing toward the viewer through a hole in the RecC protein.

Structural and biochemical studies report different step-size values. X-ray crystallographic studies of the SF1B *Deinococcus radiodurans* RecD2 helicase infer a 1-bp step size from structural analysis of RecD2 bound to DNA with and without a nonhydrolyzable nucleotide analog bound [28]. Pre-steady-state single-turnover DNA-unwinding studies measure a "kinetic step size" of 4 ± 1 bp [24, 185], where the kinetic step size is defined as the average number of base pairs unwound between two successive rate-limiting steps in the unwinding cycle [25, 116, 186]. The kinetic step size is the step size calculated from translocation assays that observe the final product or step of the reaction of helicase translocation (e.g., completely unwound ssDNA) of an ensemble of helicases in solution. The kinetic step size is not necessarily the same as the chemical step size, the number of base pairs unwound per ATP molecule hydrolyzed; e.g., if two or more ATP molecules are bound and hydrolyzed in rapid succession, followed by a slower kinetic process, then each kinetic step will be larger than the chemical step. The observed kinetic step size can differ from the mechanical step size in that it can be larger if the enzyme pauses or slips, but it can also be smaller if there are two or more kinetic processes with similar rates that occur during a mechanical step [21, 25, 26]. To address this step-size discrepancy, records of individual RecBCD enzymes unwinding DNA were measured using a precision optical-trapping instrument [187].

The unwinding records of RecBCD displayed large, multi-base-pair conformational dynamics of the RecBCD·DNA complex between steps that we interpret as rapid back-and-forth translocations of RecBCD's dual-methionine pin along the DNA, modulated by the nucleotide state of the enzyme. Here, quantification of the conformational dynamics and interpretations of the dynamics are discussed. Several key observations were made. First, we observed large conformational dynamics in the absence of ATP, indicating that the large conformational dynamics do not originate from enzyme interaction with a nucleotide. Second, the amplitude of the conformational dynamics were dependent on interactions with the end of the 5′ DNA strand, which interacts with the RecD subunit, suggesting that the large conformational dynamics are modulated by enzyme interactions with the 5′ DNA strand. Together with previously measured biochemical data [32], our observations indicate that the onset of large conformational dynamics is coincident with the onset of unwinding

activity by the RecD motor. Third, the conformational dynamics were altered when changing the GC-content of the dsDNA sequence upstream of the ssDNA-dsDNA junction, indicating interaction between the helicase and dsDNA region. Fourth, the dynamics were suppressed in the presence of an engineered, interstrand cross link in the DNA, consistent with translocations of the enzyme pin back and forth along the DNA. Fifth, the dynamics were reduced by the nonhydrolyzable ATP analog, adenosine diphosphate complexed with beryllium fluoride (ADP·BeF_x), suggesting that the ATP-bound state of the enzyme induces a tightly-bound state of the complex. These observations signify the first quantification of previously-unseen, real-time measurements of active destabilization dynamics of the RecBCD·DNA complex and lend insight into the helicase unwinding mechanism of SF1 helicases.

3.2 Directional Motion of RecBCD Along DNA Reveals Large Fluctuations

Experiments to measure directional motion of RecBCD were carried out by tethering a dsDNA molecule between a RecBCD molecule bound to a glass surface and polystyrene bead (Figure 2.24) held with an actively-stabilized optical-trapping microscope [187]. Data were taken at 6 pN of force, unless otherwise noted. With this RecBCD optical-trapping assay, we measured DNA contour length (L) as RecBCD unwound the double-stranded (ds) DNA (Figure 3.10) [90, 187]. Unwinding of the dsDNA caused a decrease in L. RecBCD motion ($N = 17$) displayed pauses and changes in velocity [90, 187] (Figure 3.10) as had been observed in previous experiments [30]. Records displayed discrete forward and backward steps, which appeared as directional translocations of the enzyme separated by pauses in movement (Figure 3.10). To quantify the steps, sections of the 1-Hz smoothed data were fit with an automated step-finding algorithm [188] to determine the average value of L for each plateau and its corresponding dwell time [90].

Unexpectedly, the measurements of RecBCD·DNA motion paused between steps (Figure 3.11) exhibited large-scale fluctuations that were significantly larger than the measured noise floor of the optical-trapping instrument (Section 3.3). The fluctuations were characterized by calculating the power spectral density (PSD) of the DNA contour length time courses and determining the

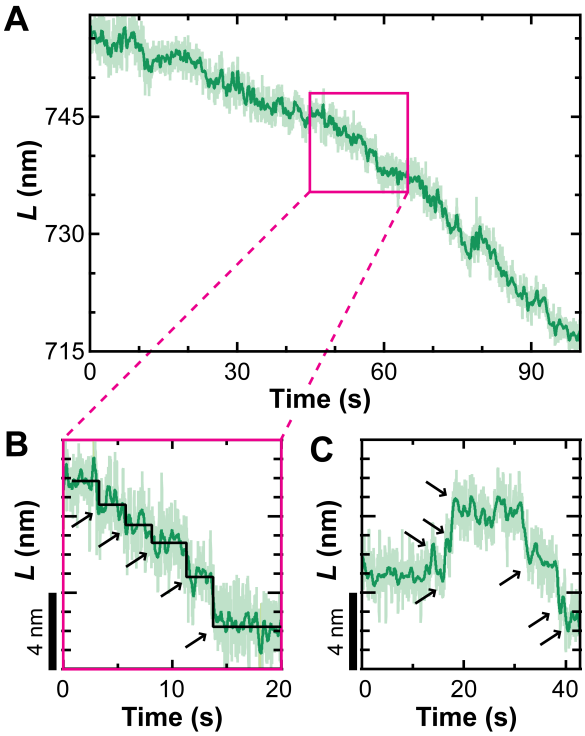

Figure 3.10: Directional motion of RecBCD. Adapted from Carter (2008) [90] and Carter *et al.* (2011). (A) DNA contour length (L) decreases as RecBCD unwinds the DNA substrate. Traces were taken at 6 pN of force, 2 μM ATP, and smoothed with a Savitzky-Golay window to 10 Hz (*light green*) and 1 Hz (*dark green*). (B) Enlarged region (*pink box*) displays forward translocation. (C) Backward translocation was also observed. Data were fit with a step-finding algorithm (*black*; line and arrows) [188].

integrated fluctuations (see Section 2.7), which was calculated from a frequency of 0.07 Hz. The PSD of the records of RecBCD paused between steps (Figure 3.12) indicated that the fluctuations occur over a frequency range of 0.07–10 Hz, which also encompasses the average forward stepping frequency of 0.62 s^{-1} [187]. At 10 Hz, the mean value of the integrated fluctuations was 1.39 ± 0.02 nm (mean ± $\sigma_{\bar{x}}$) [90] for RecBCD paused between unwinding steps.

3.3 The RecBCD·DNA Complex Exhibits Conformational Dynamics

The potential sources of fluctuations in our RecBCD assay can be categorized as follows (Figure 3.13): (I) motion of the biotin-streptavidin surface attachment, (II) motion of the RecBCD biotinylated attachment linker, (III) conformational changes of RecBCD, and (IV) translocations of RecBCD relative to the DNA substrate. To examine the first two potential sources of noise, we measured a series of controls including DNA tethered to the surface in the absence of RecBCD and DNA tethered to the surface bound to RecBCD .

3.3.1 Instrumental noise at the level of 1 bp

To demonstrate 1-bp stability of the DNA optical-trapping assay, we measured the instrumental noise using two types of DNA tethers in the absence of RecBCD. The first type was comprised of a 1007-nm dsDNA molecule with a 5′-biotin label attached to a streptavidin-coated bead and a 5′-digoxigenin label attached to the antidigoxigenin-coated glass surface. The instrumental noise was quantified with the same analysis methods used to quantify the fluctuations of RecBCD paused between steps (Section 2.7). Because we observed the greatest conformational dynamics of RecBCD·DNA as shown in the PSD in the frequency bandwidth 0.07–10 Hz (Figure 3.12), we quantified instrumental noise in this bandwidth. At 1 Hz, the first type of DNA tether exhibited a mean integrated fluctuations value of 0.285 ± 0.011 nm (0.84 ± 0.03 bp, mean ± $\sigma_{\bar{x}}$) (Figure 3.14), $N = 10$ (see Appendix C). At 10 Hz, the mean value of the integrated fluctuations was 0.502 ± 0.012 nm (1.49 ± 0.03 bp) (Figure 3.14), $N = 10$ (see Appendix C). The mean integrated fluctuations data demonstrate the capability of our optical-trapping instrument to measure 1-bp

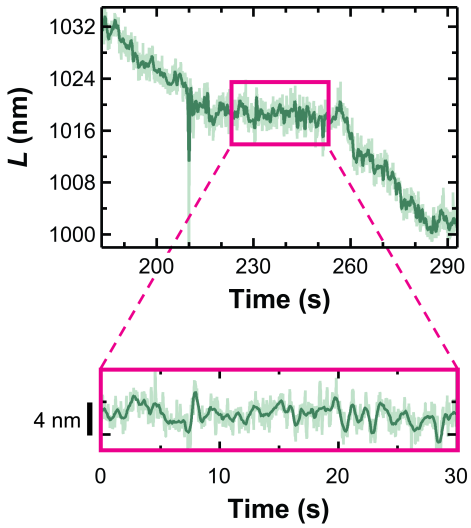

Figure 3.11: RecBCD·DNA displays large fluctuations when paused between stepping. Adapted from Carter (2008) [90]. DNA contour length (L) decreases as RecBCD unwinds the DNA substrate. Traces were taken at 6 pN of force, 2 μM ATP, and smoothed with a Savitzky-Golay window to 10 Hz (*light green*) and 1 Hz (*dark green*). Enlarged area (*pink box*) is an example of RecBCD paused between stepping.

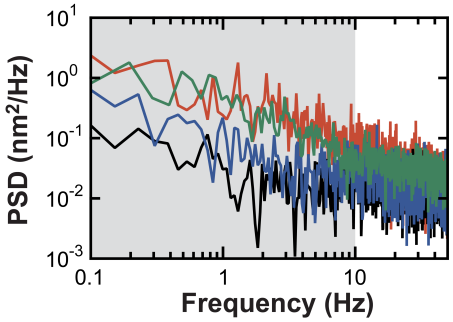

Figure 3.12: Distinct fluctuations over 0.07–10 Hz. Representative power spectral density records of RecBCD paused between stepping (*green*), RecBCD bound to the middle of DNA in the absence of ATP (*red*), RecBCD bound to the end of blunt-ended DNA (*blue*), and DNA directly attached to a surface (*black*). Grayed region indicates the frequency bandwidth over which large conformational dynamics of the RecBCD·DNA complex occur.

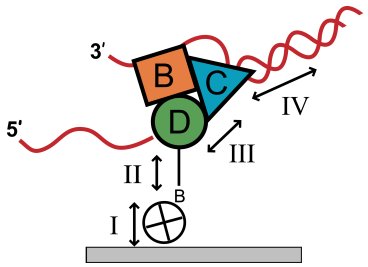

Figure 3.13: Potential sources of fluctuations in the single-molecule RecBCD assay. Adapted from Carter (2008) [90] and Carter *et al.* (2011). Fluctuations in the DNA contour length may be caused by (I) the biotin-streptavidin surface attachment, (II) the RecBCD biotinylated attachment linker, (III) conformational changes of RecBCD, and (IV) translocations of RecBCD relative to the DNA.

(0.338 nm; B-form DNA) changes in DNA contour length (Δf = 0.07–2.3 Hz).

3.3.2 Tailed DNA does not exhibit large fluctuations

In a second study of DNA tethers in the absence of RecBCD, a similar DNA construct was used with the exception that it contained noncomplementary ssDNA tails on the digoxigenin-labeled end ("dT_{10} control," Figure 2.23). The DNA end attached to the streptavidin-coated bead contained a 5′-biotin label. The DNA end attached to the antidigoxigenin-coated glass surface had a 3′-$(dT)_6$ ssDNA tail and a digoxigenin-labeled 5′-$(dT)_{10}$ ssDNA tail. The value of the integrated fluctuations at 10 Hz was 0.57 ± 0.03 nm (1.7 ± 0.1 bp, mean ± $\sigma_{\bar{x}}$) (Figure 3.14), N = 5 (see Appendix C), slightly higher than that of the non-tailed DNA data, which was 0.50 nm. Only a very slight amount of noise of 0.07 nm (0.2 bp) was added with the addition of the ssDNA dT tails. This study demonstrates that the presence of a 10-nt ssDNA region does not greatly alter the fluctuations in our optical-trapping assay.

3.3.3 RecBCD bound to blunt-ended DNA does not exhibit large fluctuations

To examine whether the attachment of RecBCD to the surface via a biotin-linker was creating the multi-base-pair fluctuations, we measured the fluctuations of RecBCD bound to the end of a blunt-ended DNA molecule ("Blunt end," Figure 2.23). At 10 Hz, the mean value of the integrated

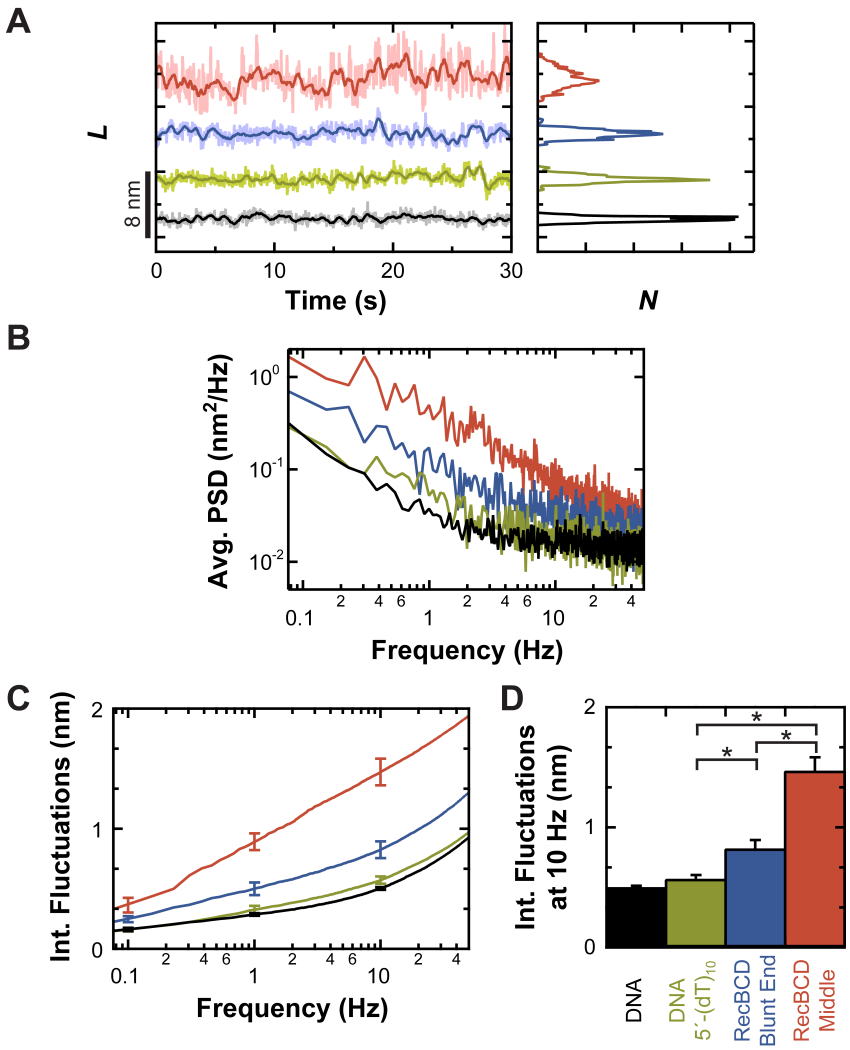

Figure 3.14: The RecBCD·DNA complex exhibits conformational dynamics. (A) Representative data of the DNA contour length versus time with corresponding histograms for tethers of DNA attached to a surface directly (*black*), DNA with 3′-$(dT)_6$ and 5′-$(dT)_{10}$ ssDNA tails attached to a surface (*olive*), RecBCD bound to the end of a blunt-ended DNA molecule (*blue*), and RecBCD bound to the middle of a partially-unwound DNA molecule in the absence of ATP (*red*). Records were taken at $F = 6$ pN and smoothed with a Savitzky-Golay window to 10 Hz (*light*) and 1 Hz (*dark*). (B) Average power spectral density. (C) Average integrated fluctuations of the PSD data. (D) Integrated fluctuations at 10 Hz ($\Delta f = 0.07$–10 Hz, $^*P < 0.02$, $5 \leq N \leq 10$). All error bars denote standard error of the mean.

fluctuations was 0.82 ± 0.07 nm (mean ± $\sigma_{\bar{x}}$) (Figure 3.14), $N = 5$ (see Appendix C) that, although higher than that of the measured instrumental noise, which was 0.50 nm, was well below that of RecBCD paused between steps, which was 1.39 nm. RecBCD bound to blunt-ended DNA was the main control used for quantification of the noise level of the RecBCD optical-trapping assay.

3.3.4 Conformational dynamics are present in the absence of ATP

To test whether the large conformational changes were present in the absence of ATP, we measured RecBCD bound to the middle of DNA in the absence of ATP. RecBCD was allowed to unwind ~1000 nm of a 2413 nm DNA in the presence of ATP and was stalled in the middle of the DNA by flushing WB buffer (~50x flow-cell volume) without ATP through the sample. Measurements of the stalled complex did not exhibit directional motion, but did exhibit conformational dynamics similar to those of RecBCD paused between steps [187]. At 10 Hz, the mean value of the integrated fluctuations of the conformational dynamics was 1.47 ± 0.11 nm (mean ± $\sigma_{\bar{x}}$) (Figure 3.14), $N = 5$ (see Appendix C), which was equivalent within error to that of RecBCD conformational dynamics between steps, which was 1.39 ± 0.02 nm (mean ± $\sigma_{\bar{x}}$) [90]. Similarity of these data was expected due to the unlikelihood of RecBCD interactions with ATP during the pauses between steps at the low concentrations of ATP used (e.g., 2 μM).

3.3.5 Summary

These observations indicate that the fluctuations of RecBCD paused during unwinding are indeed conformational dynamics of the RecBCD·DNA complex. Records of the DNA tethers indicate that the large fluctuations do not originate from instrumental noise. Records of RecBCD bound to blunt-ended DNA eliminate motion of the biotin-streptavidin surface attachment and motion between RecBCD and its biotin tag as the sources of the large fluctuations. Consequently, these control experiments suggest that the large conformational dynamics of the RecBCD·DNA complex are caused by conformational changes of RecBCD and/or translocations of the RecBCD pin relative to the DNA.

3.4 Onset of Dynamics Coincides with Onset of RecD Motor Activity

We next investigated whether the large conformational dynamics of the RecBCD·DNA complex coincided with interaction between the RecD motor and 5′ ssDNA. Equilibrium binding studies [189, 190] and structural work [191] suggest that RecBCD is able to unwind 4–6 bp of a blunt-ended DNA molecule in the absence of ATP in a Mg^{2+}-dependent manner. RecBCD was shown to bind optimally to duplex DNA with 3′-$(dT)_6$ and 5′-$(dT)_m$ tails with $m \geq 10$ nt (at 25 °C in 200 mM NaCl) [190]. Furthermore, RecBCD unwinding studies of DNA possessing 3′-$(dT)_6$ and 5′-$(dT)_m$ tails are described by a sequential n-step mechanism with h additional kinetic steps required prior to initiation of DNA unwinding, where $h = 3.2 \pm 0.1$ for $m = 6$ and $h = 0$ for $m = 10$, indicating that engagement of the RecD motor with the 5′ ssDNA is required for RecBCD to initiate unwinding of blunt-ended DNA [32].

To determine if conformational dynamics of individual RecBCD·DNA complexes are concurrent with the onset of unwinding activity observed in the RecBCD unwinding studies, we probed the effect of RecD-ssDNA engagement on the conformational dynamics in the absence of ATP using 3′-$(dT)_6$ and 5′-$(dT)_m$ DNA constructs, with m = 6, 8, 10, or 20 nt (Figure 3.15). The mean values of the integrated fluctuations at 10 Hz of RecBCD bound to 5′-$(dT)_6$-tailed DNA and 5′-$(dT)_8$-tailed DNA were 0.83 ± 0.05 nm (mean ± $\sigma_{\bar{x}}$), $N = 8$ (see Appendix C) and 0.89 ± 0.09 nm (mean ± $\sigma_{\bar{x}}$), $N = 5$ (see Appendix C), respectively, both of which were equivalent within error to the mean value of the integrated fluctuations at 10 Hz of RecBCD bound to blunt-ended DNA (0.82 ± 0.07 nm). The mean value of the integrated fluctuations at 10 Hz of RecBCD bound to 5′-$(dT)_{10}$ DNA was 1.43 ± 0.09 nm (mean ± $\sigma_{\bar{x}}$), $N = 12$ (see Appendix C), which was equivalent within error to both that of RecBCD bound to 5′-$(dT)_{20}$ DNA, which was 1.39 ± 0.20 nm (mean ± $\sigma_{\bar{x}}$), $N = 5$ (see Appendix C), and to that of RecBCD paused between unwinding steps (1.47 ± 0.11 nm).

The combination of these results has two implications. First, the statistical equivalence of the 5′-$(dT)_6$ and blunt-ended data complements previous studies that indicate that RecBCD undergoes additional kinetic steps prior to unwinding when bound to blunt-ended [24, 26, 185] and twin-$(dT)_6$-

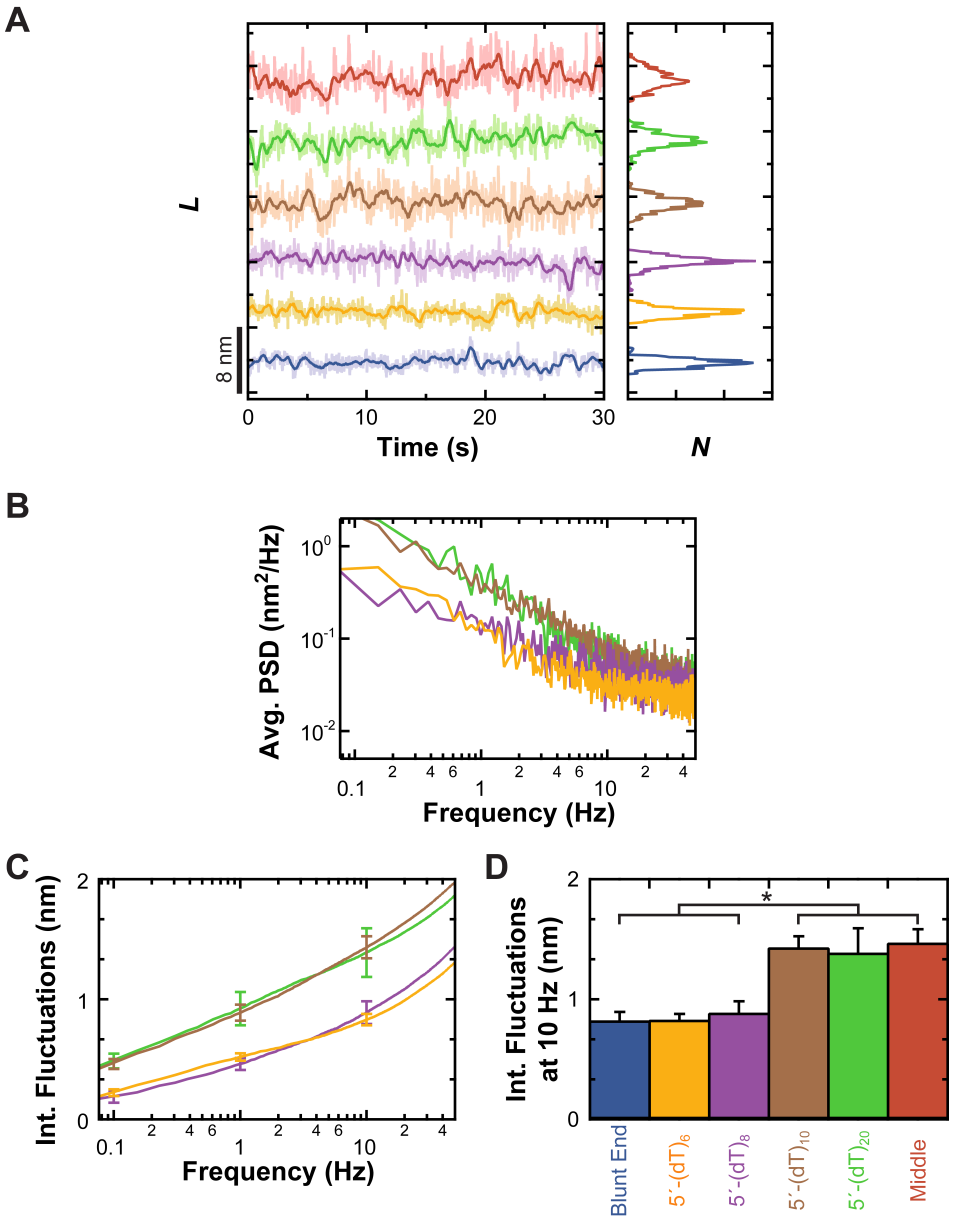

Figure 3.15: Conformational dynamics of RecBCD·DNA depend on length of 5′-(dT) tail. (A) Representative data of the DNA contour length versus time with corresponding histograms for tethers of: RecBCD bound to blunt-ended DNA (*blue*); RecBCD bound to DNA with a 3′-$(dT)_6$ and 5′-$(dT)_n$ ssDNA tails, with $n = 6$ (*yellow*), 8 (*purple*), 10 (*brown*), or 20 (*green*) nt; and RecBCD bound to the middle of a partially-unwound DNA molecule (*red*). Records were taken at $F = 6$ pN and smoothed with a Savitzky-Golay window to 10 Hz (*light*) and 1 Hz (*dark*). (B) Average power spectral density. (C) Average integrated fluctuations. (D) Integrated fluctuations at 10 Hz ($\Delta f = 0.07$–10 Hz, $^*P < 0.05$, $5 \leq N \leq 12$). All error bars denote standard error of the mean.

tailed [32] DNA constructs. Moreover, because RecBCD has been shown to bind optimally to a 3′-$(dT)_6$-tailed DNA end [190] that spans the RecB subunit [191], the lack of large conformational dynamics of RecBCD bound to twin-$(dT)_6$-tailed DNA constructs suggests that the large conformational dynamics of the RecBCD·DNA complex do not originate from interactions between RecB and the 3′-$(dT)_6$ tail.

Second, the statistical equivalence of the 5′-$(dT)_{10}$, 5′-$(dT)_{20}$, and fully-threaded RecBCD data suggest that the minimal requirement for large conformational dynamics of the RecBCD·DNA complex is met with the 5′-$(dT)_{10}$-tailed DNA. Thus, the dependence of the magnitude of the conformational dynamics on the length m of the 5′-$(dT)_m$ tail suggests that large-scale conformational dynamics are required to initiate binding interactions between the RecD motor and the end of the 5′ DNA, which then initiate directional translocation. Since the large conformational dynamics are present when RecBCD is bound to 3′-$(dT)_6$ and 5′-$(dT)_{10}$ tailed DNA, we used these tailed DNA to study RecBCD·DNA in its highly conformationally-dynamic state with a predetermined DNA contour length to simulate RecBCD paused in the middle of DNA after unwinding, which did not have a predetermined DNA contour length.

3.5 Modulation by Nonhydrolyzable ATP analogs

To investigate whether the conformational dynamics of RecBCD bound to 3′-$(dT)_6$ and 5′-$(dT)_{10}$ tailed DNA substrates were altered upon ATP binding, we studied this RecBCD·DNA complex in the presence of various nonhydrolyzable ATP analogs. The conformational dynamics of RecBCD bound to 3′-$(dT)_6$ and 5′-$(dT)_{10}$ tailed DNA substrates displayed various changes in conformational dynamics as dependent on the nonhydrolyzable ATP analog present (Figure 3.16).

The conformational dynamics were significantly reduced in the presence of three nonhydolyzable ATP analogs: adenosine diphosphate complexed with beryllium fluoride (ADP·BeF_x), adenylyl imidodiphosphate (AMPPNP), and adenosine diphosphate with inorganic phosphate (ADP + P_i). The most dramatic reduction was observed when RecBCD·DNA was in the presence of ADP·BeF_x (Figures 3.16 and 3.17), which has been shown to act as an ATP analog in structural and kinetic

studies of myosin [192, 193, 194]. Conformational dynamics of the RecBCD·DNA complex in the presence of 2 mM ADP·BeF_x, 2 mM AMPPNP, and 2 mM ADP + P_i were reduced to mean values of the integrated fluctuations at 10 Hz of 0.91 ± 0.05 nm (mean ± $\sigma_{\bar{x}}$), $N = 9$ (see Appendix C), 1.07 ± 0.09 nm (mean ± $\sigma_{\bar{x}}$), $N = 5$ (see Appendix C), and 1.03 ± 0.14 nm (mean ± $\sigma_{\bar{x}}$), $N = 5$ (see Appendix C), respectively. The ADP·BeF_x data are equivalent within error to those of RecBCD bound to blunt-ended DNA (0.82 ± 0.07 nm) suggesting, when ADP·BeF_x is bound to the RecBCD·DNA complex, that RecD interactions with the 5′-DNA tail are restricted and that RecBCD·DNA may only be able to access the conformational states that are available when RecBCD is bound to blunt-ended DNA. The conformational dynamics in the presence of ADP·BeF_x, AMPPNP, and ADP + P_i were statistically significant from the data of RecBCD·DNA in the absence of ATP analogs, with P-values (see Section 2.7) of $P < 0.0002$, $P < 0.02$, and $P < 0.05$, respectively. These significant decreases in the conformational dynamics suggest that when a nucleotide is bound to one or both of the ATP-binding clefts of RecBCD, the enzyme adopts a conformation in which the contacts between the enzyme and DNA are less dynamic, thus implying a tighter interaction between the enzyme and DNA. The change in the conformational dynamics of RecBCD bound to 5′-$(dT)_{10}$-tailed DNA suggests that binding of ADP·BeF_x, AMPPNP, and ADP + P_i to RecBCD modulates the selection of one or more particular conformational states of the RecBCD·DNA complex.

Conformational dynamics of RecBCD bound to 3′-$(dT)_6$ and 5′-$(dT)_{10}$ tailed DNA were not significantly altered in the presence of two other ATP analogs (Figure 3.16), ADP and adenosine 5′-O-(3-thiotriphosphate) (ATPγS). RecBCD·DNA conformational dynamics were unchanged within error in the presence of 2 mM ADP and displayed a mean value of the integrated fluctuations at 10 Hz of 1.26 ± 0.10 nm (mean ± $\sigma_{\bar{x}}$), $N = 5$ (see Appendix C). When RecBCD was bound to 3′-$(dT)_5$ and 5′-$(dT)_{10}$ tailed DNA in the presence of 2 mM ATPγS, the integrated fluctuations at 10 Hz were also unchanged within error and had a mean value of 1.29 ± 0.15 nm (mean ± $\sigma_{\bar{x}}$), $N = 7$ (see Appendix C). The

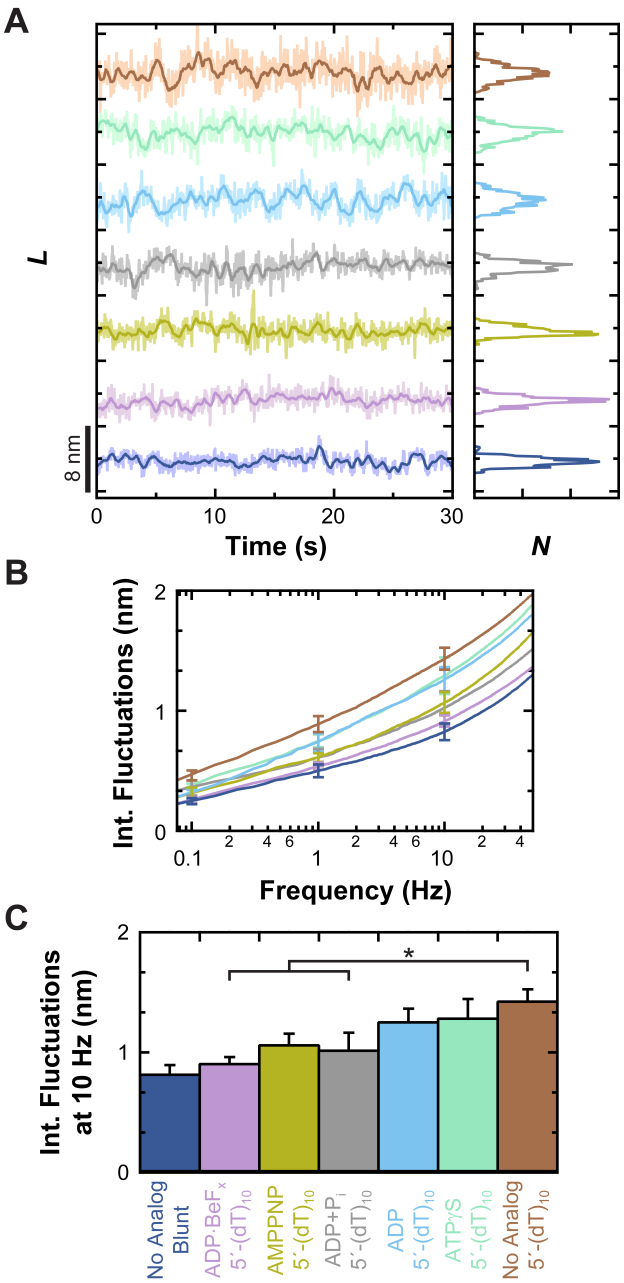

Figure 3.16: RecBCD bound to 5′-$(dT)_{10}$-tailed DNA in the presence of nonhydrolyzable ATP analogs. (A) Representative data of the DNA contour length versus time with corresponding histograms for tethers of RecBCD bound to blunt-ended DNA (*blue*) and RecBCD bound to DNA with 3′-$(dT)_6$ and 5′-$(dT)_{10}$ ssDNA tails in the absence (*brown*) and presence of the following nucleotides and analogs: ADP·BeF_x (*light purple*), AMPPNP (*yellow*), ADP + P_i (*grey*), ADP (*sky blue*), and ATPγS (*sea green*). Records were taken at $F = 6$ pN and smoothed with a Savitzky-Golay window to 10 Hz (*light*) and 1 Hz (*dark*). (B) Average integrated fluctuations. (C) Integrated fluctuations at 10 Hz ($\Delta f = 0.07$–10 Hz, $^*P < 0.05$, $5 \leq N \leq 12$). All error bars denote standard error of the mean.

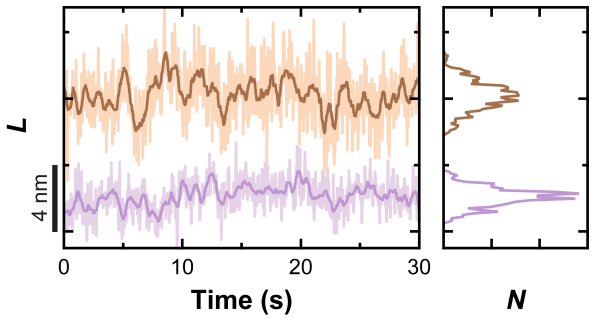

Figure 3.17: Comparison of RecBCD·DNA fluctuations in the presence and absence of ADP·BeF_x. Representative data of the DNA contour length versus time with corresponding histograms for tethers of RecBCD bound to DNA with 3′-$(dT)_6$ and 5′-$(dT)_{10}$ ssDNA tails in the absence (*brown*) and presence of ADP·BeF_x (*light purple*). Records were taken at $F = 6$ pN and smoothed with a Savitzky-Golay window to 10 Hz (*light*) and 1 Hz (*dark*).

3.6 RecBCD Pin Undergoes Back-and-Forth Translocation Along DNA

Conformational dynamics of the RecBCD·DNA complex in the absence of nucleotides may be described by three different scenarios to cause back-and-forth changes in the observed DNA contour length, L (Figure 3.18). In Scenario 1, the enzyme pin does not translocate relative to the ssDNA-dsDNA junction, denoted by the first base pair at the junction that remains base paired when L changes in length by an amount ΔL. Thus, changes in the DNA contour length originate from conformational changes of the enzyme and $\Delta x_{\text{pin}} = 0$, where Δx_{pin} denotes the change in position of the RecBCD pin. In Scenario 2, translocation of the RecBCD pin relative to the DNA substrate is of equal magnitude to that of the observed changes in the DNA contour length, i.e., $\Delta x_{\text{pin}} = \Delta L$. The enzyme pin translocates by an amount ΔL, destabilizing the equivalent number of base pairs. In Scenario 3, a combination of conformational changes of the enzyme and translocation of the enzyme pin relative to the DNA occur such the change in the pin position is nonzero and less than the observed changes of the DNA contour length, i.e., $0 < \Delta x_{\text{pin}} < \Delta L$. The pin destabilizes a portion of the duplex region past the initial junction position, but by a magnitude less than ΔL. In all three scenarios, when a nucleotide is not bound to the RecBCD, the enzyme undergoes conformational changes to maintain at least one constant enzyme-DNA interaction that prevents the enzyme from diffusing backwards along its DNA substrate, a necessary requirement for unidirectional translocation of a helicase.

To investigate the various mechanisms for the large RecBCD·DNA conformational dynamics observed, we made two types of modifications to the duplex region upstream of the ssDNA-dsDNA junction. If the enzyme pin does not undergo translocations relative to the DNA, i.e., if Scenario 1 is true, then the conformational dynamics of the RecBCD·DNA complex should not be affected by changes made in the duplex DNA region. We modified the sequence of the duplex region (Section 3.6.1) and incorporated an interstrand DNA cross link in the duplex region (Section 3.6.3).

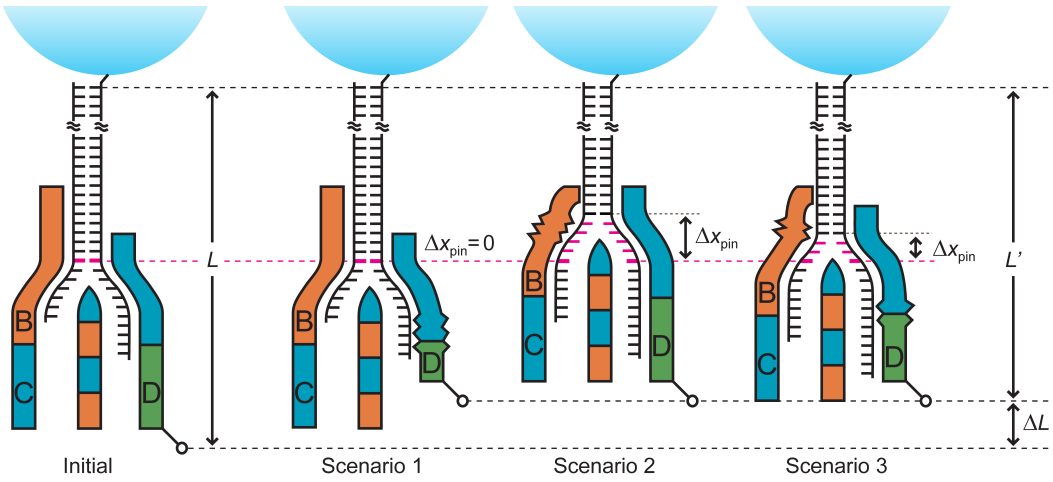

Figure 3.18: Potential mechanisms for back-and-forth motion: Three scenarios of RecBCD·DNA conformational dynamics. The DNA contour length, L, changes in length by an amount ΔL. The initial position of the ssDNA-dsDNA junction is indicated by the first base pair (*pink*). As the junction position changes by an amount Δx_{pin}, the newly destabilized base pairs are indicated (*pink*). Scenario 1: Conformational changes of the enzyme such that $\Delta x_{\mathrm{pin}} = 0$. Scenario 2: Translocation of the RecBCD pin relative to the DNA substrate such that $\Delta x_{\mathrm{pin}} = \Delta L$. Scenario 3: A combination of conformational changes of the enzyme and translocation of the enzyme pin such that $0 < \Delta x_{\mathrm{pin}} < \Delta L$.

3.6.1 Conformational dynamics are dependent on the DNA duplex sequence

We used a set of 5′-$(dT)_{10}$-tailed DNA substrates with differing GC content within the first 11 bp upstream of the fork, one with 9% GC content (AT-rich) and one with 91% GC content (GC-rich) (Figure 2.23). The RecBCD·DNA conformational dynamics were markedly different for RecBCD bound to the AT-rich substrate versus the GC-rich substrate (Figure 3.19), as well as from RecBCD bound to a mixed-seqence substrate (Figure 3.20). RecBCD bound to the AT-rich construct exhibited conformational dynamics with a mean integrated fluctuations value at 10 Hz of 1.74 ± 0.10 nm (mean ± $\sigma_{\bar{x}}$), $N = 14$ (see Appendix C), that was significantly larger ($P < 0.04$) than that of RecBCD bound to a mixed-sequence construct, which had a mean integrated fluctuations value at 10 Hz of 1.43 ± 0.09 nm (mean ± $\sigma_{\bar{x}}$), $N = 12$ (see Figure 3.15 and Appendix C). RecBCD bound to the GC-rich construct exhibited conformational dynamics with a mean integrated fluctuations value at 10 Hz of 1.16 ± 0.07 nm, $N = 11$ (see Appendix C), that was significantly smaller than that of RecBCD bound to the mixed-sequence construct ($P < 0.04$). Both AT-rich and GC-rich DNA substrates contained a single-stranded 5′-$(dT)_{10}$ tail that could engage the RecD subunit, yet complexes of RecBCD bound to the AT-rich construct exhibited significantly larger conformational dynamics than complexes of RecBCD bound to the GC-rich construct. In addition, the conformational dynamics in each case were force-dependent with reduced conformational dynamics observed with increasing force (see Section 3.6.2).

The sequence-dependence results suggest that the enzyme pin is undergoing translocations relative to the DNA junction in the absence of ATP, supporting Scenarios 2 and 3 (Figure 3.18). If RecBCD·DNA interactions were remaining static and the conformational dynamics were solely caused by enzyme conformational changes, then the dynamics would not depend on the sequence of the duplex region of the DNA. The sequence-dependent observations suggest that the RecBCD pin, which has been shown to interact with the ssDNA-dsDNA junction [131], undergoes back-and-forth translocations along the DNA substrate in the absence of ATP and that the amplitude of the translocations is determined by the GC-content of the DNA duplex region.

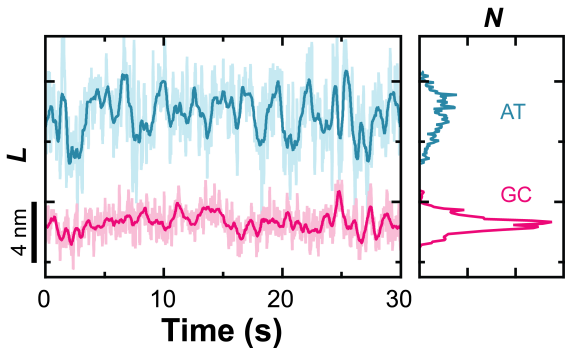

Figure 3.19: Comparison of RecBCD·DNA fluctuations: RecBCD bound to AT-rich versus GC-rich 5′-$(dT)_{10}$-tailed DNA. Representative data of the DNA contour length (L) versus time with corresponding histograms for tethers of RecBCD bound to DNA with 3′-$(dT)_6$ and 5′-$(dT)_{10}$ ssDNA tails with GC-rich (*pink*) and AT-rich (*turquoise*) duplex regions. Records were taken at $F = 6$ pN and smoothed with a Savitzky-Golay window to 10 Hz (*light*) and 1 Hz (*dark*).

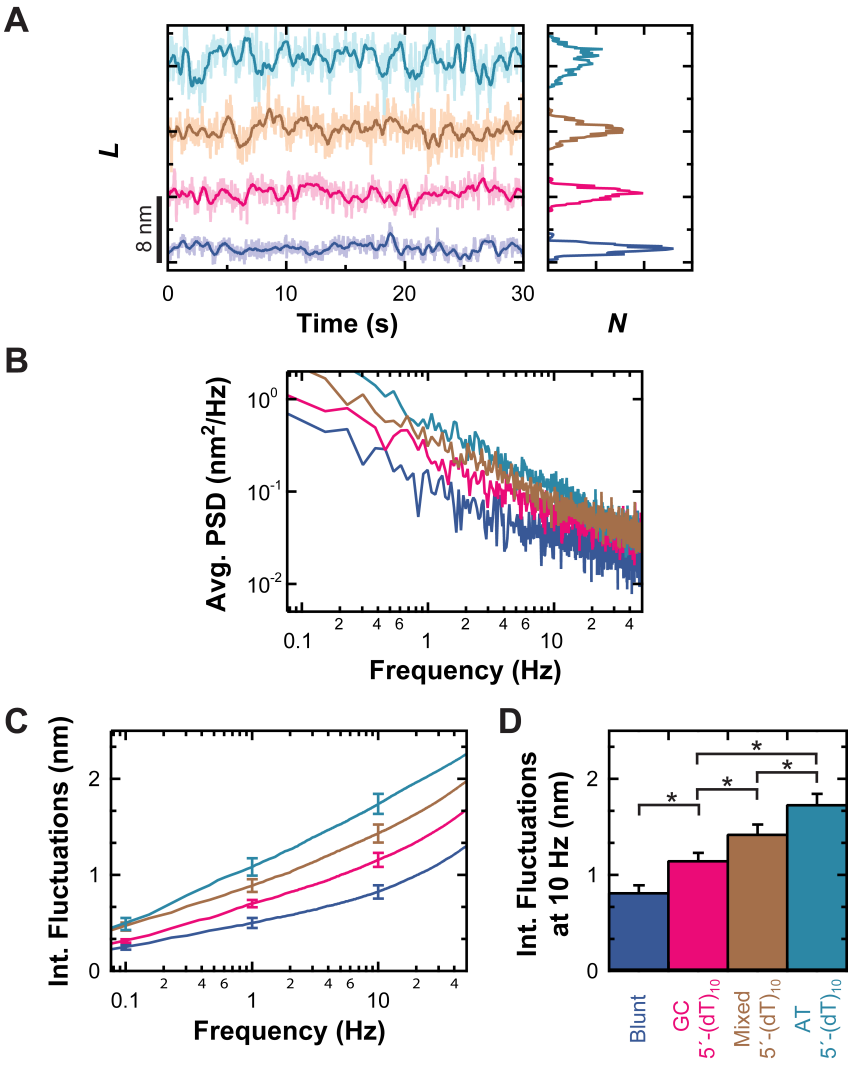

Figure 3.20: Sequence-dependence comparison of RecBCD·DNA bound to 5′-$(dT)_{10}$-tailed DNA. (A) Representative data of the DNA contour length versus time with corresponding histograms for tethers of: RecBCD bound to blunt-ended DNA (*blue*); and RecBCD bound to DNA with a 3′-$(dT)_6$ and 5′-$(dT)_{10}$ ssDNA tails with GC-rich (*pink*), mixed-sequence (*brown*), and AT-rich (*turquoise*) duplex regions. Records were taken at $F = 6$ pN and smoothed with a Savitzky-Golay window to 10 Hz (*light*) and 1 Hz (*dark*). (B) Average power spectral density. (C) Average integrated fluctuations. (D) Integrated fluctuations at 10 Hz ($\Delta f = 0.07$–10 Hz, $^*P < 0.04$, $5 \leq N \leq 14$). All error bars denote standard error of the mean.

3.6.2 Sequence-dependent dynamics observed at various forces

Force-dependence studies of RecBCD bound to AT-rich, GC-rich, and mixed-sequence 5′-$(dT)_{10}$-tailed DNA constructs demonstrated the observation of sequence-dependent conformational dynamics for a range of forces, F = 2, 4, 6, and 10 pN. Three particular complexes of RecBCD bound to DNA with 3′-$(dT)_6$ and 5′-$(dT)_{10}$ tails were studied: RecBCD bound to DNA with an AT-rich base-paired region, a mixed-sequence base-paired region, and a GC-rich base-paired region.

At 2 pN, the mean values ($\pm\ \sigma_{\bar{x}}$) of the integrated fluctuations at 10 Hz were 2.46 ± 0.12 nm, $N = 8$ (see Appendix C), 2.66 ± 0.12 nm, $N = 7$ (see Appendix C), and 3.03 ± 0.47 nm, $N = 6$ (see Appendix C) for RecBCD bound to GC-rich, mixed-sequence, and AT-rich DNA, respectively. At 10 Hz, the integrated fluctuations of the GC-rich, mixed-sequence, and AT-rich data were equivalent within error.

At 4 pN, the mean values ($\pm\ \sigma_{\bar{x}}$) of the integrated fluctuations at 10 Hz were 1.35 ± 0.07 nm, $N = 8$ (see Appendix C), 1.61 ± 0.13 nm, $N = 6$ (see Appendix C), and 2.07 ± 0.21 nm, $N = 6$ (see Appendix C) for RecBCD bound to GC-rich, mixed-sequence, and AT-rich DNA, respectively. At 10 Hz, the mean value of the integrated fluctuations of the AT-rich data was slightly higher than that of the mixed-sequence data ($P < 0.10$), and that of the mixed-sequence data were slightly higher than that of the GC-rich data ($P < 0.13$).

At 6 pN, the mean values ($\pm\ \sigma_{\bar{x}}$) of the integrated fluctuations at 10 Hz were 1.16 ± 0.07 nm, $N = 11$ (see Appendix C), 1.43 ± 0.09 nm, $N = 12$ (see Appendix C), and 1.74 ± 0.10 nm, $N = 14$ (see Appendix C) for RecBCD bound to GC-rich, mixed-sequence, and AT-rich DNA, respectively, as discussed in Section 3.6.1. At 10 Hz, the mean value of the integrated fluctuations of the mixed-sequence data were significantly higher than that of the GC-rich data ($P < 0.04$), and that of the AT-rich data was significantly higher than that of the mixed-sequence data ($P < 0.04$).

At 10 pN, the mean values ($\pm\ \sigma_{\bar{x}}$) of the integrated fluctuations at 10 Hz were 0.88 ± 0.04 nm, $N = 8$ (see Appendix C), 0.99 ± 0.10 nm, $N = 5$ (see Appendix C), and 1.12 ± 0.15 nm, $N = 7$ (see Appendix C) for RecBCD bound to GC-rich, mixed-sequence, and AT-rich DNA, respectively.

Table 3.1: RecBCD·DNA conformational dynamics of RecBCD bound to 5′-$(dT)_{10}$-tailed DNA for various duplex sequences.

Force (pN)	DNA sequence	Integrated Fluctuations at 10 Hz mean ± $\sigma_{\bar{x}}$ (nm)	N
2	GC-rich	2.46 ± 0.12	8
	Mixed	2.66 ± 0.12	7
	AT-rich	3.03 ± 0.47	6
4	GC-rich	1.35 ± 0.07	8
	Mixed	1.61 ± 0.13	6
	AT-rich	2.07 ± 0.21	6
6	GC-rich	1.16 ± 0.07	11
	Mixed	1.43 ± 0.09	12
	AT-rich	1.74 ± 0.10	14
10	GC-rich	0.88 ± 0.04	8
	Mixed	0.99 ± 0.10	5
	AT-rich	1.12 ± 0.15	7

At 10 Hz, the mean values of the integrated fluctuations of the AT-rich and mixed-sequence data were equivalent within error, and those of the mixed-sequence and GC-rich data were equivalent within error.

The sequence-dependence data at various forces are summarized in Table 3.6.2, Figure 3.21, and Figure 3.22. As the applied force was increased, the conformational dynamics of the RecBCD·DNA complex decreased. Reduced conformational dynamics of RecBCD bound to 5′-$(dT)_{10}$-tailed DNA were observed with increasing force. For each force, RecBCD·DNA conformational dynamics were largest for the AT-rich DNA, smallest for the GC-rich DNA, and in between the two cases for the mixed-sequence DNA. At low applied force, Brownian motion begins to dominate the integrated fluctuations, which reduces our resolution to measure the sequence dependence of the conformational dynamics of RecBCD·DNA. At higher applied force, the energy required to destabilize the duplex region increases, which reduces the sequence dependence of the conformational dynamics.

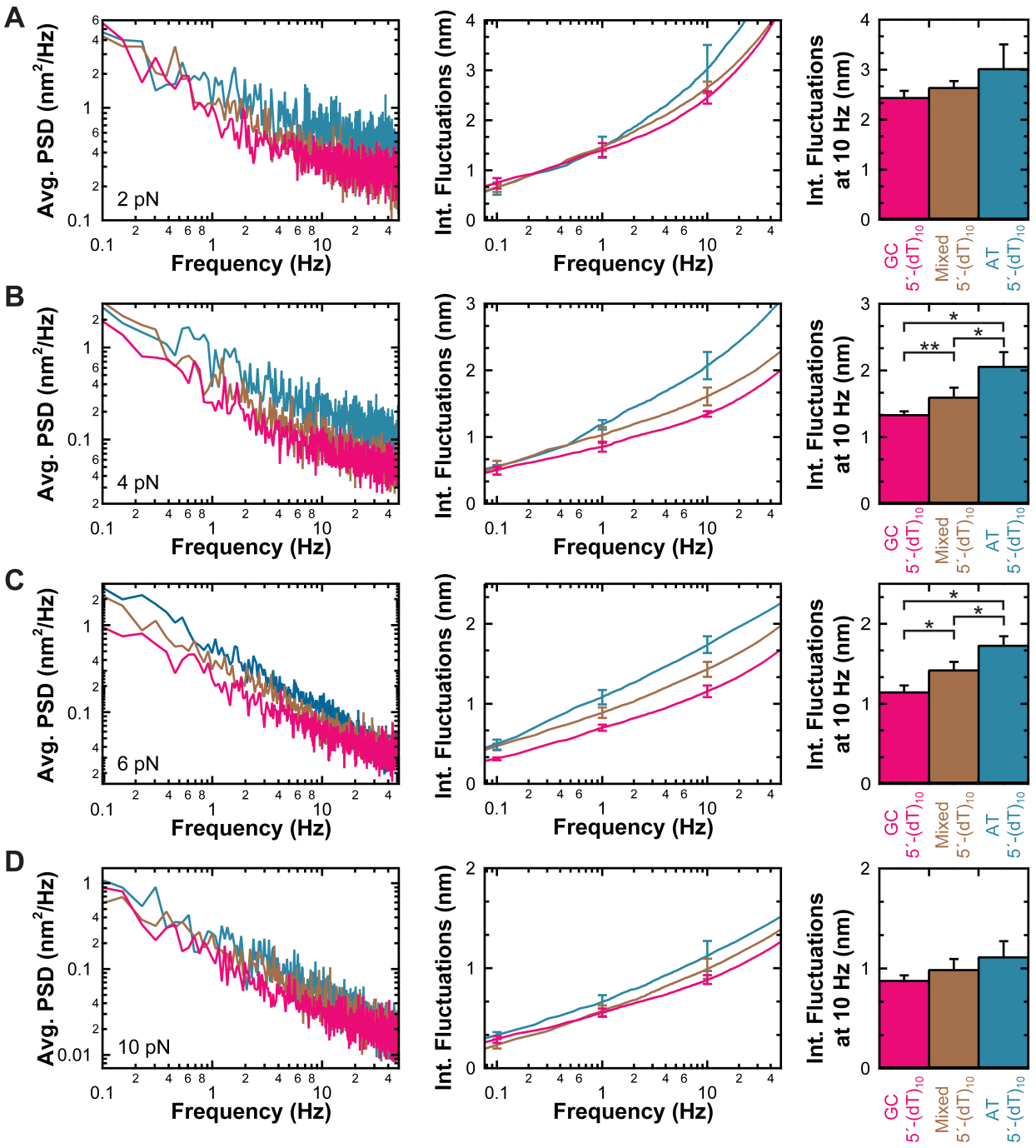

Figure 3.21: Sequence-dependent conformational dynamics of RecBCD bound to 5′-$(dT)_{10}$-tailed DNA at varying force. Average power spectral density, average integrated fluctuations, and average integrated fluctuations at 10 Hz (Δf = 0.07–10 Hz) of RecBCD bound to DNA with a 3′-$(dT)_6$ and 5′-$(dT)_{10}$ ssDNA tails with GC-rich (*pink*), mixed-sequence (*brown*), and AT-rich (*turquoise*) duplex regions. (A) Data taken at F = 2 pN. $6 \leq N \leq 8$ (B) Data taken at F = 4 pN. $^*P < 0.10$, $^{**}P < 0.13$, $6 \leq N \leq 8$ (C) Data taken at F = 6 pN. $^*P < 0.04$, $11 \leq N \leq 14$ (D) Data taken at F = 10 pN. $5 \leq N \leq 8$ All error bars denote standard error of the mean.

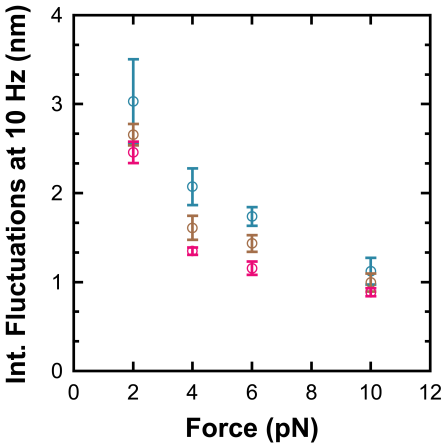

Figure 3.22: Sequence-dependent conformational dynamics of RecBCD bound to 5′-$(dT)_{10}$-tailed DNA versus force. The mean values of the integrated fluctuations at 10 Hz are shown for data taken at $F = 2$, 4, 6, and 10 pN of RecBCD bound to GC-rich 5′-$(dT)_{10}$-tailed DNA (*pink*), mixed-sequence 5′-$(dT)_{10}$-tailed DNA (*brown*), and AT-rich 5′-$(dT)_{10}$-tailed DNA (*turquoise*). All error bars denote standard error of the mean.

3.6.3 Conformational dynamics were suppressed with an interstrand cross link

To determine whether the RecBCD pin undergoes back-and-forth translocations along DNA, we measured RecBCD bound to a 3′-$(dT)_6$ and 5′-$(dT)_{10}$ tailed DNA construct with an engineered, covalent interstrand cross link positioned 3 bp upstream of the junction in the duplex region ("AT cross link, 5′-dT_{10}" and "GC cross link, 5′-dT_{10}," Figure 2.23) and compared the DNA contour length time courses with those of RecBCD bound to a non-cross-linked (dT)-tailed DNA substrate. The N^3T–butyl–N^3T cross link used bridges a mismatched thymidine base pair while maintaining the global structure of a non-cross-linked DNA duplex, indicated by circular dichroism measurements [195] and molecular dynamics calculations restrained by nuclear Overhauser effect and dihedral angle data obtained from NMR spectroscopy [196]. We performed unwinding assays to test the incorporation of the cross link and no unwinding events were observed (data not shown).

In measuring the conformational dynamics of RecBCD complexed with cross-linked DNA, we observed significantly supressed dynamics (Figure 3.23). The mean integrated fluctuations at 10 Hz of RecBCD bound to the ends of the cross-linked construct with two AT base pairs prior to the cross link were 0.96 ± 0.02 nm ($N = 7$; see Appendix C), 0.47 nm less than that of RecBCD bound to the ends of a non-cross-linked DNA construct of mixed sequence and 0.12 nm more than RecBCD bound to blunt-ended DNA. The mean value of the integrated fluctuations at 10 Hz of RecBCD bound to the ends of the cross-linked construct with two GC base pairs prior to the cross link was 1.02 ± 0.05 nm ($N = 5$; see Appendix C). The suppressed conformational dynamics indicate that, in the absence of the cross link, the enzyme pin interacts with the duplex region beyond the first 3 bp of the duplex. This evidence for nonzero back-and-forth translocations support Scenarios 2 and 3.

3.7 Quantifying RecBCD Destabilization of Duplex DNA

Scenario 2 ($\Delta x_{\text{pin}} = \Delta L$) can be tested with two methods that vary the duplex region of the DNA to determine at what base pair position the large-scale conformational dynamics of the

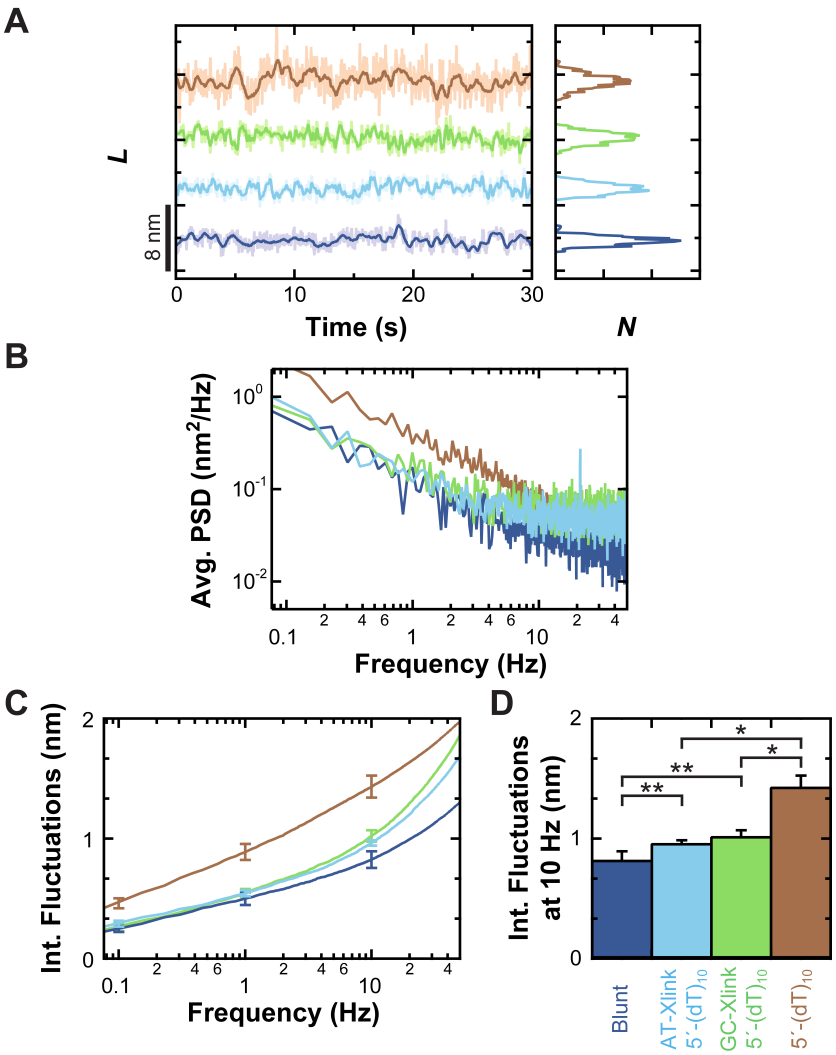

Figure 3.23: Conformational dynamics are altered with a cross-linked DNA. (A) Representative data of the DNA contour length versus time with corresponding histograms for tethers of: RecBCD bound to blunt-ended DNA (*blue*); RecBCD bound to DNA with 3′-$(dT)_6$ and 5′-$(dT)_{10}$ ssDNA tails with an engineered, interstrand cross link 3 bp upstream of the junction, with the first two base pairs comprising of either AT (*light blue*) of GC (*light green*) base pairs; and RecBCD bound to DNA with a 3′-$(dT)_6$ and 5′-$(dT)_{10}$ ssDNA tails with no cross link (*brown*). Records were taken at F = 6 pN and smoothed with a Savitzky-Golay window to 10 Hz (*light*) and 1 Hz (*dark*). (B) Average integrated fluctuations. (D) Integrated fluctuations at 10 Hz (Δf = 0.07–10 Hz, $^{*}P < 0.002$, $^{**}P < 0.12$, $5 \leq N \leq 12$). All error bars denote standard error of the mean.

RecBCD·DNA complex become independent of changes in the duplex region.

In one method, the conformational dynamics of RecBCD bound to 5′-$(dT)_{10}$, 3′-$(dT)_6$ tailed constructs with variations in the sequence of the duplex region are measured. We varied the sequence of the duplex region immediately upstream of the ssDNA-dsDNA junction with the following sequences (Figure 2.23): 5-bp GC base pairs ("GC-rich"), 3-bp GC base pairs ("Low GC-rich"), 5-bp AT base pairs ("AT-rich"), and 4-bp AT base pairs ("Low AT-rich"). Because we observe that conformational dynamics of the complex depend on the sequence of the duplex region (Section 3.6.1), we expect that if the RecBCD·DNA conformational dynamics by the mechanism described in Scenario 2, then the enzyme pin would undergo translocations relative to the DNA with an amplitude equal to that of the changes in the DNA contour length. The mean values of the integrated fluctuations at 10 Hz for RecBCD bound to the ends of AT-rich and Low AT-rich DNA were 1.74 ± 0.10 nm (mean ± $\sigma_{\bar{x}}$), $N = 14$, and 1.71 ± 0.19 nm (mean ± $\sigma_{\bar{x}}$), $N = 5$, respectively, which were equivalent within error. The values of the integrated fluctuations at 10 Hz for RecBCD bound to the ends of GC-rich and Low GC-rich DNA were 1.16 ± 0.07 nm (mean ± $\sigma_{\bar{x}}$), $N = 11$, and 1.04 ± 0.07 nm (mean ± $\sigma_{\bar{x}}$), $N = 5$, respectively, which also were equivalent within error. These results suggest that the enzyme pin does not translocate past the third (fourth) bp when bound to GC-rich (AT-rich) DNA constructs. Because the peak-to-peak values of the conformational dynamics of the complex were much larger than 3–4 bp, this suggests that the RecBCD enzyme undergoes conformational changes, which contribute to the net conformational dynamics observed of the RecBCD·DNA complex and provides evidence against Scenario 2. Together with the observations of altered conformational dynamics in the presence of an interstrand cross link (Section 3.6.3), these results provide support for Scenario 3 ($0 < \Delta x_{\mathrm{pin}} < \Delta L$) as a mechanism for large conformational dynamics of the RecBCD·DNA complex.

In a second method, an interstrand cross link can be introduced to examine two critical positions: the position at which the conformational dynamics of the RecBCD·DNA complex begin to be independent of cross-link position and the position at which the cross link inhibits pin translocation to zero ($\Delta x_{\mathrm{pin}} = 0$). If the enzyme pin does not translocate beyond the third or forth base pair,

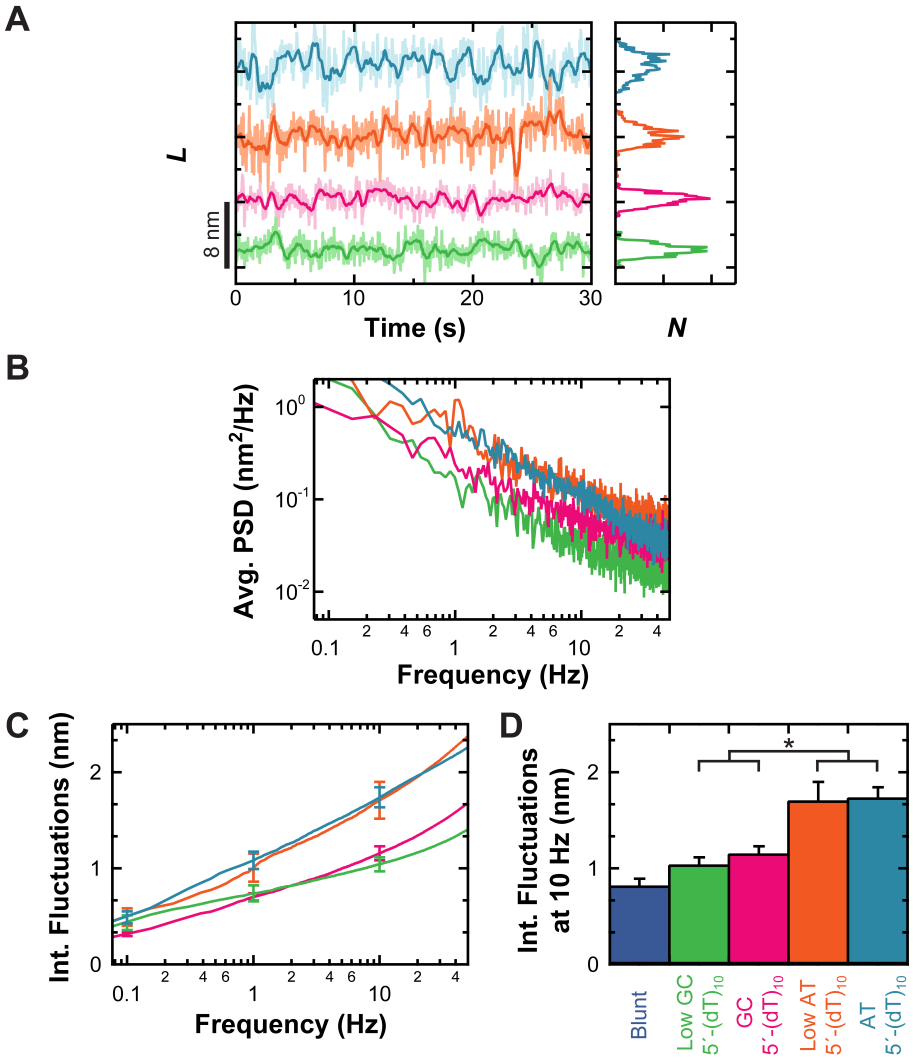

Figure 3.24: (A) Representative data of the DNA contour length versus time with corresponding histograms for tethers of: RecBCD bound to Low GC-rich DNA (*green*), GC-rich DNA (*pink*), Low AT-rich DNA (*orange*), and AT-rich DNA (*blue*) Records were taken at $F = 6$ pN and smoothed with a Savitzky-Golay window to 10 Hz (*light*) and 1 Hz (*dark*). (B) Average power spectral density. (C) Average integrated fluctuations. (D) Integrated fluctuations at 10 Hz ($\Delta f = 0.07$–10 Hz, $^*P < 0.05$, $5 \leq N \leq 14$). All error bars denote standard error of the mean.

as suggested in the AT-rich (GC-rich) vs Low AT-rich (Low GC-rich) sequence-dependent studies, then the conformational dynamics of the RecBCD·DNA complex would be equivalent in the presence and absence of an interstrand cross link positioned at the fifth base pair. If instead the back-and-forth pin translocation were completely inhibited by positioning an interstrand cross link at the first base pair at the junction, then the DNA contour length records could be analyzed to examine the conformational dynamics of the enzyme. These two studies have yet to be performed.

We measured the conformational dynamics of an interstrand cross link at the third base pair from the ssDNA-dsDNA junction (Section 3.6.3). At this position, the RecBCD pin is able to translocate at most by 2 bp ($0 \leq \Delta x_{\text{pin}} \leq 2$ bp, or $0 \leq \Delta x_{\text{pin}} \leq 0.68$ nm). Interestingly, the L time courses of RecBCD bound to the cross-linked DNA exhibit distinct, "spiked" features that contrast with the L time courses of RecBCD bound to blunt-ended DNA (Figure 3.25). The number of 0.87-nm spikes (see Section 2.7) within conformational dynamics records of RecBCD bound to a 5′-$(\text{dT})_{10}$-tailed, AT cross-linked DNA was 45.9 ± 2.8 (mean $\pm\ \sigma_{\bar{x}}$), $N = 7$ (Figure 3.25). This was significantly larger than the number of spikes observed in records of RecBCD bound to blunt-ended DNA ($P < 0.0007$; see Section 2.7), which were 17.0 ± 4.2 (mean $\pm\ \sigma_{\bar{x}}$), $N = 5$. The number of 0.87-nm spikes within conformational dynamics records of RecBCD bound to a 5′-$(\text{dT})_{10}$-tailed, GC cross-linked DNA was 50.0 ± 3.8 (mean $\pm\ \sigma_{\bar{x}}$), $N = 5$, which was also significantly larger than the number of spikes observed in records of RecBCD bound to blunt-ended DNA ($P < 0.0005$) (data not shown). Also, almost no spikes were detected in the records of DNA directly attached to the surface, which were 2.2 ± 0.7 (mean $\pm\ \sigma_{\bar{x}}$), $N = 10$, and were significantly less than the number of spikes observed in RecBCD bound to blunt-ended DNA ($P < 0.03$). The spikes exhibited by RecBCD bound to cross-linked 5′-$(\text{dT})_{10}$-tailed DNA may be due to the interactions of RecBCD encountering the cross link and/or due to conformational dynamics of RecBCD. When RecBCD is bound to the ends of blunt-ended DNA, the RecD motor is not engaged by the 5′ DNA, and RecBCD does not assume a dynamically fluctuating state.

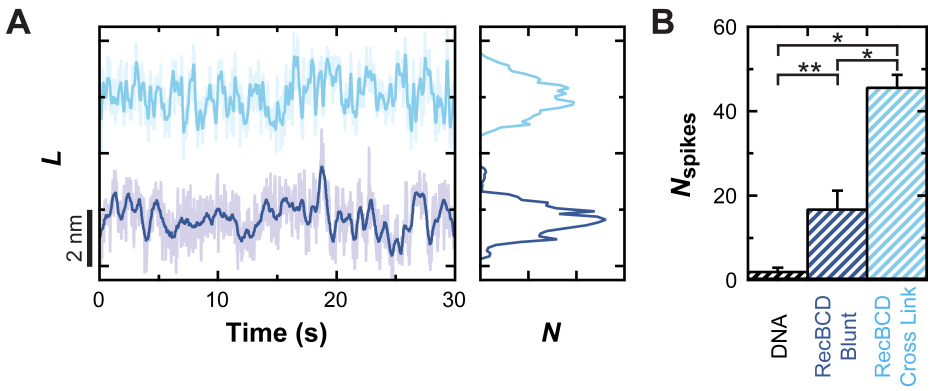

Figure 3.25: Comparison of number of spikes in RecBCD bound to cross-linked versus non-cross-linked DNA. (A) Representative records of the DNA contour length of RecBCD bound to blunt-ended DNA (*blue*) and RecBCD bound to an AT cross-linked DNA with 3′-$(dT)_6$ and 5′-$(dT)_{10}$ ssDNA tails (*light blue*), with corresponding histograms. Data were taken at $F = 6$ pN and smoothed with a Savitzky-Golay window to 10 Hz (*light*) and 1 Hz (*dark*). (B) The average number of 0.87-nm spikes observed in the 1-Hz DNA contour length records of DNA tethered to the surface (*black*), RecBCD bound to blunt-ended DNA (*blue*), and RecBCD bound to an AT cross-linked DNA with 3′-$(dT)_6$ and 5′-$(dT)_{10}$ ssDNA tails (*light blue*). $^*P < 0.0007$, $^{**}P < 0.03$, $5 \leq N \leq 10$. Error bars denote standard error of the mean.

3.8 Discussion

3.8.1 Large conformational dynamics present in the absence of ATP

With a high-precision optical-trapping microscope, we observed multi-base-pair conformational dynamics of RecBCD complexed with a DNA substrate in the absence of ATP. This indicates that the large, multi-base-pair motions are not powered by ATP hydrolysis or binding, but must be strictly due to interactions between the enzyme and the DNA substrate. Specifically, our observations suggest that the conformational dynamics are dependent on interactions between the RecD motor and the 5′-ssDNA end. The conformational dynamics may be driven by RecD translocations relative to the 5′ ssDNA end, or by RecD-DNA interactions that allosterically cause conformational changes elsewhere in the holoenzyme. Interestingly, our records indicate that only a 5′-$(dT)_{10}$ ssDNA tail is required for the 5′ DNA to interact with the RecD motor, which is consistent with equilibrium binding studies that indicate a plateau in the equilibrium binding constant of RecBCD bound to the ends of DNA duplexes with 5′-$(dT)_n$ ssDNA tails for values of $n \geq 10$ [190]. In a crystal structure of RecBCD bound to a single-stranded 5′ tail comprised of seven 5-iodouracil nucleotide analogs and three nucleotides, comprising a 5′ tail of 10 repeats, the 5′ tail appears to only partially engage the motor domains of the RecD motor [191]. Our measurements indicate that this high-resolution snapshot of RecBCD·DNA in a crystal lattice must be only one frame in a dynamic motion picture of both rapidly-fluctuating, back-and-forth translocation of the RecBCD pin along the DNA and conformational dynamics of the enzyme, which contribute to the RecBCD·DNA conformational dynamics that are on the scale of multiple base pairs.

RecBCD does not directionally translocate when paused on an unwound DNA substrate, suggesting that a part of the enzyme maintains constant contact with a part of the DNA substrate, either in the 3′ single-stranded region, the 5′ single-stranded region, the duplex region, or some combination. Crystal structures show that RecBCD extends an “arm” which contacts the duplex region 12 bp beyond the junction [131, 191], which is one potential interaction that may remain constant during the conformational dynamics.

3.8.2 RecBCD operates by dynamic destabilization and conformational changes of the enzyme

Notably, the distinctive alteration of the conformational dynamics when RecBCD is bound to a cross-linked DNA substrate indicates that the RecBCD pin translocates back and forth along the DNA in the absence of ATP. The large conformational dynamics cannot simply be attributed solely to conformational changes of the enzyme with positioning of the enzyme staying relatively constant to that of the DNA substrate. Our observations are consistent with the part of RecBCD that contacts the junction, the RecC pin, undergoing translocation relative to the DNA and thereby contributing to active destabilization of the duplex. Additionally, the large conformational dynamics cannot be attributed to translocations of the enzyme pin of equal magnitude. Our observations are consistent with RecBCD pin translocation relative to the DNA of 3–4 bp, which are smaller than the peak-to-peak behavior of the complex, suggesting that conformational changes of RecBCD contribute to the net conformational dynamics of the RecBCD·DNA complex.

The conformational dynamics are a direct, real-time observation that include dynamic destabilization of the double-stranded region of the DNA substrate by the RecBCD helicase. The direct destabilization of dsDNA by an active helicase to promote DNA opening has been modeled [110]. Correlation of the conformational dynamics with unwinding initiation [32] suggests the conformational dynamics are an integral aspect to the mechanism of the DNA unwinding mechanism of RecBCD. Because RecBCD has the ability to unwind 6 bp in the absence of ATP [189, 190, 191], it is not contradictory that RecBCD is able to dynamically destabilize multiple base pairs at the DNA junction in the absence of ATP. The large conformational dynamics could function to make the cleft between the motor domains more accessible for fast ATP binding and ADP + P_i release, contributing to the high unwinding velocities achieved by this enzyme .

The reduction of the conformational dynamics of RecBCD·DNA in the presence of ADP·BeF_x, AMPPNP, or ADP + P_i suggests that the RecBCD·DNA complex tightens down on the DNA when ATP binds to RecBCD. Presumably, the ATP analog binds to either the RecB or RecD ATP-binding

clefts, causing a conformational change in the RecBCD·DNA complex that reduces the large, multi-base-pair conformational dynamics. Structural studies of a RecD homolog, RecD2 from *Deinococcus radiodurans*, determined 2.5-Å resolution structures of RecD2 complexed with ssDNA in the presence and absence of an ATP analog [28]. Our observation of reduced conformational dynamics in the presence of ADP·BeF_x and other nonhydrolyzable ATP analogs is consistent with this structural result, which indicates that upon ATP-analog binding the number of contacts between RecD2 and the DNA substrate increase and the cleft between the 1A and 2A motor domains closes, tightening the interaction between enzyme and DNA.

Together, our observations suggest a RecD motor mechanism that includes dynamic destabilization, in which conformational dynamics of the RecBCD·DNA complex are modulated by the nucleotide-bound state of the enzyme. When no ATP is bound and RecD is engaged by the 5′ ssDNA end, conformational changes in the RecBCD·DNA complex occur, resulting in conformational changes in the RecBCD and active destabilization of the ssDNA-dsDNA junction, which is consistent with back-and-forth translocation of the dual-methionine RecC pin beyond the average junction position by multiple base pairs. A mechanism that includes dynamic destabilization may aid in RecBCD's fast unwinding speed as well as its ability to displace DNA-bound proteins. It is remarkable that a rearrangement of the three SF1 subunits, RecB, RecC, and RecD, into one holoenzyme can create such a robust and multifunctional enzyme.

Chapter 4

glmS Ribozyme Cleavage

4.1 Active Roles of RNA

4.1.1 Ribozymes are catalytic RNA molecules

Molecular biologists have long suspected that RNA molecules played a key role in the process of how life began on Earth. RNA has an essential role in protein synthesis, a fundamental process within all cells. One of the first observations of RNA catalytic activity in the absence of proteins was of the self-splicing pre-ribosomal RNA of the ciliate *Tetrahymena* [34]. With this work, the word "ribozyme" was coined for the general concept of an RNA molecule with enzymatic activity. The first example of a ribozyme that exhibited multiple turnover was the RNA subunit of ribonuclease P (RNase P), which hydrolyzes the 5′-end of precursor transfer RNA (tRNA) [33]. These findings provided further credibility to the hypothesis of an RNA world [197].

In the RNA world hypothesis, RNA served both as the genetic material and the principal cellular enzyme in cells [198]. This hypothesis postulates that as cellular metabolism became more sophisticated, increasing demands on biocatalysts provided the need for the transition to protein enzymes. Naturally-occurring ribozymes provide further evidence for the hypothesized RNA world [197]. Such ribozymes are present in organisms ranging from bacteria to humans. Examples include RNA that performs self-cleavage via transesterification (e.g., hammerhead, hairpin, hepatitis delta virus, and Varkud satellite ribozymes); self-splicing via transesterification (e.g., Group I intron and Group II intron); pre-tRNA processing via hydrolysis (e.g., RNase P); RNA splicing via

transesterification (e.g., spliceosome); and peptidyl transfer (e.g., ribosome).

In vitro selection experiments demonstrate that it is possible for functional nucleic acids to arise from random sequence libraries [199, 200]. This technique was coined the systematic evolution of ligands by exponential enrichment (SELEX) [201, 202]. Random sequence DNA or RNA pools can be generated by a combination of chemical and enzymatic synthesis, and molecules that perform a particular function can be selected from the pools. For example, the molecules might be selected to exhibit particular catalytic functions, i.e., ribozymes, or to exhibit particular binding properties, i.e., RNA "aptamers," structured nucleic acids capable of specifically binding a target molecule [203]. The selected species are then amplified. After multiple cycles of selection and amplification to mimic natural selection, the RNA molecules generated are typically highly-fit molecules. For example, the theophylline aptamer binds theophylline with a K_{d} of ~400 nM and can discriminate against caffeine, which differs by a single additional methyl group, by a factor of 10,000 [204]. These selected nucleic-acid molecules have been evolved to contain specific binding pockets, perform catalysis, bind cofactors, and adopt complex three-dimensional structures [200].

4.1.2 Riboswitches detect specific metabolites

A riboswitch is a structured RNA element that modulates gene expression in response to the direct binding of a metabolite [205]. Riboswitches, which usually reside in the $5'$ noncoding regions of messenger RNA (mRNA), are *cis*-acting genetic control modules, meaning they act on the mRNA in which they are located. They are generally utilized in the feedback repression of genes involved in the synthesis or import of the cognate metabolite. To control gene expression, riboswitches form highly-specific binding pockets for their target metabolite and typically undergo allosteric changes in structure upon ligand binding (Figure 4.1). This interaction of the aptamer domain with the immediately downstream functional domain, the "expression platform," provides the interface with various other components of the gene-expression apparatus. Ligand binding is achieved solely by the aptamer domain, which usually does not require the presence of the expression platform or the action of protein factors [205]. Over 20 distinct classes of riboswitches have been identified [206].

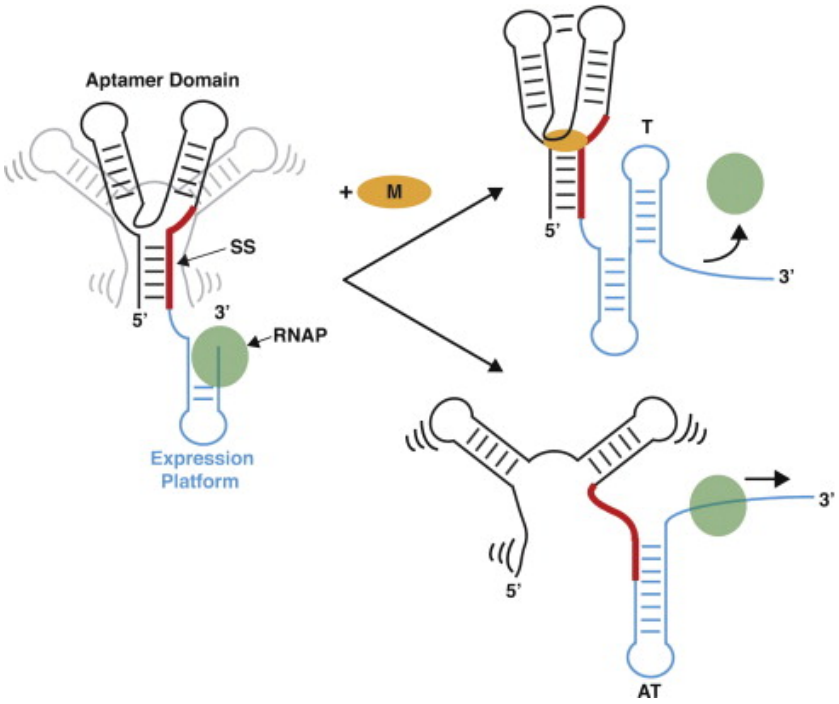

Figure 4.1: Example of gene expression regulation by a riboswitch: Riboswitch-regulated transcription termination. Reprinted from Garst and Batey (2009) [207], with permission from Elsevier. The aptamer domain (*black*/*gray*) forms prior to transcription of the expression platform (*cyan*), allowing this receptor to bind its metabolite (M; *orange*). Metabolite binding collapses the aptamer domain into a conformation that sequesters the switching sequence (SS) from pairing with the expression platform, leading to formation of a terminator stem (T), which attenuates transcription. In the event that ligand binding does not occur, particular elements of the aptamer domain remain loosely structured, leading to formation the antiterminator stem (AT), allowing RNA polymerase (RNAP) to continue transcribing.

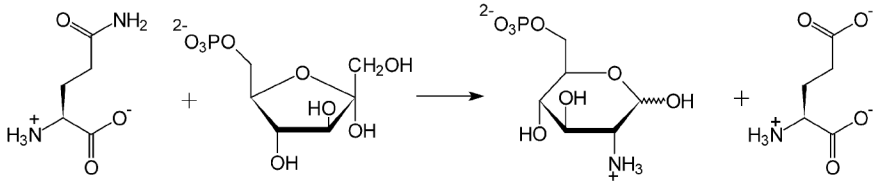

Figure 4.2: Reaction catalyzed by glucosamine-6-phosphate synthase. Reprinted from Milewski, Copyright (2002) [212], with permission from Elsevier.

Riboswitches are usually adjacent to genes involved in the synthesis or transport of their metabolite ligand [205]. Many candidates have been identified in searches for highly-conserved RNA domains that reside in intergenic regions of bacterial genomes [208, 209, 210]. Thus, the discovery of riboswitches has served as a powerful tool for inferring functions of uncharacterized genes [208, 211].

4.1.3 The *glmS* ribozyme-riboswitch

The *glmS* ribozyme was the first natural catalytic RNA discovered to require a small-molecule activator for catalysis [54]. This ribozyme-riboswitch is a conserved element in numerous Gram-positive bacteria in the 5′ untranslated region (UTR) of the mRNA encoding glucosamine-6-phosphate (GlcN6P) synthase. It functions by undergoing ligand-induced, site-specific self-cleavage that reduces gene expression through destabilization of the mRNA [54, 55]. GlcN6P synthase, formally known as glutamine-fructose-6-phosphate amidotransferase, is an enzyme that uses fructose-6-phosphate and glutamine to generate GlcN6P [212] (Figure 4.2). GlcN6P is the ligand that binds to the *glmS* ribozyme, providing a negative feedback signal for synthesis of the enzyme that produced it. The generation of GlcN6P is the first step in the pathway for the production of uridine 5′-diphospho-*N*-acetyl-D-glucosamine, which is subsequently used in the process of cell-wall biosynthesis.

X-ray crystallography studies reveal the architecture of the *glmS* ribozyme [213, 214, 215, 216]. The crystal structure of the *glmS* ribozyme with GlcN6P bound in the active site was solved to 2.5-

Å resolution [214] (Figure 4.3). The *glmS* ribozyme is ~50 Å wide and ~20 Å deep. It is comprised of a short, helical segment surrounded by two sets of coaxially-stacked helices . The short, central stack, P2.1, is sandwiched by a long stack, consisting of P1 and P3.1, and a smaller stack, consisting of P4 and P4.1.

The ribozyme core consists of a double-pseudoknot structure that comprises both the active site and the metabolite-binding pocket. The positioning of the central helix P2.1 and the adjacent helix P2.2, as well as that of a tightly bound metal ion, form the double pseudoknot by four nonhelical crossovers that connect the P1-P2.2-P2 stack with P2.1.

The ribozyme peripheral, comprised of P3, P3.1, P4, and P4.1, has been shown to be necessary for optimal self-cleavage rates at physiological Mg^{2+} concentrations [217, 218]. This accessory domain is anchored in position by a third pseudoknot between P3 and P3.1 at one end and by a tertiary interaction between P1 and and P4.1 at the other (Figure 4.3). Extensive contacts between the A-rich internal loop of the P4 element and the P2.1 minor groove serve to further buttress the catalytic core.

The atomic-resolution structures of the free and ligand-bound forms of the *glmS* ribozyme are nearly superimposable, indicating that ligand binding does not induce a conformational change in the RNA, as is typical of other riboswitches [213, 214, 215, 216].

In addition to the observed crystalline states of the *glmS* ribozyme, solution studies provide further evidence for a prefolded active site within a ribozyme structure that does not undergo a global conformational change upon GlcN6P binding [54, 219, 220]. Fluorescence resonance energy transfer (FRET) studies show that the global conformation does not change upon ligand binding [220]. Cross-link studies demonstrate that a UV cross-linked complex still exhibits catalytic activity [219]. Collectively, the crystallographic, FRET, and cross-link studies, indicating a rigid, preorganized fold, suggest that GlcN6P functions not as an allosteric effector but as a coenzyme, directly participating in catalysis.

Since the discovery of the *glmS* ribozyme, there has been evidence for a eukaryotic ribozyme riboswitch [221]. The CLEC2 ribozymes, variants of the hammerhead ribozyme found as a dis-

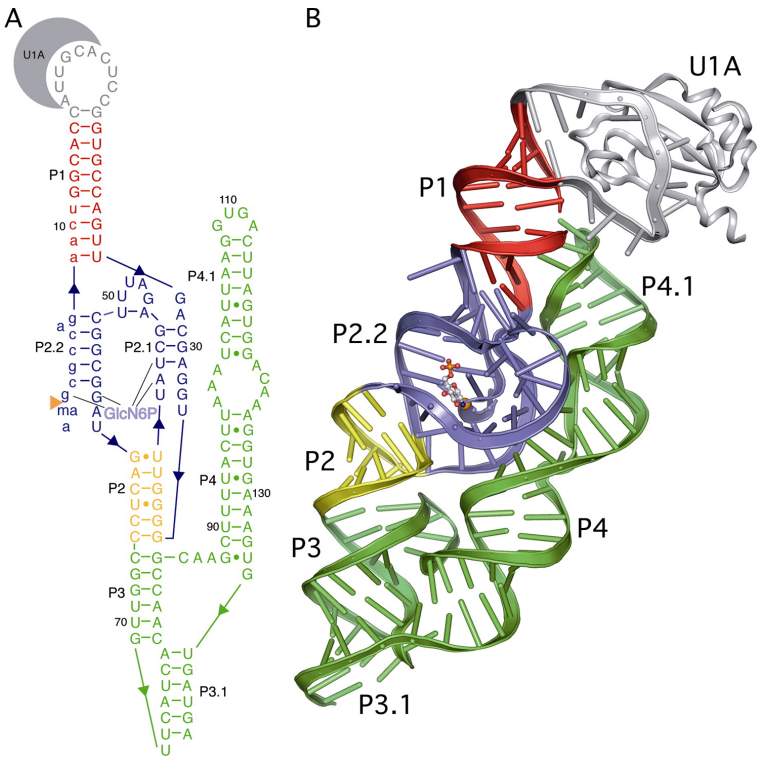

Figure 4.3: Structure of the *glmS* ribozyme. Reprinted from Cochrane *et al.*, Copyright (2007) [214], with permission from Elsevier. (A) Secondary structure of the *Bacillus anthracis glmS* ribozyme. (B) Tertiary structure depicted in ribbons format of the P1 helix (*red*); P2 helix (*yellow*); P3–P4 helices (*green*); double pseudoknot consisting of helices P2.1, P2.2, P2a, and related joiner regions (*blue*); and U1A and the U1A binding loop (*gray*). GlcN6P is bound in the active site and is shown in ball and stick representation.

continuous sequence in the 3′ UTR of rodent C-type lectin type II (*clec2*) genes, can self-cleave and reduce *clec2* gene expression in mouse cells. Although the specific effector for this putative riboswitch is still unknown, a mechanism controlling cleavage seems likely because if the ribozyme always cleaved, the *clec2* genes would never be expressed. The discovery of the *glmS* and CLEC2 ribozymes constitute specific examples of what may be a far more general regulatory phenomenon [222].

The study of the *glmS* ribozyme as a naturally-occurring biosensor may advance the development of artificial RNA-based biosensors. Aptamers, as discussed in subsection 4.1.1, are single-stranded nucleic acid molecules that bind their cognate ligands with high binding affinity and specificity. In this sense, they are comparable to monoclonal protein antibodies [223]. The development of aptamers has been accompanied by a growing range of applications in biosensor and medical technologies [53, 224].

In comparison with monoclonal antibodies, which are produced in cells, aptamer biosensors carry some distinct advantages [53]. First, aptamer biosensors can be selected for toxic and non-immunogenic targets. Second, modifications to the biosensor and assay conditions can be easily customized for the immobilization of biochips. Third, aptamers prove to be more resistant to denaturation than antibodies [225]. Fourth, aptamers have been shown to be active in the presence of organic solvents [226]. Finally, aptamers can be produced on a large scale though polymerase chain reaction and *in vitro* transcription, which is highly reproducible and inexpensive.

In this context, study of the *glmS* ribozyme provides insight into a mechanism for gene regulation by a ribozyme, as well as an example of an RNA-based biosensor, which may be applicable to further developments within the field of biosensors. Here, a single-molecule cleavage assay of the *glmS* ribozyme is developed and used to measure cleavage of single ribozymes. This proof-of-concept study demonstrates an assay for investigating nucleic-acid-based biosensors.

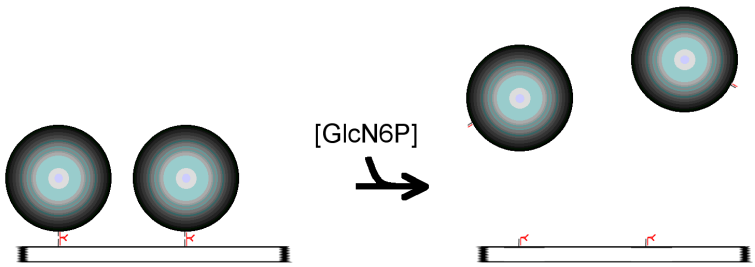

Figure 4.4: Schematic of the single-ribozyme cleavage assay. A RNA:DNA hybrid molecule is held between two points, a cover slip and a nanoparticle. The ribozyme (*red*) and DNA handles (*black*) are shown. Upon binding of glucosamine-6-phosphate (GlcN6P), the *glmS* ribozyme undergoes self-cleavage.

4.2 Materials and Methods

To allow monitoring of single cleavage events, single *glmS* ribozymes were immobilized on a surface. Each ribozyme was attached to a surface and to a 180-nm diameter nanoparticle via RNA:DNA hybrid handles and biological linkages (Figure 4.4). In our experiments, polystyrene nanospheres were antidigoxigenin-coated and adhered to the 3′ end of the digoxigenin-labeled DNA bound to the 5′ RNA terminus. The 5′ end of the DNA bound to the 3′ terminus of the RNA was biotinylated and bound tightly to the glass substrate via a streptavidin and biotinylated-BSA molecule. Upon addition of GlcN6P molecules, the ribozyme underwent self-cleavage and quickly diffused away from the surface.

We used two strategies to maintain attachment of each nanoparticle to the surface by a single RNA:DNA construct. First, we designed an RNA:DNA construct with very short handles of 30 base pairs each. This length is short compared to the diameter of the nanoparticle and spatially hinders simultaneous attachment of multiple RNA:DNA constructs to the same nanoparticle and to the surface. Second, when incubating nanoparticles with the RNA:DNA construct, we incubated with a 5:1 excess of nanoparticles, limiting the number of nanoparticles with more than one attachment. As confirmation that we do not observe kinetics due to multiply-tethered nanoparticles, we verified that the cleavage data do not fit to multiply-tethered nanoparticles by fitting the data to $y(t) = y_0 + B_1 \exp\left[-k(t-t_0)\right] + t\ B_2 \exp\left[-k(t-t_0)\right]$, where y is the fraction cleaved, t is the time after

GlcN6P is introduced, y_0 is an offset in y, B_1 and B_2 are amplitude coefficients, and k is the pseudo rate of cleavage.

4.2.1 RNA:DNA hybrid constructs

To tether single molecules of RNA to a nanoparticle and a surface, we used biotinylated-DNA and digoxigenin-labeled DNA at the ends of RNA:DNA constructs. Using hybrid constructs ensures that each tether will be hybridized on both sides of the ribozyme. Standard polymerase chain reaction (PCR) and cloning strategies were used to create a DNA plasmid comprising a T7 RNA polymerase promoter, a sequence complementary to the Handle A DNA, a 161-nucleotide insert of the *glmS* ribozyme, and a sequence complementary to the Handle B DNA (Figure 4.5).

It has been shown that *glmS* ribozymes possess considerable self-cleavage activity in the absence of ligand in TRIS-buffered solution [54, 227]. Thus, most reactions with the *glmS* RNA were performed in HEPES buffer. The *glmS* RNA was RNA was transcribed *in vitro* from PCR products. Transcription reactions consisted of 30 mM HEPES (pH 8.0), 10 mM dithiolthreitol, 0.1% Triton X-100, 0.1 mM spermidine-HCl, 4 mM each nucleotide triphosphate (Sigma-Aldrich, St. Louis, MO; pH adjusted to 8.0), 32 mM $MgCl_2$, 50 μg/ml T7 bacteriophage RNA polymerase, 1 unit/ml inorganic pyrophosphatase (Sigma-Aldrich), and template DNA at 9 μg/ml. Reactions were incubated for 2 h at 37 °C. The transcribed product was heated for 1 min at 90 °C and immediately ran on a denaturing polyacrylamide gel (8%; in TBE buffer with urea). The RNA was eluted overnight in an elution trap at 4 °C in TBE, then purified in an exchange column in 50 mM potassium HEPES (pH 7.5) and centrifuged at 36.5 krpm.

Short, 30-nt ssDNA oligomers, denoted "Handle A" and "Handle B," were end-labeled with either biotin or digoxigenin (Integrated DNA Technologies, Coralville, IA). Handle A and Handle B DNA are complementary to the $5'$ and $3'$ end sequences of the RNA, respectively. DNA and RNA were annealed with a DNA:RNA ratio of 4:1 and incubated for 80 min on ice. The annealed and unannealed DNA were separated using a nondenaturing polyacrylamide gel and recovered using standard crush-and-soak methods.

Handle A – *glmS* ribozyme –Handle B

5′ –

GGGAGAUGCGUGAGUGCGUUGCUUGUGGGUGCCGGCAU**AG**CGCCCGAACUACCGGUACC
GGUAGUUGACGAGGAUGGAGGUUAUCGAAUUUUCGGCGGAUGCCUCCCGGCUGAGUGUG
CAGAUCACAGCCGUAAGGAUUUCUUCAAACCAAGGGGGUGACUCCUUGAACAAAGAGAA
AUCACAUGAUCUUCCAAAAAUCUAGAGGUCGCUUGUCGGUCUUCUGACUGGCAGGC

5′ –

GGGAGATGCGTGAGTGCGTTGCTTGTGGGTGCCGGCATAGCGCCCGAACTACCGGTACC
GGTAGTTGACGAGGATGGAGGTTATCGAATTTTCGGCGGATGCCTCCCGGCTGAGTGTG
CAGATCACAGCCGTAAGGATTTCTTCAAACCAAGGGGGTGACTCCTTGAACAAAGAGAA
ATCACATGATCTTCCAAAAATCTAGAGGTCGCTTGTCGGTCTTCTGACTGGCAGGC

Figure 4.5: Sequence of the *glmS*-ribozyme-containing RNA used in the RNA:DNA construct. A 233-nt RNA construct was designed to contain the *glmS* ribozyme (*blue*) flanked with handles that base pair with DNA Handle A (*red*) and DNA Handle B (*green*). The RNA sequence (*top*) is shown. The cleavage site, indicated in bolded letters, is located near the 5′-end of the *glmS* ribozyme region. The DNA template for the RNA (*bottom*) is shown. Restriction-enzyme sites are underlined.

4.2.2 Protein-conjugated beads

To make the antidigoxigenin-coated nanoparticles, we coupled antidigoxigenin fragment-antigen-binding (Fab) fragments (Roche Applied Science, Indianopolis, IN) to 0.18-μm diameter spherical nanoparticles (Aldehyde/Sulfate latex particles; Interfacial Dynamics, Portland, OR; now Invitrogen, Carlsbad, CA) [87]. First, we passivated two 1.5 ml plastic tubes for 2 h at room temperature with 1.2 ml 2 mg/ml acetylated BSA (acBSA; Sigma-Aldrich) in phosphate buffered saline (PBS). The tubes were then rinsed with RNase-free (DEPC-treated) H_2O. One tube was used during the protocol and the other was used to store the final modified antidoxigenin beads at 4 °C.

Next, in the protocol tube, we washed latex beads (100 μl of 4.4% w/v 180-nm beads) 4 times in 1 ml PBS buffer (centrifuge for 9 min at 14 krpm to form a pellet, remove supernatant, resuspend in 1 ml PBS and pipette and vortex to suspend). After washing, beads were resuspended in 500 μl PBS with 20 μl of 80 mg/ml acBSA. Beads were sonicated for 40 min, or until fully separated. Next, we added 500 μl of 2 mg/ml anti-digoxigenin Fab fragments in PBS to the beads, mixed by pipetting, and incubated on a rotator ($>$ 24 h). After incubation, we centrifuged the beads to form a pellet (8 min at 14 krpm), removed the supernatant, and re-suspended them in 1.2 ml of 1.0 M glycine in PBS, incubating for 40 min on a rotator at room temperature to quench the reaction. Next we centrifuged again to form a pellet (8 min at 14 krpm) and removed the supernatant. We performed the final resuspension in PBS, 2.9 mg/ml acBSA, and 2% (w/v) sodium-azide, to form the final solution (~2 nM for 180 nm beads). The final, modified-bead solution was transferred to the other acBSA-passivated tube.

4.2.3 RNA tethered-bead assay with BSA surface passivation

One method to passivate the flow chambers was to use bovine serum albumin (BSA) and biotinylated BSA (bio-BSA) to immobilize the nucleic-acid constructs while rejecting protein adsorption (see Appendix A). BSA served to passivate the surface to prevent nonspecific attachment of the anti-digoxigenin-coated nanoparticles. Biotinylated BSA allowed specific attachment of RNA:DNA

constructs through a biotin-streptavidin linkage. To passivate the cover glass surface, a cover glass (20 x 40 mm, Corning Life Sciences) was first cleaned with potassium hydroxide dissolved in denatured ethanol. Next, flow chambers with an internal volume of 15 µl were constructed from a cleaned glass cover slip, a standard microscope slide (Corning Life Sciences), double-stick tape (3M, St. Paul, MN), and 5-minute epoxy (Devcon, Danvers, MA). The flow chamber was then incubated with a 125 µg/ml bio-BSA in 0.1 M sodium phosphate buffer for 20 min, washed with binding buffer [10 mM HEPES (pH 7.5), 150 mM potassium chloride, 0.4% Tween-20, and 3 mg/ml acetylated BSA] and incubated for 10 min.

Flow cells were next incubated with streptavidin (10 µg/ml in binding buffer) for 10 min, then washed with 400 µl of binding buffer. Nanoparticles were sonicated, then incubated 1 h with RNA:DNA constructs at a 5:1 mol ratio (900 pM nanoparticles) in binding buffer [10 mM HEPES (pH 7.5), 150 mM KCl, 0.4% Tween-20 (BioRad, Hercules, CA), and 3 mg/ml acBSA]. Next, nanoparticle-oligo complexes were flowed through the flow cells at a concentration of 188 pM nanoparticles. After 20 min of incubation, flow cells were washed with 400 µl of binding buffer. The enzymatic reaction was initiated by flowing in 50 µl reaction buffer [50 mM HEPES (pH 7.5), 150 mM KCl, 1 mM $MgCl_2$, and varying concentrations of GlcN6P].

4.2.4 RNA tethered-bead assay with PEG surface passivation

A second method to tether RNA to passivated flow chambers utilized polyethylene glycol (PEG) surfaces [228]. We used customized protocols for covalently attaching PEG molecules to the glass slide and cover glass surface, which involved careful storage and handling of the materials, details of which are explained in [87]. The protocol is briefly summarized here. First, slides and cover glasses were plasma-cleaned, then KOH-cleaned. Next, we performed aminosilanization on the glass surfaces by incubating for 20 min in a solution containing aminopropylsilane [N-(2-Aminoethyl)-3-Aminopropyltrimethoxysilane (UCT A0700)] and methanol. After aminosilanization, we rinsed with methanol, diH_2O, 1M KOH, and plenty of diH_2O, and dried with nitrogen gas. We then assembled the aminosilanated cover glass and glass slide into flow cells with no epoxy.

Next, PEG was covalently attached using a 60:1 ratio mix of methoxy-PEG (mPEG) and biotinylated-PEG (bio-PEG) molecules, dissolved in 0.1 M sodium bicarbonate bu?er. PEG solution was flowed into the assembled, aminosilanated samples, which were then incubated for 3–4 hours in a dark humidity chamber. After incubation, we rinsed the ßow cells with diH_2O, dried them with nitrogen, and stored them in black-tape wrapped bottles that were vacuum sealed.

Flow cells were rinsed with 200 µl of Tris buffered saline [TBS; 20 mM Tris-Cl (pH 7.3) and 200 µl of 150 mM NaCl] and Wash Buffer [WB; 10 mM HEPES (pH 7.3), 100 mM KCl, and 1 mM $MgCl_2$] before incubated with streptavidin (0.1 mg/ml in TBS) for 30 min, then washed with 400 µl of TBS and 400 µl of WB. Nanoparticles were sonicated, then mixed and incubated 1 h with RNA:DNA constructs at a 5:1 mol ratio (375 pM nanoparticles) in binding buffer [10 mM HEPES (pH 7.5), 50 mM KCl, and 3 mg/ml filtered acBSA] at 4 °C. Next, nanoparticle-oligo complexes were flowed through the flow cells at a concentration of 188 pM nanoparticles and incubated for 20 min at 4 °C. Then, flow cells were washed with 600 µl of WB. The enzymatic reaction was initiated by flowing in 50 µl reaction buffer [50 mM HEPES (pH 7.5), 150 mM KCl, 1 mM $MgCl_2$, and varying concentrations of GlcN6P].

4.2.5 Single-molecule data acquisition and analysis

We used tethered-particle microscopy and measured single cleavage events in real time. A wide-field differential-interference-contrast (DIC) inverted microscope (TE 2000-S; Nikon Corporation, Japan) with 100x oil immersion objective (Nikon Plan Fluor, 100x/1.30 oil DIC H; Nikon Corporation, Japan) was used to image an area of 100 x 100 μm^2 to a charge-coupled device camera (CCD100; Dage-MTI, Michigan City, IN). Cleavage events were observed as previously immobile nanoparticles that suddenly diffused away from the cover-glass surface.

The recorded image was digitized and analyzed (Vision Assistant; National Instruments, Austin, TX). Analysis included enhancing the brightness and contrast of the image, converting the image to binary, calculating the sum signal of the region of interest for each nanoparticle, and determining in which frame the nanoparticle disappeared from the image with a customized,

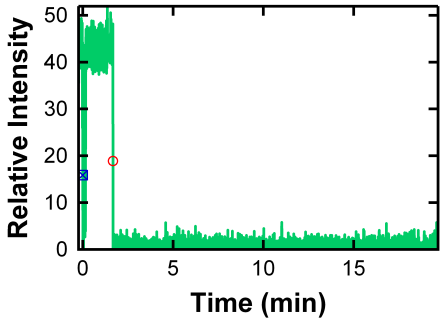

Figure 4.6: Signal of a cleavage event as measure with a tethered-particle assay. The time course is a representative trace of the enhanced sum signal measured by the CCD camera of a selected region of interest. An automated algorithm determines the start time (*blue square*) and the cleavage time (*red circle*).

automated procedure (Igor Pro; WaveMetrics, Portland, OR) (Figure 4.6). The threshold value was set halfway between the maximum intensity of the region of interest and the background.

4.2.6 Ensemble FRET experiments

We also studied freely diffusing RNA:DNA constructs using fluorescence resonance energy transfer (FRET). Here, we used RNA:DNA constructs with a 34-nt DNA labeled with Alexa-546 at the 5′ end annealed to the 5′ end of the RNA and 41-nt DNA labeled with Alexa-647 at the 3′ end annealed to the 3′ end of the RNA. Fluorescence values were measured using a fluorometer (Fluorolog-3™; Jobin Yvon, now HORIBA Jobin Yvon Inc, Edison, NJ), FluorEssence™ software, and a 50 µl cuvette. The FRET signal was measured by exciting the sample at 530 nm, which primarily excites the donor, and collecting the acceptor emission at 667 nm, with excitation and emission slits set to a 5-nm bandpass. Annealed ribozymes (final concentration 5 nM) were incubated at 25 °C for at least 15 min in 50 mM HEPES (pH 7.5) and 150 mM KCl, and then transferred to a 50 µl cuvette. GlcN6P and $MgCl_2$ was manually added to concentrations of 30 *umu*M and 1 mM, respectively. Photobleaching was negligible, as indicated by measurement of the acceptor emission spectrum before and after cleavage (data not shown).

The decrease in FRET efficiency from cleavage resulted in a time-dependent decrease in

acceptor emission. These data were used to determine the apparent rate constant for cleavage, k_{obs}, by fitting the FRET acceptor fluorescence, A, to a single exponential,

$$A(t) = A_0 e^{-k_{\text{obs}} t} + A_{\text{offset}}, \tag{4.1}$$

where k_{obs} is the observed rate of cleavage, A_0 is the fluorescence at time zero, and A_{offset} is the change in fluorescence between time zero and infinite time. The normalized acceptor fluorescence was normalized by the equation $y = (A - A_{\text{offset}})/A_0$.

4.3 Preliminary Results

4.3.1 Cleavage of single *glmS* ribozymes

We observe cleavage events of the surface-immobilized ribozyme by video microscopy. Enzymatic activities of the ribozymes were monitored by observing when the nanoparticle left the surface. The reaction time course is shown in Figure 4.7. The fraction cleaved was fit to the double exponential equation

$$y(t) = y_0 + C_1 \exp(-k_1 t) + C_2 \exp(-k_2 t), \tag{4.2}$$

where y is the fraction cleaved, t is the time after GlcN6P is introduced, y_0 is the offset in y, C_1 and C_2 are amplitude coefficients, and k_1 and k_2 are the pseudo-rate constants of cleavage. The data do not fit to a single exponential, which suggests heterogeneous reaction kinetics that are described with two or more distinct cleavage-rate constants. We observed cleavage rates from one flow cell of $k_1 = 1.96 \pm 0.30$ min^{-1} and $k_2 = 0.28 \pm 0.13$ min^{-1} and amplitude coefficients of $C_1 = -0.67 \pm 0.09$ and $C_2 = -0.33 \pm 0.03$ at higher concentration of ligand [50 mM HEPES (pH 7.5), 150 mM KCl, 1 mM $MgCl_2$, and 200 μM GlcN6P] on a BSA-coated surface. We also observed slower cleavage rates from the combined data of two flow cells of $k_1 = 0.82 \pm 0.07$ min^{-1} and $k_2 = 0.06 \pm 0.04$ min^{-1} and amplitude coefficients of $C_1 = -0.72 \pm 0.04$ and $C_2 = -0.35 \pm 0.07$ at lower concentration of ligand [50 mM HEPES (pH 7.5), 150 mM KCl, 10 mM $MgCl_2$, and 50 μM GlcN6P] on PEG-coated surfaces. Preliminary results indicate double-exponential kinetics that were present on both BSA-passivated and PEG-passivated surfaces.

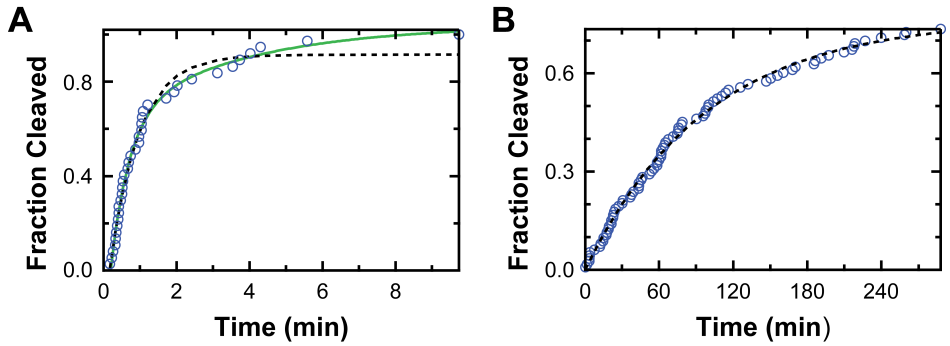

Figure 4.7: Single-molecule measurements of *glmS* ribozyme cleavage. The blue open circles show the reaction time course of the surface-immobilized ribozyme. The dashed black (solid green) curve is a numerical fit to a single (double) exponential. (A) Ligand is present. Measurement of one flow cell of *glmS* ribozymes in in 50 mM HEPES (pH 7.5), 150 mM KCl, 1 mM $MgCl_2$, and 200 µM GlcN6P. (B) No ligand is present. Measurement of one flow cell of *glmS* ribozymes in in 50 mM HEPES (pH 7.5), 150 mM KCl, and 1 mM $MgCl_2$.

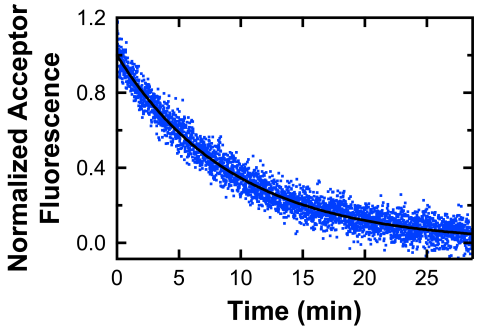

Figure 4.8: Real-time ensemble measurement of *glmS* ribozyme cleavage. Time dependence of the acceptor fluorescence after mixing with GlcN6P and Mg^{2+}. Rates of cleavage were measured (*blue dots*) and fit to a single exponential (*black line*).

We also performed control experiments to test whether *glmS* ribozymes were undergoing self-cleavage in the absence of GlcN6P. We observed a background cleavage rate from one flow cell of 0.0102 ± 0.0003 min^{-1} in 50 mM HEPES (pH 7.5), 150 mM KCl, and 1 mM $MgCl_2$ (Figure 4.7) on a PEG-passivated surface.

4.3.2 Cleavage of an ensemble of *glmS* ribozymes

To verify that the functional properties of the ribozyme were not compromised by surface immobilization, we measured reaction kinetics for a similar construct in solution. Measuring identical values would indicate that the surface is not changing the cleavage kinetics. We excited the donor and monitor the intensity of the acceptor fluorescence of samples of an ensemble of ribozymes in solution. In preliminary results, we obtained the cleavage rate for the RNA:DNA construct in solution as 0.106 min^{-1} (Figure 4.8), which is smaller than the expected rate under similar conditions [54]. Further measurements of the cleavage rate with varying ligand and Mg^{2+} concentrations must be performed to determine whether the cleavage kinetics of our *glmS* ribozyme construct are altered as compared to those of a *glmS* ribozyme that does not contain engineered RNA:DNA handles. Also, the ensemble measurements did not retrieve double-exponential kinetics, which could be due to a lack of resolution or due to the double-exponential kinetics being a surface-dependent artifact.

4.4 Summary

We designed and implemented a single-molecule *glmS* ribozyme cleavage assay with tethered nanoparticles using short RNA:DNA constructs. This proof-of-concept study is a new single-molecule measurement of *glmS* ribozyme cleavage. Our methods can potentially be expanded to nucleic-acid-based biosensors utilizing other aptamer domains. Previous studies have attempted to create variants of the *glmS* ribozyme that cleave upon binding of target molecules other than GlcN6P [229], raising the prospect of creating cleavable biosensors made of RNA. Use of the specificity of riboswitches to create highly-specific biosensors is being explored [48, 49, 50].

Chapter 5

Conclusions and Future Directions

5.1 Conclusions

The studies presented here signify the first direct measurements of RecBCD·DNA destabilization dynamics. We observed large conformational destabilization dynamics of the RecBCD·DNA complex that were on the order of multiple base pairs. This type of measurement is only possible with an assay that can resolve subnanometer changes in position, which was accomplished using an actively-stabilized optical-trapping assay. In this thesis, we present two new, major observations detailing RecBCD helicase mechanism. First, to conclude that the helicase was destabilizing the duplex region of the DNA substrate, it was necessary to study the conformational dynamics of RecBCD bound to an interstrand cross-linked DNA substrate. We observed dramatically-altered conformational dynamics in the presence of the cross link, providing strong evidence that the enzyme actively destabilizes the DNA duplex region. Second, we measured significantly-reduced conformational dynamics in the presence of nonhydrolyzable ATP analogs. This result suggests that the destabilization dynamics are modulated by the nucleotide-bound state of RecBCD and may be an important aspect of helicase function, particularly in the mechanisms of active helicases.

Additionally, we developed an original single-molecule cleavage assay of the *glmS* ribozyme, the first-discovered catalytic riboswitch. The work presented here is one of the first single-molecule studies of the *glmS* ribozyme. This cleavage assay has the potential to be expanded to examine other biosensors that utilize aptamer domains. Despite the fact that nucleic acids have more limited chemical functionality than proteins, the target binding properties of aptamers can rival those

of antibodies, and nucleic acids possess a number of advantages over antibodies, including easier synthesis and superior transduction.

5.2 Future Directions

5.2.1 Further characterization of back-and-forth dynamics

Improved resolution of the RecBCD optical-trapping assay may be attained by repositioning the biotin moiety. The derivative of RecBCD (RecBCD-bio) that we used in our studies has a genetically-engineered biotin moiety near the carboxy terminus of the RecD subunit. Placing the biotin moiety at a different position on the enzyme can be achieved by posttranslational modification [230]. Modification of the enzyme would require demonstration that the new RecBCD derivative is still functional *in vivo* and still exhibits helicase and DNA-dependent ATPase activities *in vitro* analogous to those of wild-type RecBCD. With this approach, it may be possible to measure the most highly-dynamic regions of the RecBCD·DNA complex with improved spatio-temporal resolution. Resolving the dynamics has the potential to reveal additional details of the translocation stepping mechanism.

5.2.2 Quantification of duplex destabilization by the helicase

There are two methods of quantifying the extent to which a helicase destabilizes the junction. In one method, the velocity of the helicase unwinding dsDNA is compared to the velocity of helicase translocation along ssDNA. This method has been explored in several single-molecule studies [72, 114, 117, 120]. In the second method, the dependence of the unwinding velocity of the helicase on the GC-content of the double-stranded nucleic acid is examined [72, 118].

Since RecBCD will not bind to ssDNA, one strategy that could be employed in the first method is to use DNA substrates with double-stranded regions and ssDNA gaps to induce translocation of RecBCD on ssDNA [231]. For our RecBCD optical-trapping assay, a long DNA substrate (e.g., $L > 500$ nm) is needed to measure translocation. Such a DNA construct could be constructed with

double-stranded regions and a non-base-paired ssDNA region. An approach which would allow use of the second method is to design a DNA construct with tandem repeats of GC-rich and AT-rich sequences. In conjunction, these methods may elucidate duplex destabilization by RecBCD.

5.2.3 Characterization of the RecB motor and RecBCD after Chi recognition

The RecBCD optical-trapping assay can be used to directly measure the stepping behavior of the RecB motor of RecBCD. The RecBCD·DNA complex did not exhibit large conformational dynamics when bound to DNA with a $3'$-$(dT)_6$ noncomplementary DNA tail, in spite of interaction between the $3'$ DNA end with the RecB motor [191]. This begs the question of whether the destabilization dynamics are present when RecB is the lead helicase motor. Comparison of unwinding rates of a disabled-RecD-motor mutant ($RecBCD^{K177Q}$) with unwinding rates of RecBCD before and after Chi provided evidence that RecD (RecB) is the lead motor of RecBCD before (after) Chi recognition [139]. In these studies, when RecD was the lead motor, RecBCD unwound DNA roughly twice as fast as when RecB was the lead motor. Understanding the mechanistic basis of these two superfamily-1 helicases and how they differ would bring further understanding to general helicase mechanism.

Bibliography

[1] J. M. Berg, J. L. Tymoczko, and L. Stryer. Biochemistry. W. H. Freeman and Company, New York, 5th edition, 2002.

[2] K. E. Neet. Enzyme catalytic power minireview series. Journal of Biological Chemistry, 273(40):25527–25528, 1998.

[3] A. L. Lehninger, D. L. Nelson, and M. M. Cox. Lehninger Principles of Biochemistry. W. H. Freeman and Company, New York, NY, 4th edition, 2005.

[4] P. K. Agarwal. Enzymes: An integrated view of structure, dynamics and function. Microbial Cell Factories, 5(2), 2006.

[5] C. Bustamante, Y. R. Chemla, N. R. Forde, and D. Izhaky. Mechanical processes in biochemistry. Annual Review of Biochemistry, 73(1):705–748, 2004.

[6] S. B. Smith, L. Finzi, and C. Bustamante. Direct mechanical measurements of the elasticity of single DNA molecules by using magnetic beads. Science, 258(5085):1122–1126, 1992.

[7] T. Strick, J. F. Allemand, V. Croquette, and D. Bensimon. The manipulation of single biomolecules. Physics Today, 54(10):46–51, 2001.

[8] T. R. Strick, J. Allemand, D. Bensimon, A. Bensimon, and V. Croquette. The elasticity of a single supercoiled DNA molecule. Science, 271(5257):1835–1835, 1996.

[9] K. Svoboda, C. F. Schmidt, B. J. Schnapp, and S. M. Block. Direct observation of kinesin stepping by optical trapping interferometry. Nature, 365(6448):721–727, 1993.

[10] E. Betzig and R. J. Chichester. Single molecules observed by near-field scanning optical microscopy. Science, 262(5138):1422–1425, 1993.

[11] W. E. Moerner and L. Kador. Optical detection and spectroscopy of single molecules in a solid. Physical Review Letters, 62(21):2535–2538, 1989.

[12] M. Orrit and J. Bernard. Single pentacene molecules detected by fluorescence excitation in a p-terphenyl crystal. Physical Review Letters, 65(21):2716–2719, 1990.

[13] C. Bustamante. *In singulo* biochemistry: When less is more. Annual Review of Biochemistry, 77(1):45–50, 2008.

[14] I. J. Finkelstein and E. C. Greene. Single molecule studies of homologous recombination. Molecular BioSystems, 4(11):1094–1104, 2008.

[15] P. Hinterdorfer and A. van Oijen. Handbook of single-molecule biophysics. Springer Verlag, 2009.

[16] C. Joo, H. Balci, Y. Ishitsuka, C. Buranachai, and T. Ha. Advances in single-molecule fluorescence methods for molecular biology. Annual Review of Biochemistry, 77(1):51–76, 2008.

[17] J. R. Moffitt, Y. R. Chemla, K. Aathavan, S. Grimes, P. J. Jardine, D. L. Anderson, and C. Bustamante. Intersubunit coordination in a homomeric ring ATPase. Nature, 457(7228):446–450, 2009.

[18] K. Aathavan, A. T. Politzer, A. Kaplan, J. R. Moffitt, Y. R. Chemla, S. Grimes, P. J. Jardine, D. L. Anderson, and C. Bustamante. Substrate interactions and promiscuity in a viral DNA packaging motor. Nature, 461(7264):669–673, 2009.

[19] P. V. Cornish, D. N. Ermolenko, H. F. Noller, and T. Ha. Spontaneous intersubunit rotation in single ribosomes. Molecular Cell, 30(5):578–588, 2008.

[20] J. G. Yodh, M. Schlierf, and T. Ha. Insight into helicase mechanism and function revealed through single-molecule approaches. Quarterly Reviews of Biophysics, 43(02):185–217, 2010.

[21] T. M. Lohman, E. J. Tomko, and C. G. Wu. Non-hexameric DNA helicases and translocases: mechanisms and regulation. Nature Reviews Molecular Cell Biology, 9(5):391–401, 2008.

[22] S. Myong and T. Ha. Stepwise translocation of nucleic acid motors. Current Opinion in Structural Biology, 20(1):121–127, 2010.

[23] M. S. Dillingham and S. C. Kowalczykowski. RecBCD enzyme and the repair of double-stranded DNA breaks. Microbiology and Molecular Biology Reviews, 72:642–671, 2008.

[24] A. L. Lucius, C. J. Wong, and T. M. Lohman. Fluorescence stopped-flow studies of single turnover kinetics of *E. coli* RecBCD helicase-catalyzed DNA unwinding. Journal of Molecular Biology, 339(4):731–750, 2004.

[25] A. L. Lucius, N. K. Maluf, C. J. Fischer, and T. M. Lohman. General methods for analysis of sequential "n-step" kinetic mechanisms: application to single turnover kinetics of helicase-catalyzed DNA unwinding. Biophysical Journal, 85(4):2224–2239, 2003.

[26] A. L. Lucius and T. M. Lohman. Effects of temperature and ATP on the kinetic mechanism and kinetic step-size for *E. coli* RecBCD helicase-catalyzed DNA unwinding. Journal of Molecular Biology, 339(4):751–771, 2004.

[27] J. Y. Lee and W. Yang. UvrD helicase unwinds DNA one base pair at a time by a two-part power stroke. Cell, 127(7):1349–1360, 2006.

[28] K. Saikrishnan, B. Powell, N. J. Cook, M. R. Webb, and D. B. Wigley. Mechanistic basis of $5'$-$3'$ translocation in SF1B helicases. Cell, 137(5):849–859, 2009.

[29] S. S. Velankar, P. Soultanas, M. S. Dillingham, H. S. Subramanya, and D. B. Wigley. Crystal structures of complexes of PcrA DNA helicase with a DNA substrate indicate an inchworm mechanism. Cell, 97(1):75–84, 1999.

[30] T. T. Perkins, H. W. Li, R. V. Dalal, J. Gelles, and S. M. Block. Forward and reverse motion of single RecBCD molecules on DNA. Biophysical Journal, 86(3):1640–1648, 2004.

[31] A. R. Carter, Y. Seol, and T. T. Perkins. Precision surface-coupled optical-trapping assay with one-basepair resolution. Biophysical Journal, 96(7):2926–2934, 2009.

[32] C. G. Wu and T. M. Lohman. Influence of DNA end structure on the mechanism of initiation of DNA unwinding by the *Escherichia coli* RecBCD and RecBC helicases. Journal of Molecular Biology, 382(2):312–326, 2008.

[33] C. Guerrier-Takada, K. Gardinier, T. Pace, and S. Altman. The RNA moiety of ribonuclease P is the catalytic subunit of the enzyme. Cell, 35:849–857, 1983.

[34] K. Kruger, P. J. Grabowski, A. J. Zaug, J. Sands, D. E. Gottschling, and T. R. Cech. Self-splicing RNA: autoexcision and autocyclization of the ribosomal RNA intervening sequence of Tetrahymena. Cell, 31(1):147–157, 1982.

[35] A. P. Carter, W. M. Clemons, D. E. Brodersen, R. J. Morgan-Warren, B. T. Wimberly, and V. Ramakrishnan. Functional insights from the structure of the 30S ribosomal subunit and its interactions with antibiotics. Nature, 407:340–348, 2000.

[36] P. Nissen, J. Hansen, N. Ban, and P. B. Moore. The structural basis of ribosome activity in peptide bond synthesis. Science, 289:920–930, 2000.

[37] H. F. Noller, V. Hoffarth, and L. Zimniak. Unusual resistance of peptidyl transferase to protein extraction procedure. Science, 265:1709–12, 1992.

[38] S. Valadkhan and J. L. Manley. Intrinsic metal binding by a spliceosomal RNA. Nature Structural Biology, 9:498–499, 2002.

[39] T. Villa, J. A. Pleiss, and C. Guthrie. Spliceosomal snRNAs: Mg^{2+}-dependent chemistry at the catalytic core? Cell, 109:149–52, 2002.

[40] X. Zhuang. Single-molecule RNA science. Annual Review of Biophysics and Biomolecular Structure, 34:399–414, 2005.

[41] D. P. Bartel. MicroRNAs: genomics, biogenesis, mechanism, and function. Cell, 116:281–297, 2004.

[42] J. C. Carrington and V. Ambros. Role of microRNAs in plant and animal development. Science, 301(5631):336–338, 2003.

[43] S. Gottesman. The small RNA regulators of *Escherichia coli*: roles and mechanisms. Annual Review of Microbiology, 58:303–328, 2004.

[44] K. M. Wassarman. RNA regulators of transcription. Nature Structural & Molecular Biology, 11:803–804, 2004.

[45] P. Burgstaller, A. Jenne, and M. Blind. Aptamers and aptazymes: Accelerating small molecule drug discovery. Current Opinion in Drug Discovery & Development, 5:690–700, 2002.

[46] M. Famulok and S. Verma. In vivo-applied functional RNAs as tools in proteomics and genomics research. Trends in Biotechnology, 20:462–66, 2002.

[47] B. A. Sullenger and E. Gilboa. Emerging clinical applications of RNA. Nature, 418:252–258, 2002.

[48] R. R. Breaker. Natural and engineered nucleic acids as tools to explore biology. Nature, 432(7019):838–845, 2004.

[49] J. Liu, Z. Cao, and Y. Lu. Functional nucleic acid sensors. Chemical Reviews, 109(5):1948–1998, 2009.

[50] S. K. Silverman. Rube Goldberg goes (ribo)nuclear? Molecular switches and sensors made from RNA. RNA, 9:377–383, 2003.

[51] D. H. J. Bunka and P. G. Stockley. Aptamers come of age – at last. Nature Reviews Microbiology, 4(8):588–596, 2006.

[52] C. K. O'Sullivan. Aptasensors – the future of biosensing? Analytical and Bioanalytical Chemistry, 372(1):44–48, 2002.

[53] J. E. Weigand and B. Suess. Aptamers and riboswitches: perspectives in biotechnology. Applied Microbiology and Biotechnology, 85(2):229–236, 2009.

[54] W. C. Winkler, A. Nahvi, A. Roth, J. A. Collins, and R. R. Breaker. Control of gene expression by a natural metabolite-responsive ribozyme. Nature, 428(6980):281–286, 2004.

[55] J. A. Collins, I. Irnov, S. Baker, and W. C. Winkler. Mechanism of mRNA destabilization by the glmS ribozyme. Genes & Development, 21(24):3356–3368, 2007.

[56] T. Lindahl. Instability and decay of the primary structure of DNA. Nature, 362(6422):709–715, 1993.

[57] T. Lindahl and R. D. Wood. Quality control by DNA repair. Science, 286(5446):1897–1905, 1999.

[58] D. E. Barnes and T. Lindahl. Repair and genetic consequences of endogenous DNA base damage in mammalian cells. Annual Review of Genetics, 38:445–476, 2004.

[59] C. B. Millar, J. Guy, O. J. Sansom, J. Selfridge, E. MacDougall, B. Hendrich, P. D. Keightley, S. M. Bishop, A. R. Clarke, and A. Bird. Enhanced CpG mutability and tumorigenesis in MBD4-deficient mice. Science, 297(5580):403–405, 2002.

[60] E. Wong, K. Yang, M. Kuraguchi, U. Werling, E. Avdievich, K. Fan, M. Fazzari, B. Jin, A. M. C. Brown, M. Lipkin, and W. Edelmann. Mbd4 inactivation increases C→T transition mutations and promotes gastrointestinal tumor formation. Proceedings of the National Academy of Sciences of the United States of America, 99(23):14937–14942, 2002.

[61] C. Bustamante, Z. Bryant, and S. B. Smith. Ten years of tension: Single-molecule DNA mechanics. Nature, 421(6921):423–427, 2003.

[62] S. B. Smith, Y. Cui, and C. Bustamante. Overstretching B-DNA: the elastic response of individual double-stranded and single-stranded DNA molecules. Science, 271(5250):795–799, 1996.

[63] M. D. Wang, H. Yin, R. Landick, J. Gelles, and S. M. Block. Stretching DNA with optical tweezers. Biophysical Journal, 72(3):1335–1346, 1997.

[64] R. Langridge, H. R Wilson, C. W. Hooper, M. H. F. Wilkins, and L. D. Hamilton. The molecular configuration of deoxyribonucleic acid: I. X-ray diffraction study of a crystalline form of the lithium salt. Journal of Molecular Biology, 2(1):19–37, 1960.

[65] R. Wing, H. Drew, T. Takano, C. Broka, S. Tanaka, K. Itakura, and R. E. Dickerson. Crystal structure analysis of a complete turn of B-DNA. Nature, 287(5784):755–758, 1980.

[66] P. J. Hagerman. Flexibility of DNA. Annual Review of Biophysics and Biophysical Chemistry, 17(1):265–286, 1988.

[67] B. Tinland, A. Pluen, J. Sturm, and G. Weill. Persistence length of single-stranded DNA. Macromolecules, 30(19):5763–5765, 1997.

[68] M. T. Woodside and M. T. Valentine. Single-molecule manipulation using optical traps. In P. Hinterdorfer and A. van Oijen, editors, Handbook of Single-Molecule Biophysics, chapter 12, pages 341–370. Springer/Kluwer Academic Publishers, 2009.

[69] J. F. Marko and E. D. Siggia. Stretching DNA. Macromolecules, 28(26):8759–8770, 1995.

[70] K. C. Neuman and S. M. Block. Optical trapping. Review of Scientific Instruments, 75(9):2787–2809, 2004.

[71] U. Bockelmann, B. Essevaz-Roulet, and F. Helsot. Molecular stick-slip motion revealed by opening DNA with piconewton forces. Physical Review Letters, 79:4489–4492, 1997.

[72] D. S. Johnson, L. Bai, B. Y. Smith, S. S. Patel, and M. D. Wang. Single-molecule studies reveal dynamics of DNA unwinding by the ring-shaped T7 helicase. Cell, 129(7):1299–1309, 2007.

[73] J. A. Doudna and J. R. Lorsch. Ribozyme catalysis: not different, just worse. Nature Structural & Molecular Biology, 12(5):395–402, 2005.

[74] J. Zhang, M. W. Lau, and A. R. Ferré-D'Amaré. Ribozymes and riboswitches: Modulation of RNA function by small molecules. Biochemistry, 49(43):9123–9131, 2010.

[75] J. R. Moffitt, Y. R. Chemla, S. B. Smith, and C. Bustamante. Recent advances in optical tweezers. Annual Review of Biochemistry, 77(1):205–228, 2008.

[76] A. Ashkin. Optical trapping and manipulation of neutral particles using lasers. Proceedings of the National Academy of Sciences of the United States of America, 94(10):4853–4860, 1997.

[77] K. Svoboda and S. M. Block. Biological applications of optical forces. Annual Review of Biophysics and Biomolecular Structure, 23:247–285, 1994.

[78] A. R. Carter, G. M. King, T. A. Ulrich, W. Halsey, D. Alchenberger, and T. T. Perkins. Stabilization of an optical microscope to 0.1 nm in three dimensions. Applied Optics, 46(3):421–427, 2007.

[79] J. D. Jackson. Classical Electrodynamics. Wiley, New York, 3rd edition, 1998.

[80] A. Ashkin. Forces of a single-beam gradient laser trap on a dielectric sphere in the ray optics regime. Biophysical Journal, 61(2):569–582, 1992.

[81] E. A. Abbondanzieri, W. J. Greenleaf, J. W. Shaevitz, R. Landick, and S. M. Block. Direct observation of base-pair stepping by RNA polymerase. Nature, 438(7067):460–465, 2005.

[82] J. R. Moffitt, Y. R. Chemla, D. Izhaky, and C. Bustamante. Differential detection of dual traps improves the spatial resolution of optical tweezers. Proceedings of the National Academy of Sciences of the United States of America, 103(24):9006–9011, 2006.

[83] L. Nugent-Glandorf and T. T. Perkins. Measuring 0.1-nm motion in 1 ms in an optical microscope with differential back-focal-plane detection. Optics Letters, 29(22):2611–2613, 2004.

[84] F. Gittes and C. F. Schmidt. Interference model for back-focal-plane displacement detection in optical tweezers. Optics Letters, 23(1):7–9, 1998.

[85] A. Pralle, M. Prummer, E.-L. Florin, E. H. K. Stelzer, and J. K. H. Hörber. Three-dimensional high-resolution particle tracking for optical tweezers by forward scattered light. Microscopy Research and Technique, 44(5):378–386, 1999.

[86] K. Visscher, S. P. Gross, and S. M. Block. Construction of multiple-beam optical traps with nanometer-resolution position sensing. IEEE Journal of Selected Topics in Quantum Electronics, 2(4):1066–1076, 1996.

[87] A. E. Carpenter. Human TATA-Binding Protein Interactions with DNA Characterized by Stabilized, Axial Optical Trapping. PhD thesis, University of Colorado at Boulder, 2011.

[88] P. Marchand and L. Marmet. Binomial smoothing filter: A way to avoid some pitfalls of least-squares polynomial smoothing. Review of Scientific Instruments, 54(8):1034–1041, 1983.

[89] M. C. Wang and G. E. Uhlenbeck. On the theory of the Brownian motion II. Reviews of Modern Physics, 17(2, 3):323–342, 1945.

[90] A. R. Carter. A precision optical trapping assay: Measuring the conformational dynamics of single *E. coli* RecBCD helicases. PhD thesis, University of Colorado at Boulder, 2008.

[91] K. M. Dohoney and J. Gelles. χ-sequence recognition and DNA translocation by single RecBCD helicase/nuclease molecules. Nature, 409(6818):370–374, 2001.

[92] T. T. Perkins and H. W. Li. Single-molecule studies of RecBCD. In M. M. Abdelhaleem, editor, Helicases: Methods and Protocols, volume 587, chapter 11, pages 155–172. Springer, Clifton, NJ, 2010.

[93] S. T. Lovett, C. Luisi-DeLuca, and R. D. Kolodner. The genetic dependence of recombination in recD mutants of *Escherichia coli*. Genetics, 120(1):37–45, 1988.

[94] T. M. Lohman and K. P. Bjornson. Mechanisms of helicase-catalyzed DNA unwinding. Annual Review of Biochemistry, 65(1):169–214, 1996.

[95] S. W. Matson, D. W. Bean, and J. W. George. DNA helicases: enzymes with essential roles in all aspects of DNA metabolism. Bioessays, 16(1):13–22, 1994.

[96] M. R. Singleton, M. S. Dillingham, and D. B. Wigley. Structure and mechanism of helicases and nucleic acid translocases. Annual Review of Biochemistry, 76:23–50, 2007.

[97] T. L. Hill and T. Tsuchiya. Theoretical aspects of translocation on DNA: adenosine triphosphatases and treadmilling binding proteins. Proceedings of the National Academy of Sciences of the United States of America, 78(8):4796–4800, 1981.

[98] A. E. Gorbalenya and E. V. Koonin. Helicases: amino acid sequence comparisons and structure-function relationships. Current Opinion in Structural Biology, 3(3):419–429, 1993.

[99] J. Ye, A. R. Osborne, M. Groll, and T. A. Rapoport. RecA-like motor ATPases–lessons from structures. Biochimica et Biophysica Acta (BBA) - Bioenergetics, 1659(1):1–18, 2004.

[100] J. E. Walker, M. Saraste, M. J. Runswick, and N. J. Gay. Distantly related sequences in the alpha-and beta-subunits of ATP synthase, myosin, kinases and other ATP-requiring enzymes and a common nucleotide binding fold. The EMBO Journal, 1(8):945, 1982.

[101] K. Scheffzek, M. R. Ahmadian, W. Kabsch, L. Wiesmuller, A. Lautwein, F. Schmitz, and A. Wittinghofer. The Ras-RasGAP complex: structural basis for GTPase activation and its loss in oncogenic Ras mutants. Science, 277(5324):333–338, 1997.

[102] M. R. Singleton and D. B. Wigley. Modularity and specialization in superfamily 1 and 2 helicases. Journal of Bacteriology, 184(7):1819–1826, 2002.

[103] P. H. von Hippel and E. Delagoutte. A general model for nucleic acid helicases and their “coupling" within macromolecular machines. Cell, 104(2):177–190, 2001.

[104] T. M. Lohman. Helicase-catalyzed DNA unwinding. Journal of Biological Chemistry, 268(4):2269–2272, 1993.

[105] T. M. Lohman. *Escherichia coli* DNA helicases: mechanisms of DNA unwinding. Molecular Microbiology, 6(1):5–14, 1992.

[106] G. Bonnet, O. Krichevsky, and A. Libchaber. Kinetics of conformational fluctuations in DNA hairpin-loops. Proceedings of the National Academy of Sciences of the United States of America, 95(15):8602–8606, 1998.

[107] J. L. Leroy, M. Kochoyan, T. Huynh-Dinh, and M. Guéron. Characterization of base-pair opening in deoxynucleotide duplexes using catalyzed exchange of the imino proton. Journal of Molecular Biology, 200(2):223–238, 1988.

[108] P. Soultanas and D. B. Wigley. Unwinding the ‘Gordian knot’ of helicase action. Trends in Biochemical Sciences, 26(1):47–54, 2001.

[109] M. D. Betterton and F. Jülicher. A motor that makes its own track: Helicase unwinding of DNA. Physical Review Letters, 91(25):258103, 2003.

[110] M. D. Betterton and F. Jülicher. Opening of nucleic-acid double strands by helicases: Active versus passive opening. Physical Review E, 71(1):11904, 2005.

[111] M. Manosas, X. G. Xi, D. Bensimon, and V. Croquette. Active and passive mechanisms of helicases. Nucleic Acids Research, 38(16):5518–5526, 2010.

[112] P. Soultanas, M. S. Dillingham, P. Wiley, M. R. Webb, and D. B. Wigley. Uncoupling DNA translocation and helicase activity in PcrA: Direct evidence for an active mechanism. The EMBO Journal, 19(14):3799–3810, 2000.

[113] K. M. Brendza, W. Cheng, C. J. Fischer, M. A. Chesnik, A. Niedziela-Majka, and T. M. Lohman. Autoinhibition of *Escherichia coli* Rep monomer helicase activity by its 2B subdomain. Proceedings of the National Academy of Sciences of the United States of America, 102(29):10076–10081, 2005.

[114] M. N. Dessinges, T. Lionnet, X. G. Xi, D. Bensimon, and V. Croquette. Single-molecule assay reveals strand switching and enhanced processivity of UvrD. Proceedings of the National Academy of Sciences of the United States of America, 101(17):6439–6444, 2004.

[115] N. K. Maluf, C. J. Fischer, and T. M. Lohman. A dimer of *Escherichia coli* UvrD is the active form of the helicase *in vitro*. Journal of Molecular Biology, 325(5):913–935, 2003.

[116] C. J. Fischer, N. K. Maluf, and T. M. Lohman. Mechanism of ATP-dependent translocation of *E. coli* UvrD monomers along single-stranded DNA. Journal of Molecular Biology, 344(5):1287–1309, 2004.

[117] B. Sun, K. J. Wei, B. Zhang, X. H. Zhang, S. X. Dou, M. Li, and X. G. Xi. Impediment of E. coli UvrD by DNA-destabilizing force reveals a strained-inchworm mechanism of DNA unwinding. The EMBO Journal, 27(24):3279–3287, 2008.

[118] W. Cheng, S. Dumont, I. Tinoco, and C. Bustamante. NS3 helicase actively separates RNA strands and senses sequence barriers ahead of the opening fork. Proceedings of the National Academy of Sciences of the United States of America, 104(35):13954–13959, 2007.

[119] I. Donmez, V. Rajagopal, Y. J. Jeong, and S. S. Patel. Nucleic acid unwinding by hepatitis C virus and bacteriophage T7 helicases is sensitive to base pair stability. Journal of Biological Chemistry, 282(29):21116–21123, 2007.

[120] T. Lionnet, M. M. Spiering, S. J. Benkovic, D. Bensimon, and V. Croquette. Real-time observation of bacteriophage T4 gp41 helicase reveals an unwinding mechanism. Proceedings of the National Academy of Sciences of the United States of America, 104(50):19790–19795, 2007.

[121] G. T. Yarranton and M. L. Gefter. Enzyme-catalyzed DNA unwinding: Studies on *Escherichia coli* rep protein. Proceedings of the National Academy of Sciences of the United States of America, 76(4):1658–1662, 1979.

[122] J. Yu, T. Ha, and K. Schulten. Structure-based model of the stepping motor of PcrA helicase. Biophysical Journal, 91(6):2097–2114, 2006.

[123] I. Wong and T. M. Lohman. Allosteric effects of nucleotide cofactors on *Escherichia coli* Rep helicase–DNA binding. Science, 256(5055):350–355, 1992.

[124] M. Amaratunga and T.M. Lohman. *Escherichia coli* rep helicase unwinds DNA by an active mechanism. Biochemistry, 32(27):6815–6820, 1993.

[125] K. P. Bjornson, I. Wong, and T. M. Lohman. ATP hydrolysis stimulates binding and release of single stranded DNA from alternating subunits of the dimeric E. coli Rep helicase: implications for ATP-driven helicase translocation. Journal of Molecular Biology, 263(3):411–422, 1996.

[126] T. M. Lohman, J. Hsieh, N. K. Maluf, W. Cheng, A. L. Lucius, C. J. Fischer, K. M. Brendza, S. Korolev, and G. Waksman. DNA helicases, motors that move along nucleic acids: lessons from the SF1 helicase superfamily. The Enzymes, 23:303–369, 2003.

[127] S. Korolev, J. Hsieh, G. H. Gauss, T. M. Lohman, and G. Waksman. Major domain swiveling revealed by the crystal structures of complexes of *E. coli* Rep helicase bound to single-stranded DNA and ADP. Cell, 90(4):635–647, 1997.

[128] J. L. Kim, K. A. Morgenstern, J. P. Griffith, M. D. Dwyer, J. A. Thomson, M. A. Murcko, C. Lin, and P. R. Caron. Hepatitis C virus NS3 RNA helicase domain with a bound oligonucleotide: the crystal structure provides insights into the mode of unwinding. Structure, 6(1):89–100, 1998.

[129] M. Machius, L. Henry, M. Palnitkar, and J. Deisenhofer. Crystal structure of the DNA nucleotide excision repair enzyme UvrB from *Thermus thermophilus*. Proceedings of the National Academy of Sciences of the United States of America, 96(21):11717–11722, 1999.

[130] H. S. Subramanya, L. E. Bird, J. A. Brannigan, and D. B. Wigley. Crystal-Structure of a Dexx Box DNA Helicase. Nature, 384(6607):379–383, 1996.

[131] M. R. Singleton, M. S. Dillingham, M. Gaudier, S. C. Kowalczykowski, and D. B. Wigley. Crystal structure of RecBCD enzyme reveals a machine for processing DNA breaks. Nature, 432(7014):187–193, 2004.

[132] M. K. Levin, M. Gurjar, and S. S. Patel. A Brownian motor mechanism of translocation and strand separation by hepatitis C virus helicase. Nature Structural & Molecular Biology, 12(5):429–435, 2005.

[133] S. S. Patel and I. Donmez. Mechanisms of helicases. Journal of Biological Chemistry, 281(27):18265–18268, 2006.

[134] A. M. Pyle. Translocation and unwinding mechanisms of RNA and DNA helicases. Annual Review of Biophysics, 37:317–336, 2008.

[135] M. K. Levin, M. M. Gurjar, and S. S. Patel. ATP binding modulates the nucleic acid affinity of hepatitis C virus helicase. Journal of Biological Chemistry, 278(26):23311–23316, 2003.

[136] P. R. Bianco, L. R. Brewer, M. Corzett, R. Balhorn, Y. Yeh, S. C. Kowalczykowski, and R. J. Baskin. Processive translocation and DNA unwinding by individual RecBCD enzyme molecules. Nature, 409(6818):374–378, 2001.

[137] L. J. Roman and S. C. Kowalczykowski. Characterization of the adenosine triphosphatase activity of the *Escherichia coli* RecBCD enzyme: relationship of ATP hydrolysis to the unwinding of duplex DNA. Biochemistry, 28(7):2873–2881, 1989.

[138] L. J. Roman and S. C. Kowalczykowski. Characterization of the helicase activity of the *Escherichia coli* RecBCD enzyme using a novel helicase assay. Biochemistry, 28(7):2863–2873, 1989.

[139] M. Spies, I. Amitani, R. J. Baskin, and S. C. Kowalczykowski. RecBCD enzyme switches lead motor subunits in response to χ recognition. Cell, 131(4):694–705, 2007.

[140] L. J. Roman, A. K. Eggleston, and S. C. Kowalczykowski. Processivity of the DNA helicase activity of *Escherichia coli* RecBCD enzyme. Journal of Biological Chemistry, 267(6):4207–4214, 1992.

[141] M. S. Dillingham, M. Spies, and S. C. Kowalczykowski. RecBCD enzyme is a bipolar DNA helicase. Nature, 423(6942):893–897, 2003.

[142] M. S. Dillingham, M. R. Webb, and S. C. Kowalczykowski. Bipolar DNA translocation contributes to highly processive DNA unwinding by RecBCD enzyme. Journal of Biological Chemistry, 280(44):37069–37077, 2005.

[143] I. J. Finkelstein, M. L. Visnapuu, and E. C. Greene. Single-molecule imaging reveals mechanisms of protein disruption by a DNA translocase. Nature, 468:983–987, 2010.

[144] M. R. Gabbidon, V. E. Rampersaud, and D. A. Julin. Salt-stable complexes of the *Escherichia coli* RecBCD enzyme bound to double-stranded DNA. Archives of Biochemistry and Biophysics, 350(2):266–272, 1998.

[145] A. F. Taylor and G. R. Smith. Monomeric RecBCD enzyme binds and unwinds DNA. Journal of Biological Chemistry, 270(41):24451–24458, 1995.

[146] F. Korangy and D. A. Julin. Efficiency of ATP hydrolysis and DNA unwinding by the RecBC enzyme from *Escherichia coli*. Biochemistry, 33(32):9552–9560, 1994.

[147] S. K. Amundsen and G. R. Smith. Interchangeable parts of the *Escherichia coli* recombination machinery. Cell, 112(6):741–744, 2003.

[148] A. K. Eggleston and S. C. West. Recombination initiation: Easy as A, B, C, D... χ? Current Biology, 7(12):R745–R749, 1997.

[149] S. C. Kowalczykowski. Initiation of genetic recombination and recombination-dependent replication. Trends in Biochemical Sciences, 25(4):156–165, 2000.

[150] R. S. Myers, M. M. Stahl, and F. W. Stahl. χ recombination activity in phage λ decays as a function of genetic distance. Genetics, 141(3):805–812, 1995.

[151] G. R. Smith. Homologous recombination near and far from DNA breaks: alternative roles and contrasting views. Genetics, 35(1):243–274, 2001.

[152] M. Spies and S. C. Kowalczykowski. Homologous recombination by RecBCD and RecF pathways. In N. P. Higgins, editor, The bacterial chromosome, pages 389–403, Washington, DC, 2005. ASM Press.

[153] A. F. Taylor. The RecBCD enzyme of *Escherichia coli*. In R. Kucherlapati and G. R. Smith, editors, Genetic recombination, pages 231–263, Washington, D.C., 1988. American Society for Microbiology.

[154] T. Kogoma. Stable DNA replication: interplay between DNA replication, homologous recombination, and transcription. Microbiology and Molecular Biology Reviews, 61(2):212–238, 1997.

[155] A. Kuzminov. Collapse and repair of replication forks in Escherichia coli. Molecular Microbiology, 16(3):373–384, 1995.

[156] M. M. Cox and I. R. Lehman. RecA protein of Escherichia coli promotes branch migration, a kinetically distinct phase of DNA strand exchange. Proceedings of the National Academy of Sciences of the United States of America, 78(6):3433–3437, 1981.

[157] T. Shibata, C. DasGupta, R. P. Cunningham, and C. M. Radding. Purified *Escherichia coli* recA protein catalyzes homologous pairing of superhelical DNA and single-stranded fragments. Proceedings of the National Academy of Sciences of the United States of America, 76(4):1638–1642, 1979.

[158] R. Galletto and S. C. Kowalczykowski. RecA. Current Biology, 17(11):R395–R397, 2007.

[159] S. C. Kowalczykowski, D. A. Dixon, A. K. Eggleston, S. D. Lauder, and W. M. Rehrauer. Biochemistry of homologous recombination in *Escherichia coli*. Microbiology and Molecular Biology Reviews, 58(3):401–465, 1994.

[160] G. R. Smith. Conjugational recombination in *E. coli*: Myths and mechanisms. Cell, 64(1):19–27, 1991.

[161] R. C. Heller and K. J. Marians. Replisome assembly and the direct restart of stalled replication forks. Nature Reviews Molecular Cell Biology, 7(12):932–943, 2006.

[162] A. J. Clark and S. J. Sandler. Homologous genetic recombination: the pieces begin to fall into place. Critical Reviews in Microbiology, 20(2):125–142, 1994.

[163] A. Kuzminov. Recombinational repair of DNA damage in *Escherichia coli* and bacteriophage λ. Microbiology and Molecular Biology Reviews, 63(4):751–813, 1999.

[164] D. Henderson and J. Weil. The nature and origin of a class of essential gene substitutions in bacteriophage λ. Virology, 67(1):124–135, 1975.

[165] S. T. Lam, M. M. Stahl, K. D. McMilin, and F. W. Stahl. Rec-mediated recombinational hot spot activity in bacteriophage lambda. II. A mutation which causes hot spot activity. Genetics, 77(3):425–433, 1974.

[166] P. R. Bianco and S. C. Kowalczykowski. The recombination hotspot Chi is recognized by the translocating RecBCD enzyme as the single strand of DNA containing the sequence 5′-GCTGGTGG-3′. Proceedings of the National Academy of Sciences of the United States of America, 94(13):6706–6711, 1997.

[167] K. U. Sprague, D. H. Faulds, and G. R. Smith. A single base-pair change creates a Chi recombinational hotspot in bacteriophage λ. Proceedings of the National Academy of Sciences of the United States of America, 75(12):6182–6186, 1978.

[168] G. R. Smith, S. M. Kunes, D. W. Schultz, A. Taylor, and K. L. Triman. Structure of Chi hotspots of generalized recombination. Cell, 24(2):429–436, 1981.

[169] I. D. Hickson, C. N. Robson, K. E. Atkinson, L. Hutton, and P. T. Emmerson. Reconstitution of RecBC DNase activity from purified *Escherichia coli* RecB and RecC proteins. Journal of Biological Chemistry, 260(2):1224–1229, 1985.

[170] P. E. Boehmer and P. T. Emmerson. The RecB subunit of the *Escherichia coli* RecBCD enzyme couples ATP hydrolysis to DNA unwinding. Journal of Biological Chemistry, 267(7):4981–4987, 1992.

[171] J. Z. Sun, D. A. Julin, and J. S. Hu. The nuclease domain of the *Escherichia coli* RecBCD enzyme catalyzes degradation of linear and circular single-stranded and double-stranded DNA. Biochemistry, 45(1):131–140, 2006.

[172] J. Wang, R. Chen, and D. A. Julin. A single nuclease active site of the *Escherichia coli* RecBCD enzyme catalyzes single-stranded DNA degradation in both directions. Journal of Biological Chemistry, 275(1):507–513, 2000.

[173] M. Yu, J. Souaya, and D. A. Julin. Identification of the nuclease active site in the multifunctional RecBCD enzyme by creation of a chimeric enzyme. Journal of Molecular Biology, 283(4):797–808, 1998.

[174] M. Yu, J. Souaya, and D. A. Julin. The 30-kDa C-terminal domain of the RecB protein is critical for the nuclease activity, but not the helicase activity, of the RecBCD enzyme from *Escherichia coli*. Proceedings of the National Academy of Sciences of the United States of America, 95(3):981–986, 1998.

[175] D. G. Anderson, J. J. Churchill, and S. C. Kowalczykowski. A single mutation, $\mathrm{RecB_{D1080A}}$, eliminates RecA protein loading but not Chi recognition by RecBCD enzyme. Journal of Biological Chemistry, 274(38):27139–27144, 1999.

[176] D. G. Anderson and S. C. Kowalczykowski. The translocating RecBCD enzyme stimulates recombination by directing RecA protein onto ssDNA in a χ-regulated manner. Cell, 90(1):77–86, 1997.

[177] L. N. Kinch, K. Ginalski, L. Rychlewski, and N. V. Grishin. Identification of novel restriction endonuclease-like fold families among hypothetical proteins. Nucleic Acids Research, 33(11):3598–3605, 2005.

[178] D. A. Arnold, N. Handa, I. Kobayashi, and S. C. Kowalczykowski. A novel, 11 nucleotide variant of χ, χ^*: one of a class of sequences defining the *Escherichia coli* recombination hotspot χ. Journal of Molecular Biology, 300(3):469–479, 2000.

[179] N. Handa, S. Ohashi, K. Kusano, and I. Kobayashi. χ^*, a χ-related 11-mer sequence partially active in an *E. coli recC** strain. Genes to cells, 2(8):525–536, 1997.

[180] H. W. Chen, B. Ruan, M. Yu, J. Wang, and D. A. Julin. The RecD subunit of the RecBCD enzyme from *Escherichia coli* is a single-stranded DNA-dependent ATPase. Journal of Biological Chemistry, 272(15):10072–10079, 1997.

[181] A. F. Taylor and G. R. Smith. RecBCD enzyme is a DNA helicase with fast and slow motors of opposite polarity. Nature, 423(6942):889–893, 2003.

[182] H. F. Fan and H. W. Li. Studying RecBCD helicase translocation along χ-DNA using tethered particle motion with a stretching force. Biophysical Journal, 96(5):1875–1883, 2009.

[183] N. Handa, P. R. Bianco, R. J. Baskin, and S. C. Kowalczykowski. Direct visualization of RecBCD movement reveals cotranslocation of the RecD motor after χ recognition. Molecular Cell, 17(5):745–750, 2005.

[184] M. Spies, P. R. Bianco, M. S. Dillingham, N. Handa, R. J. Baskin, and S. C. Kowalczykowski. A molecular throttle: The recombination hotspot χ controls DNA translocation by the RecBCD helicase. Cell, 114(5):647–654, 2003.

[185] A. L. Lucius, A. Vindigni, R. Gregorian, J. A. Ali, A. F. Taylor, G. R. Smith, and T. M. Lohman. DNA unwinding step-size of *E. coli* RecBCD helicase determined from single turnover chemical quenched-flow kinetic studies. Journal of Molecular Biology, 324(3):409–428, 2002.

[186] J. A. Ali and T. M. Lohman. Kinetic measurement of the step size of DNA unwinding by *Escherichia coli* UvrD helicase. Science, 275(5298):377–380, 1997.

[187] A. R. Carter, M. Hosotani, A. M. Noronha, C. J. Wilds, H. F. Fan, H. W. Li, and T. T. Perkins. Nanometer-scale conformational dynamics of RecBCD along DNA. In preparation, 2011.

[188] J. W. J. Kerssemakers, E. L. Munteanu, L. Laan, T. L. Noetzel, M. E. Janson, and M. Dogterom. Assembly dynamics of microtubules at molecular resolution. Nature, 442(7103):709–712, 2006.

[189] J. A. Farah and G. R. Smith. The RecBCD enzyme initiation complex for DNA unwinding: Enzyme positioning and DNA opening. Journal of Molecular Biology, 272(5):699–715, 1997.

[190] C. J. Wong, A. L. Lucius, and T. M. Lohman. Energetics of DNA end binding by *E. coli* RecBC and RecBCD helicases indicate loop formation in the 3′-single-stranded DNA tail. Journal of Molecular Biology, 352(4):765–782, 2005.

[191] K. Saikrishnan, S. P. Griffiths, N. Cook, R. Court, and D. B. Wigley. DNA binding to RecD: Role of the 1B domain in SF1B helicase activity. The EMBO Journal, 27(16):2222–2229, 2008.

[192] P. D. Coureux, H. L. Sweeney, and A. Houdusse. Three myosin V structures delineate essential features of chemo-mechanical transduction. The EMBO Journal, 23:4527–4537, 2004.

[193] A. J. Fisher, C. A. Smith, J. B. Thoden, R. Smith, K. Sutoh, H. M. Holden, and I. Rayment. X-ray structures of the myosin motor domain of *Dictyostelium discoideum* complexed with MgADP·BeF_x and MgADP·AlF_4. Biochemistry, 34(28):8960–8972, 1995.

[194] A. M. Gulick, C. B. Bauer, J. B. Thoden, and I. Rayment. X-ray structures of the MgADP, MgATPγS, and MgAMPPNP complexes of the *Dictyostelium discoideum* myosin motor domain. Biochemistry, 36(39):11619–11628, 1997.

[195] C. J. Wilds, A. M. Noronha, S. Robidoux, and P. S. Miller. Mispair-aligned N^3T-alkyl-N^3T interstrand cross-linked DNA: Synthesis and characterization of duplexes with interstrand cross-links of variable lengths. Journal of the American Chemical Society, 126(30):9257–9265, 2004.

[196] M. W. da Silva, R. G. Bierbryer, C. J. Wilds, A. M. Noronha, O. M. Colvin, P. S. Miller, and M. P. Gamcsik. Intrastrand base-stacking buttresses widening of major groove in interstrand cross-linked B-DNA. Bioorganic & Medicinal Chemistry, 13(14):4580–4587, 2005.

[197] J. A. Doudna and T. R. Cech. The chemical repertoire of natural ribozymes. Nature, 418(6894):222–228, 2002.

[198] W. Gilbert. Evolution of antibodies: the road not taken. Nature, 320(6062):485–486, 1986.

[199] X. Chen, N. Li, and A. D. Ellington. Ribozyme catalysis of metabolism in the RNA world. Chemistry & Biodiversity, 4(4):633–655, 2007.

[200] A. D. Ellington, X. Chen, M. Robertson, and A. Syrett. Evolutionary origins and directed evolution of RNA. The International Journal of Biochemistry & Cell Biology, 41(2):254–265, 2009.

[201] A. D. Ellington and J. W. Szostak. *In vitro* selection of RNA molecules that bind specific ligands. Nature, 346(6287):818–822, 1990.

[202] C. Tuerk and L. Gold. Systematic evolution of ligands by exponential enrichment: RNA ligands to bacteriophage T4 DNA polymerase. Science, 249(4968):505–505, 1990.

[203] T. Hermann. Chemical and functional diversity of small molecule ligands for RNA. Biopolymers, 70(1):4–18, 2003.

[204] R. D. Jenison, S. C. Gill, A. Pardi, and B. Polisky. High-resolution molecular discrimination by RNA. Science, 263(5152):1425–1429, 1994.

[205] W. C. Winkler and R. R. Breaker. Regulation of bacterial gene expression by riboswitches. Microbiology, 59:487–517, 2005.

[206] A. Roth and R. R. Breaker. The structural and functional diversity of metabolite-binding riboswitches. Annual Review of Biochemistry, 78:305–334, 2009.

[207] A. D. Garst and R. T. Batey. A switch in time: Detailing the life of a riboswitch. Biochimica et Biophysica Acta (BBA) - Gene Regulatory Mechanisms, 1789(9-10):584–591, 2009.

[208] D. A. Rodionov, A. G. Vitreschak, A. A. Mironov, and M. S. Gelfand. Comparative genomics of thiamin biosynthesis in procaryotes. New genes and regulatory mechanisms. Journal of Biological Chemistry, 277(50):48949–48959, 2002.

[209] M. Mandal, B. Boese, J. E. Barrick, W. C. Winkler, and R. R. Breaker. Riboswitches control fundamental biochemical pathways in Bacillus subtilis and other bacteria. Cell, 113(5):577–586, 2003.

[210] J. E. Barrick, K. A. Corbino, W. C. Winkler, A. Nahvi, M. Mandal, J. Collins, M. Lee, A. Roth, N. Sudarsan, I. Jona, J. K. Wickiser, and R. R. Breaker. New RNA motifs suggest an expanded scope for riboswitches in bacterial genetic control. Proceedings of the National Academy of Sciences of the United States of America, 101(17):6421–6426, 2004.

[211] A. G. Vitreschak, D. A. Rodionov, A. A. Mironov, and M. S. Gelfand. Regulation of the vitamin B12 metabolism and transport in bacteria by a conserved RNA structural element. RNA, 9(9):1084–1097, 2003.

[212] S. Milewski. Glucosamine-6-phosphate synthase–the multi-facets enzyme. Biochimica et Biophysica Acta (BBA) - Protein Structure and Molecular Enzymology, 1597(2):173–192, 2002.

[213] D. J. Klein and A. R. Ferre-D'Amare. Structural basis of glmS ribozyme activation by glucosamine-6-phosphate. Science, 313(5794):1752–1756, 2006.

[214] J. C. Cochrane, S. V. Lipchock, and S. A. Strobel. Structural investigation of the GlmS ribozyme bound to its catalytic cofactor. Chemistry & Biology, 14(1):97–105, 2007.

[215] D. J. Klein, S. R. Wilkinson, M. D. Been, and A. R. Ferré-D'Amaré. Requirement of helix P2. 2 and nucleotide G1 for positioning the cleavage site and cofactor of the glmS ribozyme. Journal of Molecular Biology, 373(1):178–189, 2007.

[216] J. C. Cochrane, S. V. Lipchock, K. D. Smith, and S. A. Strobel. Structural and chemical basis for glucosamine 6-phosphate binding and activation of the *glmS* ribozyme. Biochemistry, 48(15):3239–3246, 2009.

[217] S. R. Wilkinson and M. D. Been. A pseudoknot in the 3′ non-core region of the *glmS* ribozyme enhances self-cleavage activity. RNA, 11(12):1788–1794, 2005.

[218] A. Roth, A. Nahvi, M. Lee, I. Jona, and R. R. Breaker. Characteristics of the *glmS* ribozyme suggest only structural roles for divalent metal ions. RNA, 12(4):607–619, 2006.

[219] K. J. Hampel and M. M. Tinsley. Evidence for preorganization of the *glmS* ribozyme ligand binding pocket. Biochemistry, 45(25):7861–7871, 2006.

[220] R. A. Tinsley, J. R. W. Furchak, and N. G. Walter. Trans-acting *glmS* catalytic riboswitch: Locked and loaded. RNA, 13(4):468–477, 2007.

[221] M. Martick, L. H. Horan, H. F. Noller, and W. G. Scott. A discontinuous hammerhead ribozyme embedded in a mammalian messenger RNA. Nature, 454(7206):899–902, 2008.

[222] W. G. Scott, M. Martick, and Y. I. Chi. Structure and function of regulatory RNA elements: Ribozymes that regulate gene expression. Biochimica et Biophysica Acta (BBA) - Gene Regulatory Mechanisms, 1789(9-10):634–641, 2009.

[223] M. Liss, B. Petersen, H. Wolf, and E. Prohaska. An aptamer-based quartz crystal protein biosensor. Analytical Chemistry, 74(17):4488–4495, 2002.

[224] E. N. Brody, L. Gold, R. M. Lawn, J. J. Walker, and D. Zichi. High-content affinity-based proteomics: unlocking protein biomarker discovery. Expert Review of Molecular Diagnostics, 10(8):1013–1022, 2010.

[225] K. Stadtherr, H. Wolf, and P. Lindner. An aptamer-based protein biochip. Analytical Chemistry, 77(11):3437–3443, 2005.

[226] E. Ehrentreich-Förster, D. Orgel, A. Krause-Griep, B. Cech, V. A. Erdmann, F. Bier, F. W. Scheller, and M. Rimmele. Biosensor-based on-site explosives detection using aptamers as recognition elements. Analytical and Bioanalytical Chemistry, 391(5):1793–1800, 2008.

[227] T. J. McCarthy, M. A. Plog, S. A. Floy, J. A. Jansen, J. K. Soukup, and G. A. Soukup. Ligand requirements for *glmS* ribozyme self-cleavage. Chemistry & Biology, 12(11):1221–1226, 2005.

[228] T. Ha. Single-molecule fluorescence resonance energy transfer. Methods, 25(1):78–86, 2001.

[229] K. H. Link, L. Guo, and R. R. Breaker. Examination of the structural and functional versatility of glmS ribozymes by using in vitro selection. Nucleic Acids Research, 34(17):4968–4975, 2006.

[230] J. E. Cronan Jr and K. E. Reed. Biotinylation of proteins in vivo: A useful posttranslational modification for protein analysis. Methods in Enzymology, 326:440–458, 2000.

[231] C. G. Wu, C. Bradford, and T. M. Lohman. *Escherichia coli* RecBC helicase has two translocase activities controlled by a single ATPase motor. Nature Structural & Molecular Biology, 17(10):1210–1217, 2010.

Appendix A

Protocols

A.1 RecBCD Tethered-Bead Assay

The following protocol was used to tether beads to a coverslip surface via a dsDNA molecule bound to a biotinylated RecBCD molecule attached to the coverslip.

RecBCD-Biotin Assay: Streptavidin-coated surface, Streptavidin-coated beads

The following buffer was used:

10 mL Wash Buffer (WB)

To a new 15 mL falcon tube add:

8.45 mL ddH_2O	final concentration:
250 µL 2 M TRIS, pH = 7.5	25 mM
10 µL 1M Mg(OAc)2	1 mM
10 µL 1M NaCl	1 mM
400 µL 10% Tween-20	0.4%
870 µL 35 mg/mL BSA (filtered)*	3 mg/mL
10 µL 1M DTT	1 mM

*To make 10 mL 35 mg/mL BSA:

9.4 mL ddH_2O

200 µL 1 M Tris-Cl

400 μL 10% Tween-20

350 mg BSA

To filter, take two 500 μL aliquots of 35 mg/mL BSA solution and put in 0.22 um Millipore filter tubes. Centrifuge at half-speed for 5 min. Remove the filter and take 435 μL out of each tube and put into falcon tube.

(1) Make slides and allow epoxy to dry.

(2) *Be concurrently preparing beads/DNA.*

(3) Dilute 200 μL of 125 μg/mL bio-BSA solution (enough for 10 slides).

195 μL 100 mM Na-Phos pH = 7

5 μL of 5 mg/mL solution

(4) Flow 20 μL per slide of 125 μg/mL Bio-BSA solution through slides.

– Sit for 20 min. in humidity chamber at room temp.

(5) Wash 2 times per slide with 200 μL WB.

– Sit for 10 min.

(6) Make 300 μL of 10 μg/mL Streptavidin (SA) (enough for 6 slides).

297 μL WB

3 μL of 1 mg/mL SA

(7) Flow 50 μL per slide of 10 μg/mL SA.

– Sit for 20 min in humidity chamber at room temp.

(8) Wash 2 times per slide with 200 μL of WB.

– Sit for 10 min.

(9) Make 40 μL of 15 nM RecBCD-bio (usually 0.45 μL of 10 μM or 34 μM RecBCD in 500 μL of WB).

(10) Flow 20 μL 15 nM RecBCD-bio.

– Sit for 2 hours in humidity chamber at room temp.

(11) Wash 2 times with 200 μL of WB.

– Sit for 10 min.

(12) Flow 30 μL of beads/DNA per slide.

– Sit for 60 min in humidity chamber at room temp.

(13) Wash 2 times with 200 μL of WB.

– Sit for 10 min.

(14) View under microscope.

(15) Add 50 μL of ATP-SSB solution to slide for RecBCD to unwind the DNA.

81.4 μL WB	
10 μL 100 μM ATP	10 μM ATP
8.6 μL 12.8 μM SSB	1.1 μM SSB

SA beads/DNA

(1) Briefly vortex bead stock.

(2) Add 30 μL of 408 pM SA bead stock (for 440-nm diameter, 920 pM for 320-nm diameter) per 2 slides.

(3) Wash beads three times. Add 200 μL 0.4% Phos-Tween, centrifuge (5 min, 10 krpm, 400 nm bead) (7krpm, 500 nm bead, 5 min) (12 krpm, 320 nm bead, 5 min), and remove supernatant.

(4) Resuspend in 30 μL of WB (30 μL of 408 pM beads).

(5) Sonicate beads.

   (a) Parafilm the tube before sonicating.

   (b) 4 °C temperature

   (c) 8 min pulse mode (2 s on, 2 s off)

(6) Check beads for monodispersion.

   (a) Dilute 1 μL of beads in 100 μL of WB.

   (b) Flow through a slide and check under microscope.

(7) Make 30 μL of 100 pM DNA per two slides.

(8) If two dilutions are necessary, 1st dilution should be in 10mM Tris-Cl (This dilution can be kept and used for weeks.)

(9) For 2nd dilution, dilute into WB. This solution can be used for ~1 week.

(10) Mix 408 pM beads with 100 pM DNA, makes 204 pM beads and 50 pM DNA

(11) Mix by pipetting.

(12) Sit for 60 min at room temperature.

A.2 *glmS* Ribozyme Tethered-Bead Assay

glmS Tethered-Bead Assay: Streptavidin-coated surface, Antidigoxigenin-coated beads

The following buffer was used:

10 mL Yeonee Buffer (YB) with Tween-20

To a new 15 mL falcon tube add:

7.625 mL DEPC-treated dH_2O (RNase-free)	Final concentration:
100 µL 1 M HEPES pH 7.5	10 mM
1500 µL 1 M KCl	150 mM
400 µL 10% Tween-20	0.4%
375 µL 80 mg/mL acetylated BSA*	3 mg/mL

YB and BSA solution is only good for 1 week at 4 °C. Need at least 2.58 mL YB per 2 slides.

(1) Make slides and allow epoxy to dry.

(2) Be concurrently preparing beads and RNA:DNA while completing steps 3-8.

(3) Make 100 µL (per 2 slides) of 125 µg/mL Biotin BSA solution. Mix by vortexing:

97.5 µL of 100 mM Phosphate buffer (JUST Phos, no Tween!)

2.5 µL of 5 mg/mL biotinylated BSA

(4) Flow 50 µL per slide of 125 µg/mL Biotin BSA solution

–Let sit for 20 min in humidity chamber at room temperature.

(5) Wash slides 2x w/200 µL YB.

–Let sit for 10 min at room temperature.

(6) Make 100 µL (per 2 slides) of 10 µg/mL SA solution. Mix by vortexing:

99 µL of YB

1 μL of 1 mg/mL SA

(7) Flow 50 μL per slide of 10 μg/mL SA solution

–Let sit for 10 min in humidity chamber at room temperature.

(8) Wash slides 2x w/200 μL YB.

–Let sit for 10 min at 4 °C.

Bead-RNA:DNA preparation

(1) Prepare 40 μL 375 pM AD beads per 2 slides.

(a) Briefly vortex AD bead stock.

(b) To an epindorph tube, add enough beads to be 375 pM when diluted in 40 μL per 2 slides.

17.24 μL of 870 pM 180 nm beads per 2 slides

(c) Bring up to 200 μL in Phos-Tween buffer (0.4%),

(d) Centrifuge for 7 min at 14 krpm and remove supernatant.

(e) Resuspend beads in 200 μL Phos-Tween, centrifuge 7 min, remove supernatant.

(f) Resuspend in 40 μL YB.

(g) Sonicate 10 min total.

(h) Check under microscope for monodispersion.

(2) Make 40 μL 75 pM DNA per two slides.

(a) If two dilutions are necessary, 1st dilution should be in 10 mM Tris Cl (This dilution can be kept and used for weeks.)

(b) For 2nd dilution, dilute into YB. This solution can be used for ~1 week. 3 μL of 1 nM DNA + 37 μL YB + 2 μL SUPERase

(3) Add DNA to bead solution.

40 μL of the 375 pM bead solution per two slides

40 μL of the 75 pM DNA solution per two slides

(a) Mix by pipetting quickly 10x, then vortexing for 30 s on medium (5).

(b) Let sit 20 min at 4 °C.

(4) Flow 30 μL of bead-DNA solution through each slide.

–Let sit 20 min. at 4 °C.

(5) Wash slides 2x w/200 μL YB.

(6) Wash slides 2x w/200 μL No Ligand Buffer.

Appendix B

Alignment and Calibrations

B.1 Optical-Trapping Instrument

Calibrations of the precision optical-trapping instrument requires a series of steps. Most of these steps can be done using a polystyrene bead with diameter $d = 400$ nm. A free bead refers to a bead in solution, usually an uncoated polystyrene particle in water. A stuck bead refers to a bead that is stuck to a glass coverslip, typically using a buffer with high magnesium concentration followed by a bake [87].

(1) *Coarse optical alignment.*

Check that the laser beams are level, not clipping on any optics, and parallel to the screw holes in the optical table. Lenses and detectors should be aligned to the optical axis of the laser. Fiber coupling of the laser into the fiber should be adjusted such that the output from the AOM is imaged onto the angle-cleaved fiber tip.

(2) *Optimize trap laser collimation.*

Set the focal point of the trapping laser ($\lambda = 1064$ nm) to the optimal position relative to the objective lens such that it keeps a trapped free bead at a constant axial position when lowering the stage position. To do this, translate the 2^{nd} lens after the fiber output in the axial direction, and translate the output end of the fiber in the axial direction. Measure the 1064 sum signal ($V_{1064,\text{sum}}$) of a trapped free bead versus stage position (z_{stage}), scanning from when the bead leaves the surface to when z_{stage} is several microns away (Figure 2.8).

LabVIEW: C:\Users\Perkins\Labview \JILA\DriftofFreeBead_ASH052510.vi
(subVI: C:\Users\Perkins\Labview\JILA\height JILA 2bm DAQ.vi)

IGOR: Load general text (e.g., free223314.hg1) saved by the height program (height JILA 2bm DAQ.vi).

Examples: 052610.pxp MH #6 p.126, 061906 ARC #11 p.55

(3) *Optimize the position of the bead detection laser focus.*

Repeat steps as described in step 2, but using signals for the bead detection laser ($\lambda = 785$ nm) (Figure 2.8). First perform a coarse adjustment by making the image of the detection laser focus on the CCD camera in the same image plane as the trapped bead. Measure the 785 sum signal ($V_{785,\mathrm{sum}}$) of a trapped free bead versus stage position (z_{stage}), scanning from when the bead leaves the surface to when z_{stage} is several microns away. Then translate the 2^{nd} lens after the fiber output in the axial direction, and translate the output end of the fiber in the axial direction to "flatten" the bead position signal such that it stays constant as z_{stage} increases.

(4) *Position CCD camera in a plane conjugate to the trapping plane.*

Determine z position at which a trapped bead leaves the coverslip surface by overlaying a 785 z scan of a free bead with that of a stuck bead (e.g., surface-to-peak ~340 nm). Set the CCD camera position to be at the image plane of when a stuck bead is at that position (Figure 2.7).

Examples: 052710.pxp MH #6 p.127

(5) *Position the focus of the fiducial mark detection laser.*

Determine the trap position using the aligned 785 sum signal off a stuck bead. Measure the sum signal off the bead with the stage detection laser ($\lambda = 850$ nm). Move the 850 nm 2^{nd} lens and fiber tip axially to optimize the 850 nm position of the focus (e.g., to be in line with the 785 focus, or, in the case of the RecBCD assay, to be 300 nm below the trapping

plane).

(6) *Minimize crosstalk of all lasers.*

Measure the V_{x}, V_{y}, and V_{z} voltage signals of a stuck bead when moving the stage in x, y, and z. Minimize the crosstalk (i.e., minimize V_{x} versus y_{stage}, V_{y} versus x_{stage}, V_{x} versus z_{stage}, and V_{y} versus z_{stage}). To minimize crosstalk, adjust the lateral position of the fiber output with the 3D-translation stage upon which it is mounted.

(7) *Calibrate the PZT mirrors.*

Calibrate the 1064 and 850 PZT mirrors. Each PZT mirror can be rotated by orienting the mirror to different screw holes in its gimbal mount.

LabVIEW: C:\Users\Perkins\Labview\JILA\Calibration Routines
\CalibratePZTMirrorUsingStageAndStuckBead.vi
C:\Users\Perkins\Labview\JILA\Calibration Routines
\CheckCalibratePZTMirrorUsingStageAndStuckBead.vi

(8) *Measure the pointing stability between the detection lasers.*

Measure the differential signal between 785/850 (e.g., $(V_{785,\mathrm{x}} - V_{850,\mathrm{x}})$ versus time) to measure the relative pointing stability between the 785 and 850 detection lasers. The average standard deviation should be (0.05 nm, 0.05 nm) in (x, y) for 1-10 Hz (average 10 sec) (Figure 2.12A).

LabVIEW: C:\Users\Perkins\Labview\Z calibration\ZCal_2_Beams_1 bead_Rezero.vi

IGOR: Load general text (e.g., ReZero173259.dat). Run AnalyzeRezero.ipf (but do not decimate, just smooth data) and StdDev1s.ipf.

Examples: 060410 stability.pxp MH #6 p.135, 080806 ARC #11 p.116

(9) *Measure stability with active stage stabilization.*

Measure 785 when stabilizing with 850 for stage position lock. Use DAQ rate 10.4 kHz,

average 104 points (average to 100 Hz), set anti-alias filter to 2 kHz. When setting up, center the 785 on a stuck bead ($d \sim 400$ nm) with StageDrift_1_Beam_Multi.vi and center the 850 on the same bead with BeamAlignment.vi (PZT 850, detector beam 850) after setting the 850 PZT mirror to (5 V, 5 V). In ZCal2BeamStageStream_Rezero.vi, enable stabilization (hit ReZero enabled button) and turn on position clamps in x, y, and z (click those 3 buttons). Observe 785 signals. Want 0.1-10 Hz standard deviation of (~0.1 nm, ~0.1 nm, ~0.1 nm) in (x, y, z). For optimal stabilization, servo the 785 and 850 both at -9 V (although 785 servo is typically -3 V).

LabVIEW: C:\Users\Perkins\Labview\Z calibration\ZCal_2_Beams_1 bead_Rezero.vi
C:\Users\Perkins\Labview\JILA\StageDrift\StageDrift_1_Beam_Multi.vi
C:\Users\Perkins\Labview\JILA\BeamAlignment.vi

IGOR: Load general text (e.g. ReZero173259.dat). Run AnalyzeRezero.ipf and StdDev1s.ipf.

Examples: 060410 stability.pxp MH #6 p.137, 080806 ARC #11 p.116

(10) *Measure pointing stability between the trap and bead detection lasers.*

Measure the differential signal between the 785 and 1064 lasers, as done for the 785 and 850 lasers in step 8 (Figure 2.12B).

LabVIEW: C:\Users\Perkins\Labview\Z calibration\ZCal_2_Beams_1 bead_Rezero.vi

IGOR: Load general text (e.g. ReZero173259.dat). Run AnalyzeRezero.ipf and StdDev1s.ipf.

Example: 060410 stability.pxp

(11) *Measure trap ellipticity.*

Measure the position of a bead in a trap and plot the y position versus x position. Fit the data to a line. The slope should be <0.01.

LabVIEW: C:\Users\Perkins\Labview\JILA\Yeonee\StiffnessCalbyPF&EQP.vi

Plot with C:\Users\Perkins\Labview\JILA\Yeonee\2DHistogram.vi

IGOR: Load binary data.

Examples: 040310 ellipticity.pxp MH #6 p.138

(12) *Calibrate trap stiffness versus servo voltage.*

Use 400 nm uncoated bead to measure trap stiffness using the power spectrum and equipartition methods. They should agree to within 10%. Check the calibration with 3 beads. The error should be within 10%. Typical r200stiff-to-volt values were (96, -.04, 49, -.04).

LabVIEW: C:\Users\Amanda\Labview\Calibrations\Stiffness Calibrations
\Pow vs Stiff_PSandEQP_ PositonLockOpt_AECv5_mh.vi
(check for Servo 1-9 V)

C:\Users\Perkins\Labview\JILA\Calibration Routines\StiffnessCalCheck.vi

IGOR: Run plot_ktrap.ipf (loads and plots data from .kvV file or .pve file) and AnalyzeStiffCheck.ipf.

(13) *Measure trap stiffness versus height.*

The trap stiffness should only decrease by 15% 1 μm above the surface.

LabVIEW: C:\Users\Perkins\Labview\JILA\Yeonee\StiffnessCalbyPF&EQP.vi (checks one voltage)

Example: 040506 ARC #11 p.9, 060510 MH #6 p.140

(14) *Check 785 sensitivity versus z of trapped bead.*

(15) *Calibrate trap stiffness versus voltage using PS, EQP, and drag.*

Vary voltage from 1 V to 9 V.

(16) *Check linearity of trap.*

Use drag to measure the trap linearity of the force versus displacement of a free bead. This

program moves the stage at varying velocity to drag a free bead out of the trap. Measure the slope of the sample (dz/dx and dz/dy). Settings: 800 μm/s, number of increments 30, ~100 ms time.

LabVIEW: C:\Users\Perkins\Labview\calibrate_free_bead.vi

(17) *Check stiffness for 320 SA beads.*

Should get r160stiff-to-volt values of (110, 0, 46, 0).

(18) *Check DNA tethers for good L_0, L_p, F_{offset}.*

Use 2 μm DNA, 400 nm beads (AD coated) with bio-BSA/SA surface.

LabVIEW: C:\Users\Perkins\Labview\JILA\DNA stretching\DNA_stretching.llb
\DNA_stretching.vi

IGOR: Procedure_GetExtensionandForce.ipf, ModifiedMarkoSiggitFit.ipf

Example: 060710.pxp

(19) *Optimize 1064 fiber coupling.*

See ARC thesis (Appendix E.11 "How to guide: fiber alignment"). Optimize at $V_{1064,AOM} = 0.6$ V. Get >7.25 V on PD.

(20) *Check 1064 Power versus servo voltage.*

Measure the power of the 1064 laser for 1064 servo voltage 1-9 V and fit to a line. Should get 76 mW/Volt. Use large power head meter set right before beam enters microscope, but make sure sensor is not at the focus of the telescope lens.

Example: 061210.pxp

(21) *Measure free bead versus time.*

LabVIEW: C:\Users\Perkins\Labview\JILA\freebead meas\Measure freebead with steps.vi

IGOR: AnalyzeFreeBead.ipf

(22) *Measure stability of a DNA tether, L versus time.*

LabVIEW: C:\Users\Perkins\Labview\JILA\RecBCD\RecBCDPulling_v1.llb
\RecBCDPulling_v1.vi

Appendix C

Data

The data of individual molecules often contain some level of heterogeneity. For that reason, the individual records of RecBCD bound to DNA are included here.

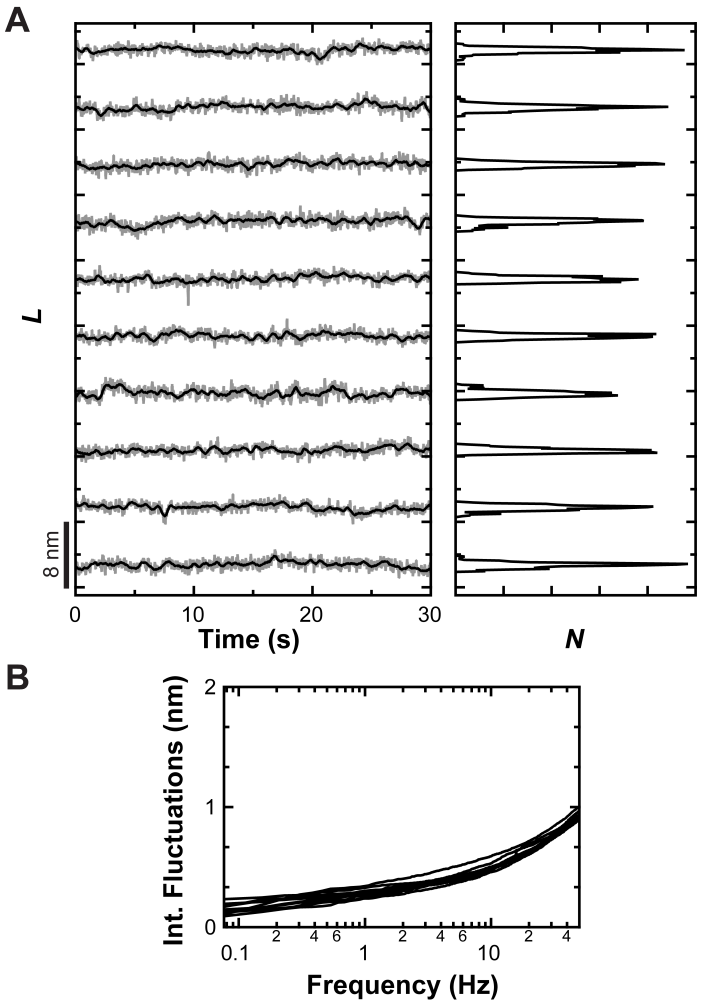

Figure C.1: DNA tethers. (A) DNA contour length versus time with corresponding histograms. Data were taken at $F = 6$ pN and smoothed with a Savitzky-Golay window to 10 Hz (*grey*) and 1 Hz (*black*). (B) Integrated fluctuations of the records in A.

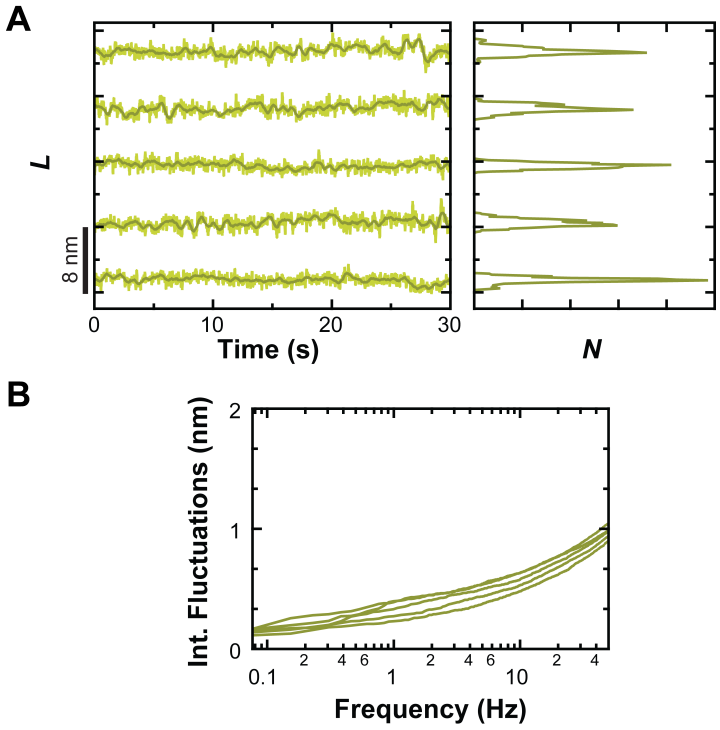

Figure C.2: 5′-$(dT)_{10}$-tailed DNA tethers. (A) DNA contour length versus time with corresponding histograms. Data were taken at $F = 6$ pN and smoothed with a Savitzky-Golay window to 10 Hz (*yellow*) and 1 Hz (*olive*). (B) Integrated fluctuations of the records in A.

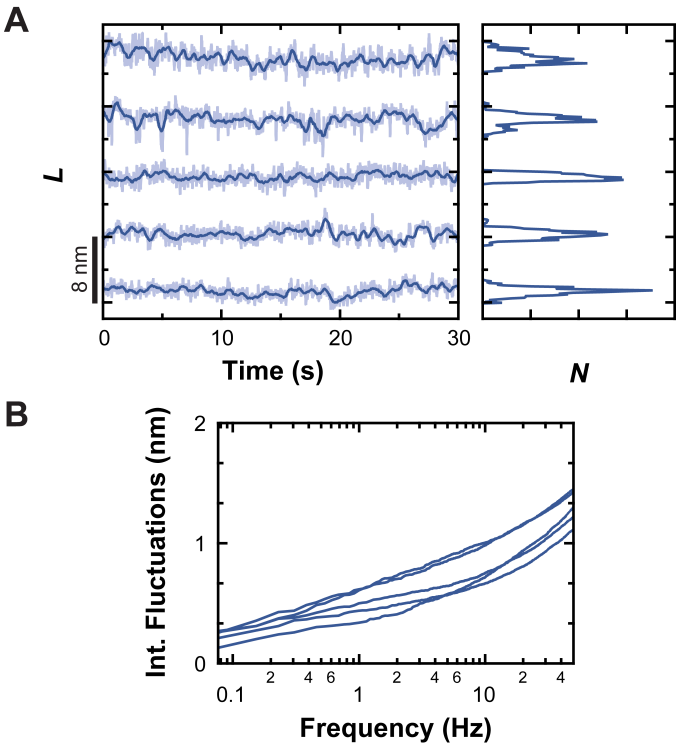

Figure C.3: Control data: RecBCD bound to blunt-ended DNA. (A) DNA contour length versus time with corresponding histograms. Data were taken at $F = 6$ pN and smoothed with a Savitzky-Golay window to 10 Hz (*light blue*) and 1 Hz (*blue*). (B) Integrated fluctuations of the records in A.

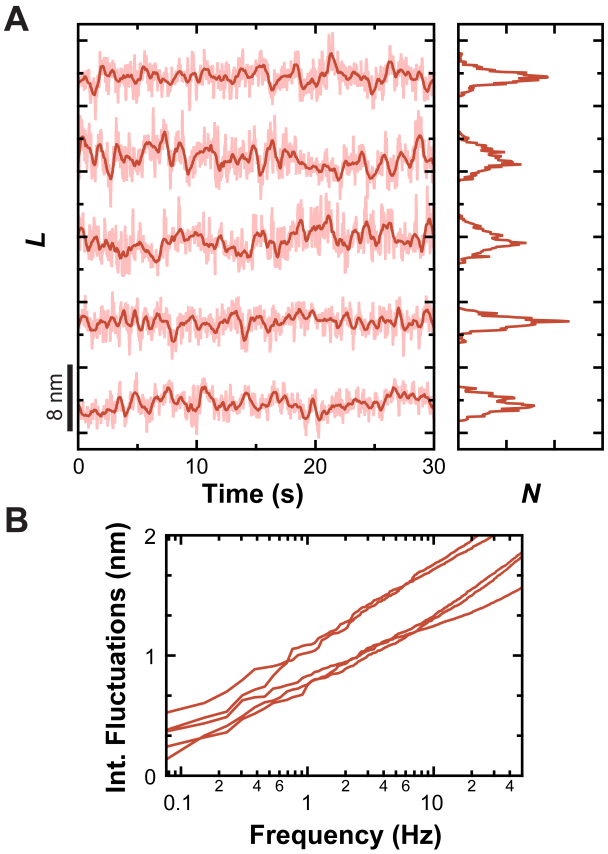

Figure C.4: Control data: RecBCD bound to partially unwound DNA in the absence of ATP. (A) DNA contour length versus time with corresponding histograms. Data were taken at $F = 6$ pN and smoothed with a Savitzky-Golay window to 10 Hz (*pink*) and 1 Hz (*red*). (B) Integrated fluctuations of the records in A.

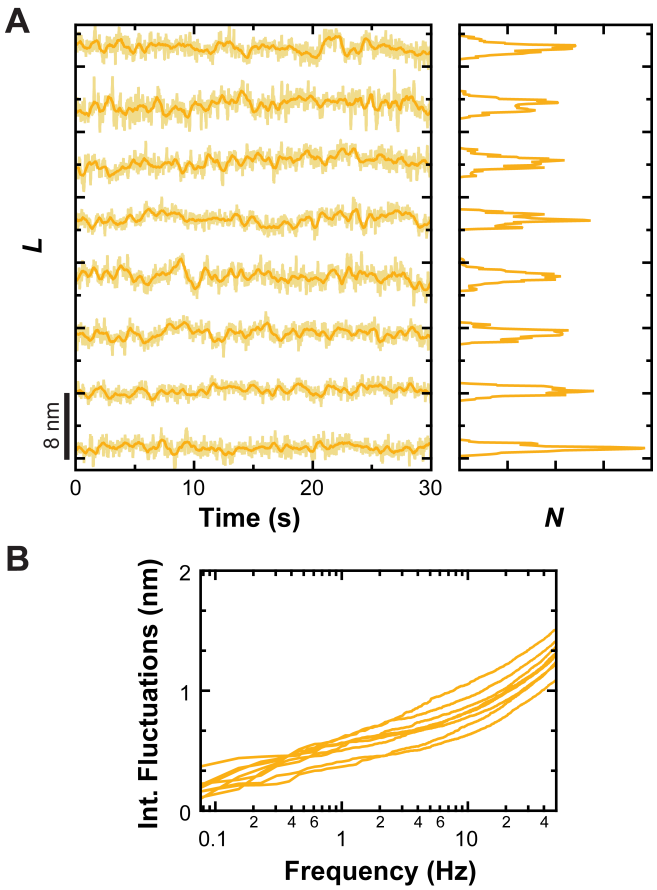

Figure C.5: RecBCD bound to 5′-$(dT)_6$-tailed DNA. (A) DNA contour length versus time with corresponding histograms. Data were taken at $F = 6$ pN and smoothed with a Savitzky-Golay window to 10 Hz (*light yellow*) and 1 Hz (*dark yellow*). (B) Integrated fluctuations of the records in A.

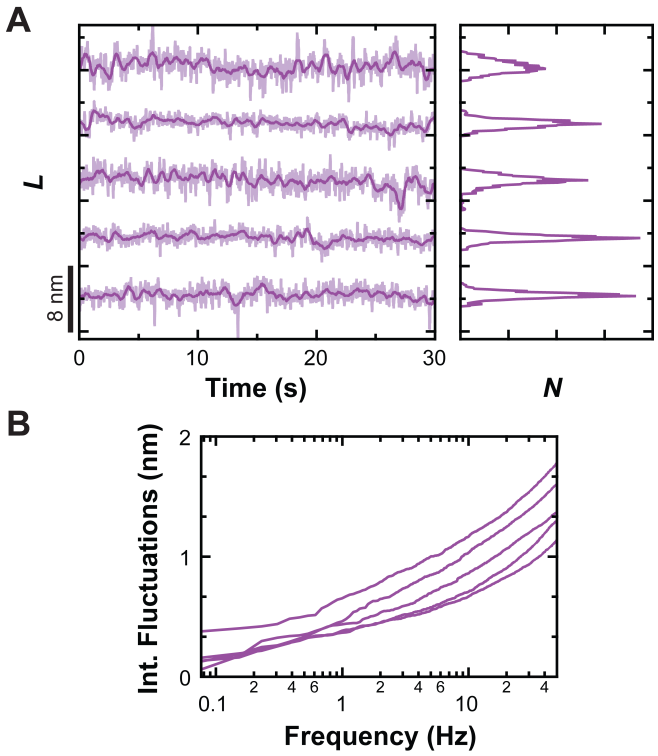

Figure C.6: RecBCD bound to 5′-$(dT)_8$-tailed DNA. (A) DNA contour length versus time with corresponding histograms. Data were taken at $F = 8$ pN and smoothed with a Savitzky-Golay window to 10 Hz (*light purple*) and 1 Hz (*deep purple*). (B) Integrated fluctuations of the records in A.

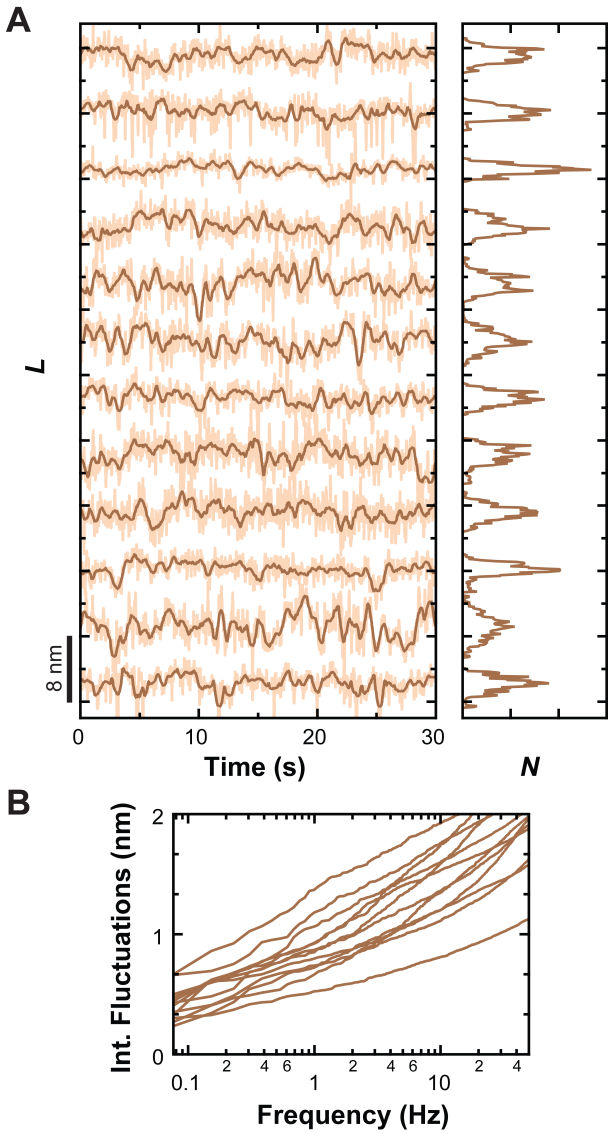

Figure C.7: RecBCD bound to 5′-$(dT)_{10}$-tailed DNA. (A) DNA contour length versus time with corresponding histograms. Data were taken at $F = 6$ pN and smoothed with a Savitzky-Golay window to 10 Hz (*light brown*) and 1 Hz (*brown*). (B) Integrated fluctuations of the records in A.

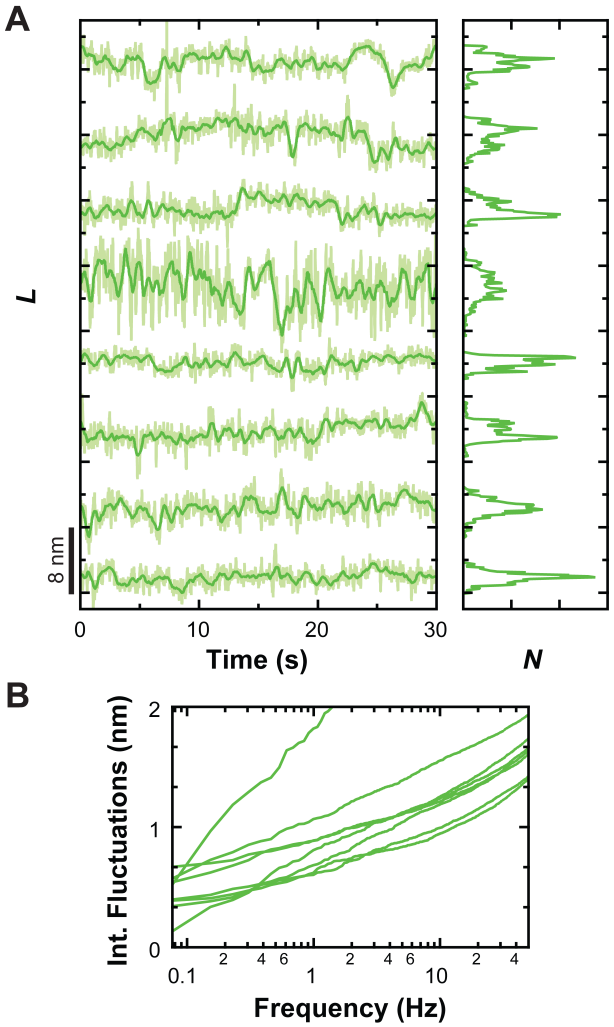

Figure C.8: RecBCD bound to 5′-$(dT)_{20}$-tailed DNA. (A) DNA contour length versus time with corresponding histograms. Data were taken at $F = 20$ pN and smoothed with a Savitzky-Golay window to 10 Hz (*light green*) and 1 Hz (*green*). (B) Integrated fluctuations of the records in A.

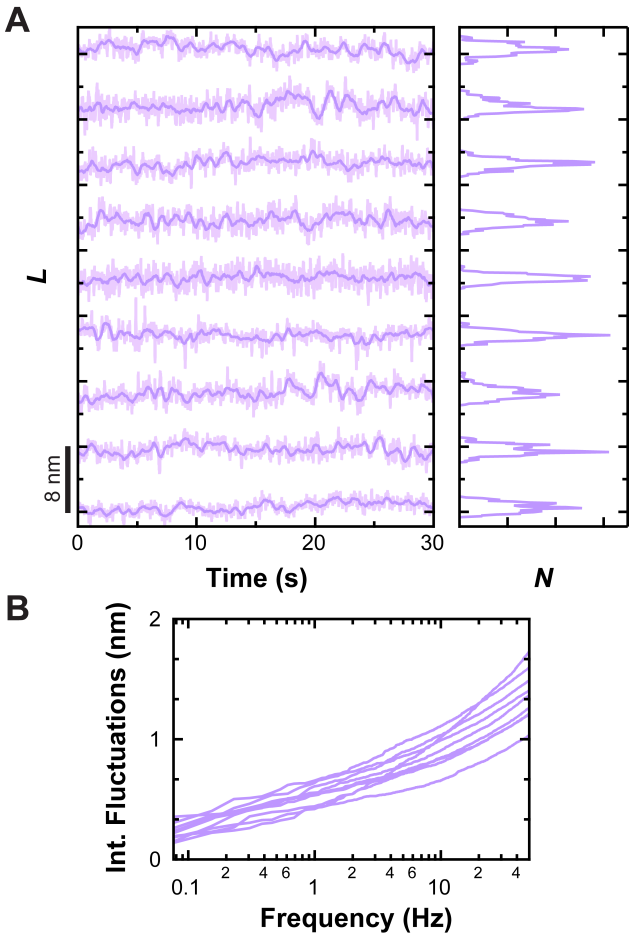

Figure C.9: RecBCD bound to 5′-$(dT)_{10}$-tailed DNA in the presence of ADP·BeF_x. (A) DNA contour length versus time with corresponding histograms. Data were taken at $F = 6$ pN and smoothed with a Savitzky-Golay window to 10 Hz (*light purple*) and 1 Hz (*purple*). (B) Integrated fluctuations of the records in A.

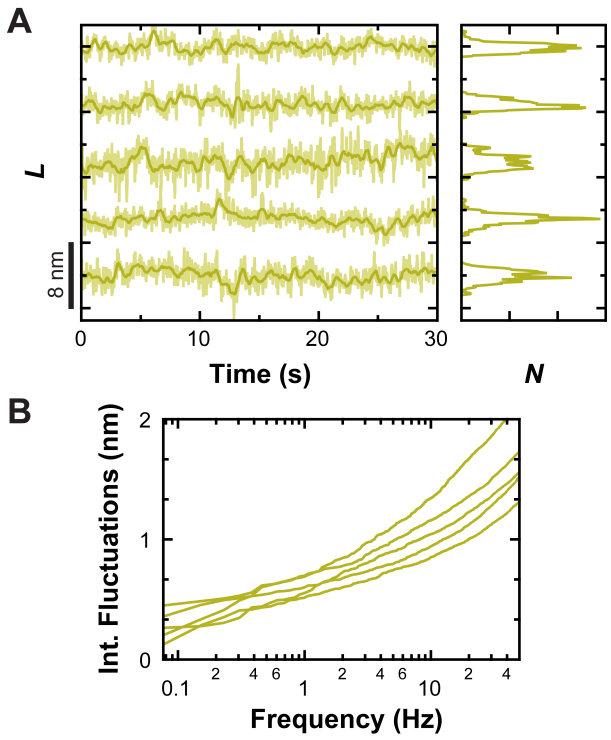

Figure C.10: RecBCD bound to 5′-$(dT)_{10}$-tailed DNA in the presence of AMPPNP. (A) DNA contour length versus time with corresponding histograms. Data were taken at $F = 6$ pN and smoothed with a Savitzky-Golay window to 10 Hz (*light yellow*) and 1 Hz (*yellow*). (B) Integrated fluctuations of the records in A.

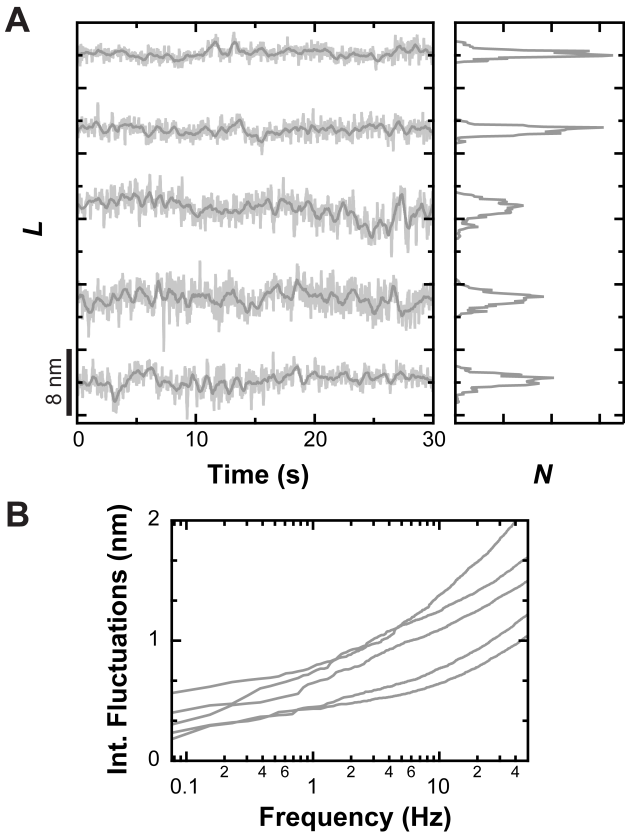

Figure C.11: RecBCD bound to 5′-$(dT)_{10}$-tailed DNA in the presence of ADP + P_i. (A) DNA contour length versus time with corresponding histograms. Data were taken at $F = 6$ pN and smoothed with a Savitzky-Golay window to 10 Hz (*light gray*) and 1 Hz (*gray*). (B) Integrated fluctuations of the records in A.

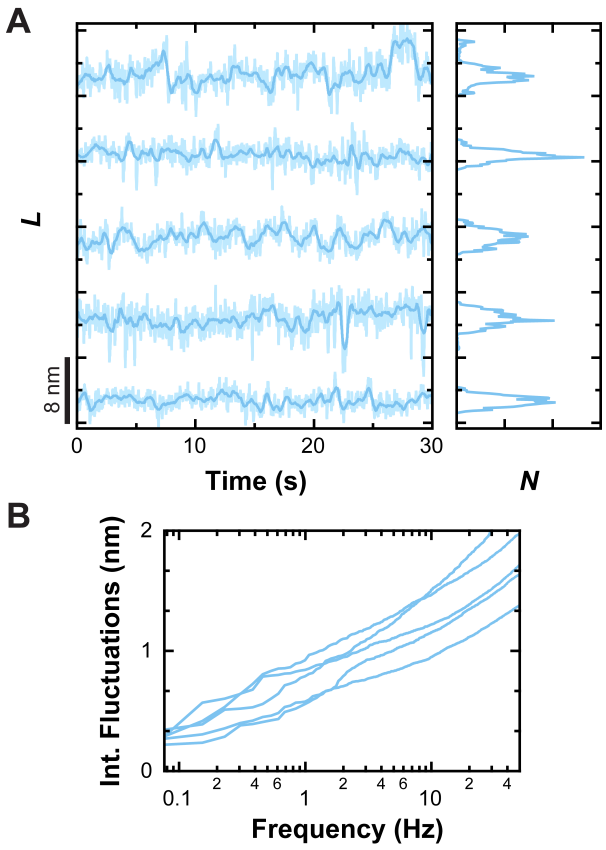

Figure C.12: RecBCD bound to 5′-$(dT)_{10}$-tailed DNA in the presence of ADP. (A) DNA contour length versus time with corresponding histograms. Data were taken at $F = 6$ pN and smoothed with a Savitzky-Golay window to 10 Hz (*light blue*) and 1 Hz (*sky blue*). (B) Integrated fluctuations of the records in A.

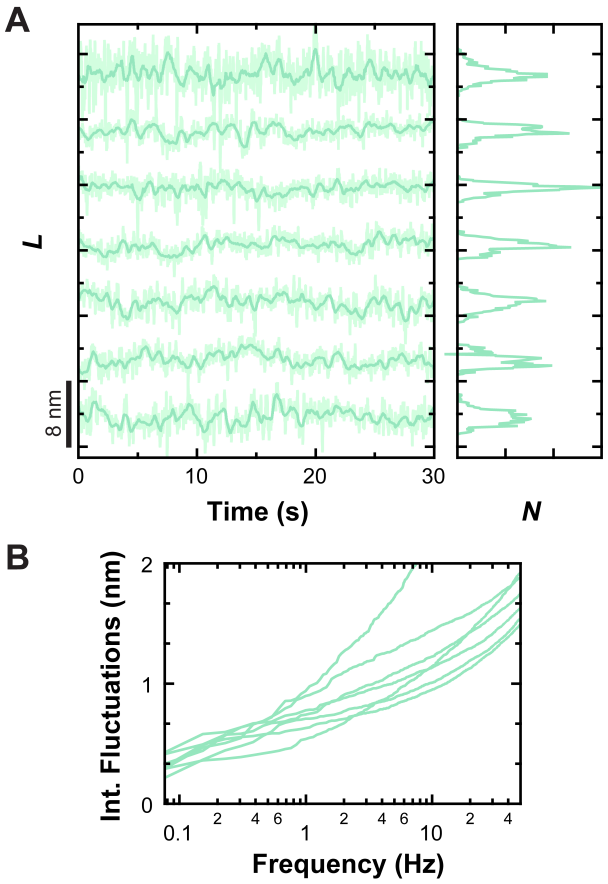

Figure C.13: RecBCD bound to 5′-$(dT)_{10}$-tailed DNA in the presence of ATPγS. (A) DNA contour length versus time with corresponding histograms. Data were taken at $F = 6$ pN and smoothed with a Savitzky-Golay window to 10 Hz (*sea green*) and 1 Hz (*teal*). (B) Integrated fluctuations of the records in A.

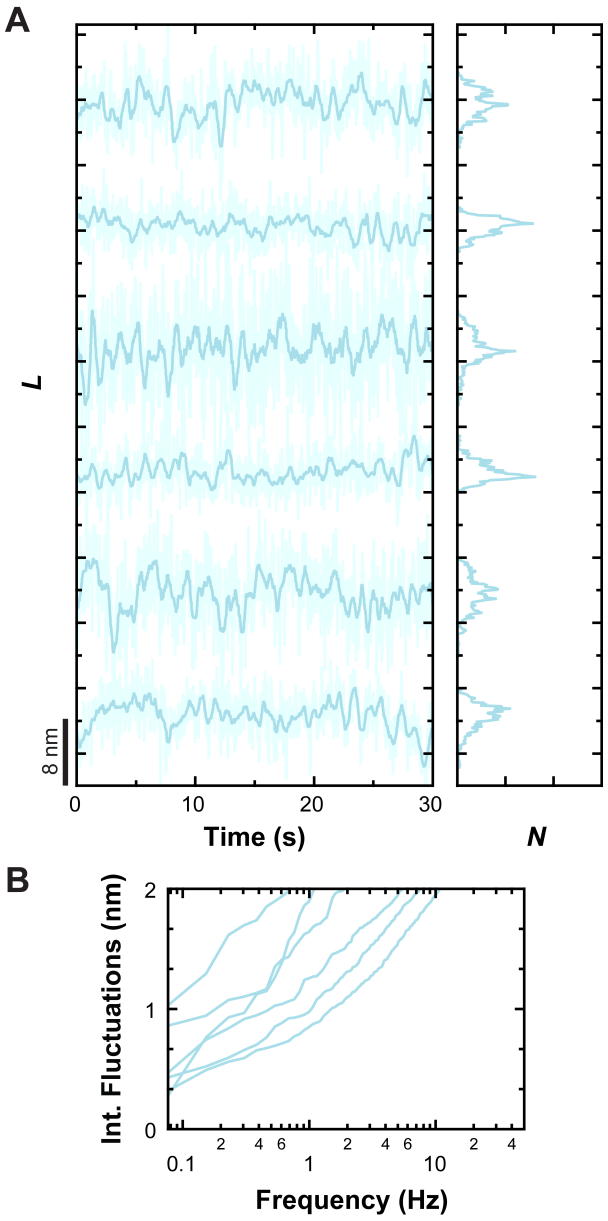

Figure C.14: RecBCD bound to AT-rich 5′-$(dT)_{10}$-tailed DNA at 2 pN. (A) DNA contour length versus time with corresponding histograms. Data were taken at $F = 2$ pN and smoothed with a Savitzky-Golay window to 10 Hz (*light blue*) and 1 Hz (*cyan*). (B) Integrated fluctuations of the records in A.

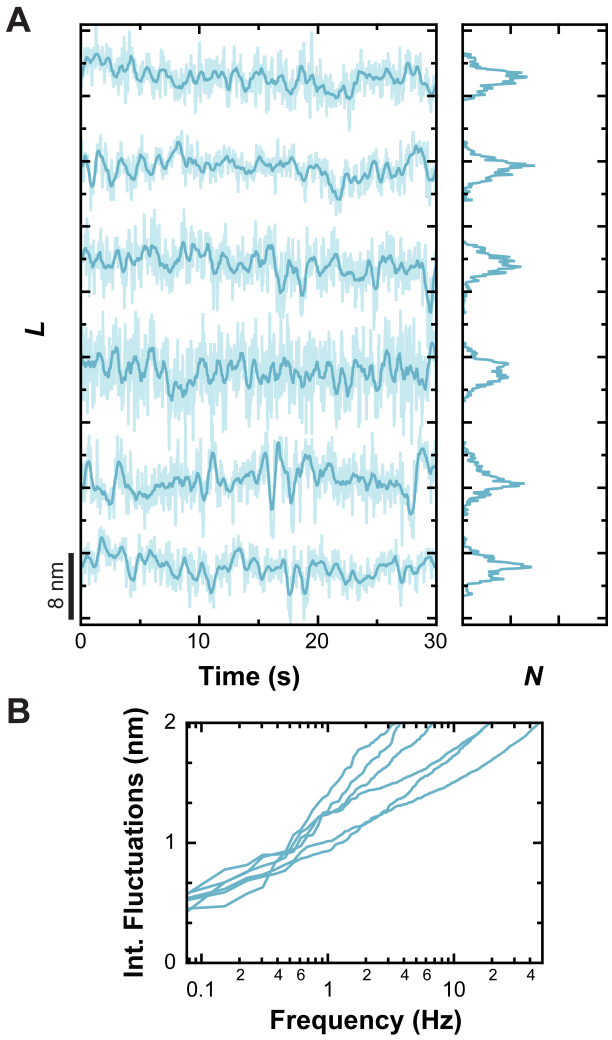

Figure C.15: RecBCD bound to AT-rich 5′-$(dT)_{10}$-tailed DNA at 4 pN. (A) DNA contour length versus time with corresponding histograms. Data were taken at $F = 4$ pN and smoothed with a Savitzky-Golay window to 10 Hz (*light blue*) and 1 Hz (*light turquoise*). (B) Integrated fluctuations of the records in A.

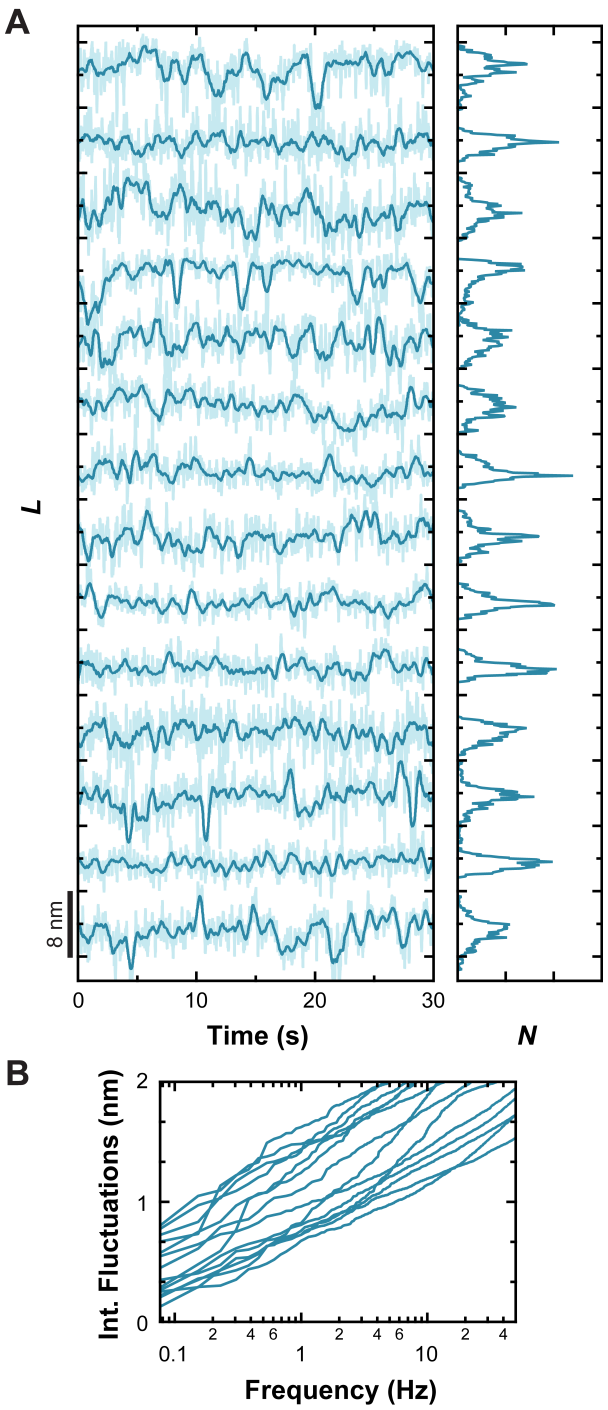

Figure C.16: RecBCD bound to AT-rich 5′-$(dT)_{10}$-tailed DNA at 6 pN. (A) DNA contour length versus time with corresponding histograms. Data were taken at $F = 6$ pN and smoothed with a Savitzky-Golay window to 10 Hz (*light blue*) and 1 Hz (*turquoise*). (B) Integrated fluctuations of the records in A.

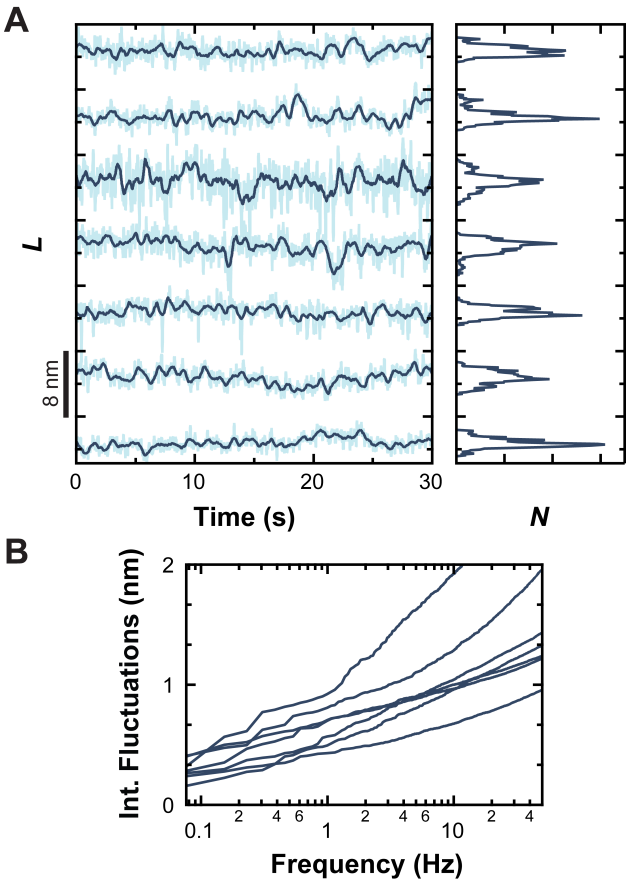

Figure C.17: RecBCD bound to AT-rich 5′-$(dT)_{10}$-tailed DNA at 10 pN. (A) DNA contour length versus time with corresponding histograms. Data were taken at $F = 10$ pN and smoothed with a Savitzky-Golay window to 10 Hz (*light blue*) and 1 Hz (*dark turquoise*). (B) Integrated fluctuations of the records in A.

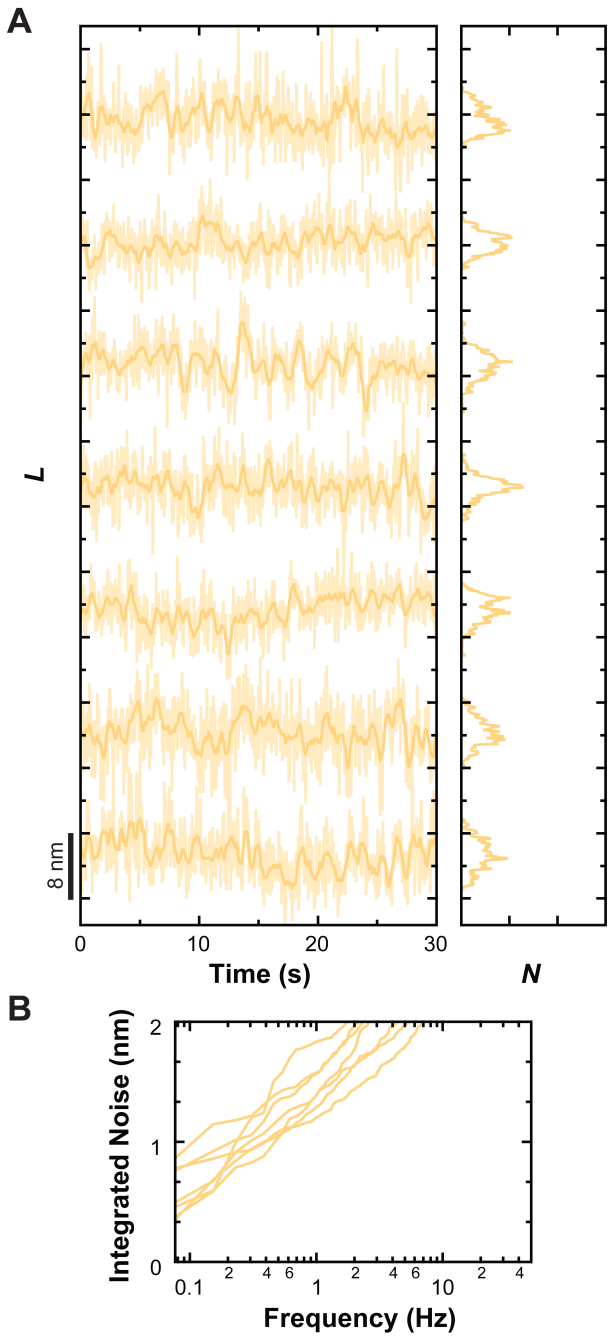

Figure C.18: RecBCD bound to mixed-sequence 5′-$(dT)_{10}$-tailed DNA at 2 pN. (A) DNA contour length versus time with corresponding histograms. Data were taken at $F = 2$ pN and smoothed with a Savitzky-Golay window to 10 Hz (*light yellow-orange*) and 1 Hz (*dark yellow-orange*). (B) Integrated fluctuations of the records in A.

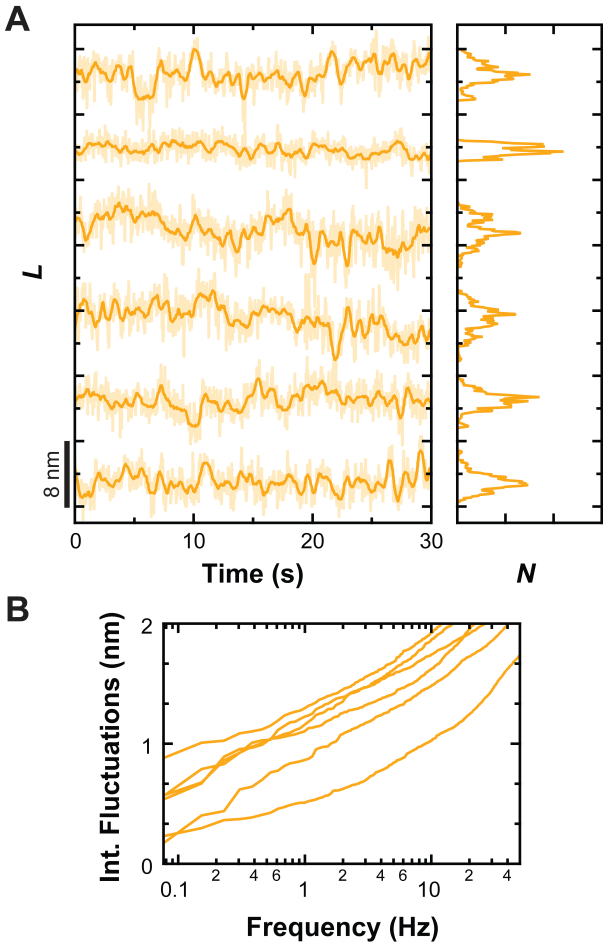

Figure C.19: RecBCD bound to mixed-sequence 5′-$(dT)_{10}$-tailed DNA at 4 pN. (A) DNA contour length versus time with corresponding histograms. Data were taken at $F = 4$ pN and smoothed with a Savitzky-Golay window to 10 Hz (*light orange*) and 1 Hz (*dark orange*). (B) Integrated fluctuations of the records in A.

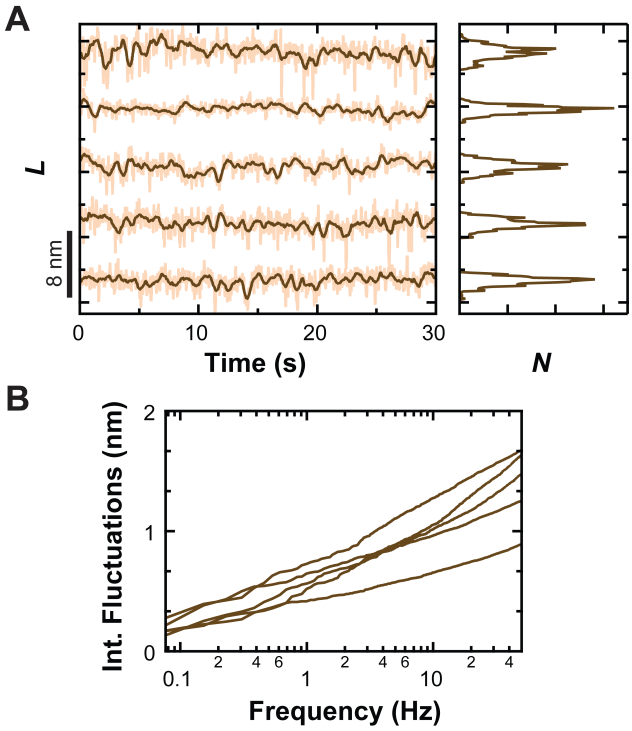

Figure C.20: RecBCD bound to mixed-sequence 5′-$(dT)_{10}$-tailed DNA at 10 pN. (A) DNA contour length versus time with corresponding histograms. Data were taken at $F = 10$ pN and smoothed with a Savitzky-Golay window to 10 Hz (*light brown*) and 1 Hz (*dark brown*). (B) Integrated fluctuations of the records in A.

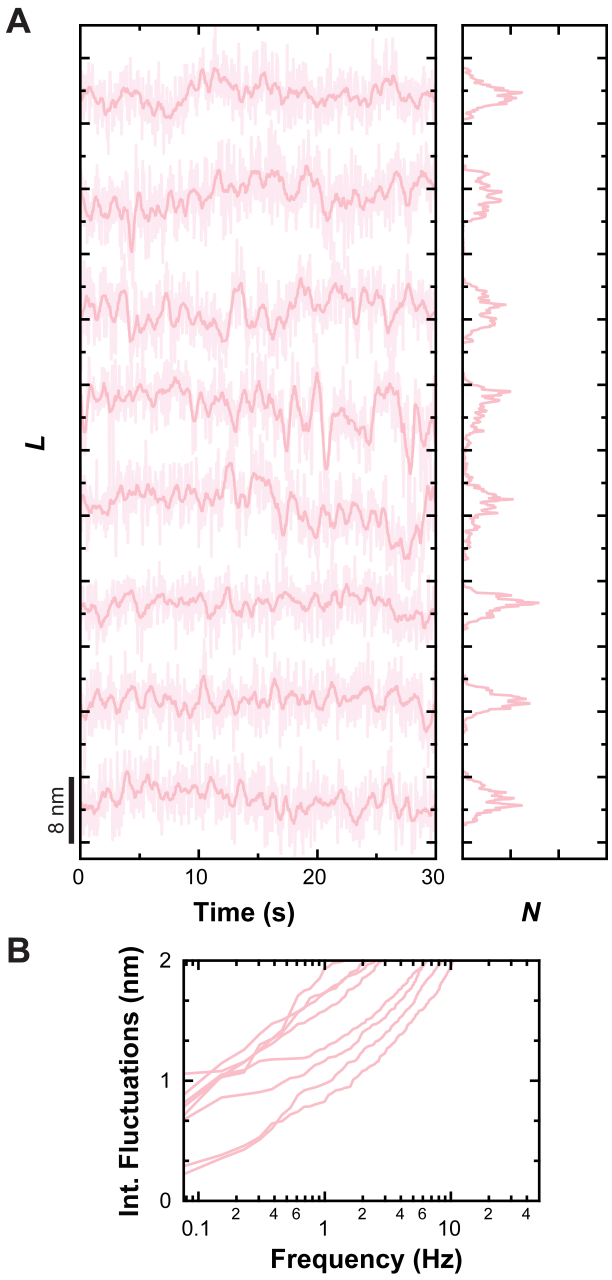

Figure C.21: RecBCD bound to GC-rich 5′-$(dT)_{10}$-tailed DNA at 2 pN. (A) DNA contour length versus time with corresponding histograms. Data were taken at $F = 2$ pN and smoothed with a Savitzky-Golay window to 10 Hz (*light rose*) and 1 Hz (*rose*). (B) Integrated fluctuations of the records in A.

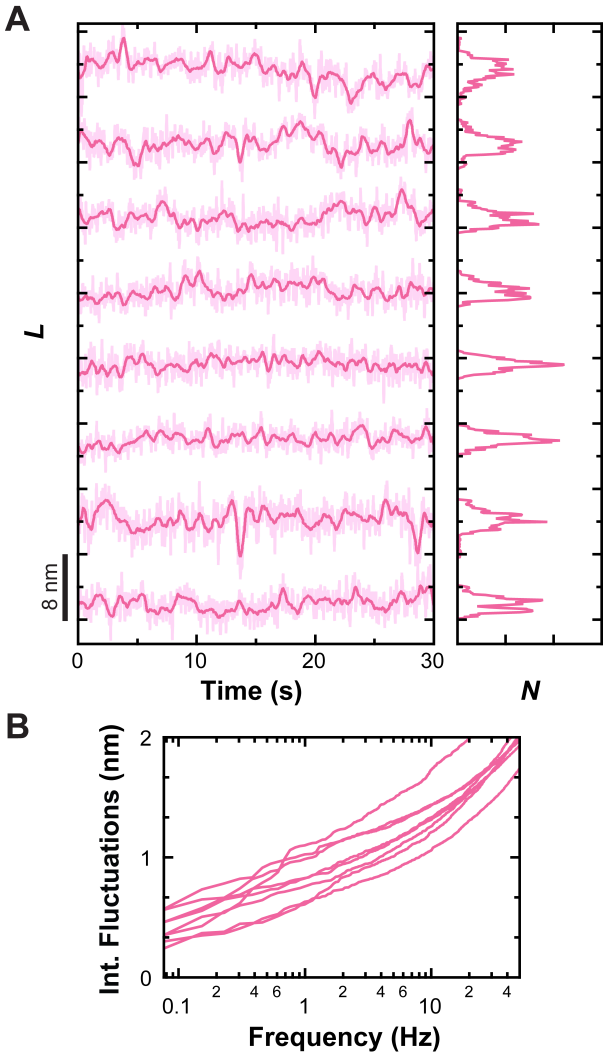

Figure C.22: RecBCD bound to GC-rich 5′-$(dT)_{10}$-tailed DNA at 4 pN. (A) DNA contour length versus time with corresponding histograms. Data were taken at $F = 4$ pN and smoothed with a Savitzky-Golay window to 10 Hz (*light pink*) and 1 Hz (*pink*). (B) Integrated fluctuations of the records in A.

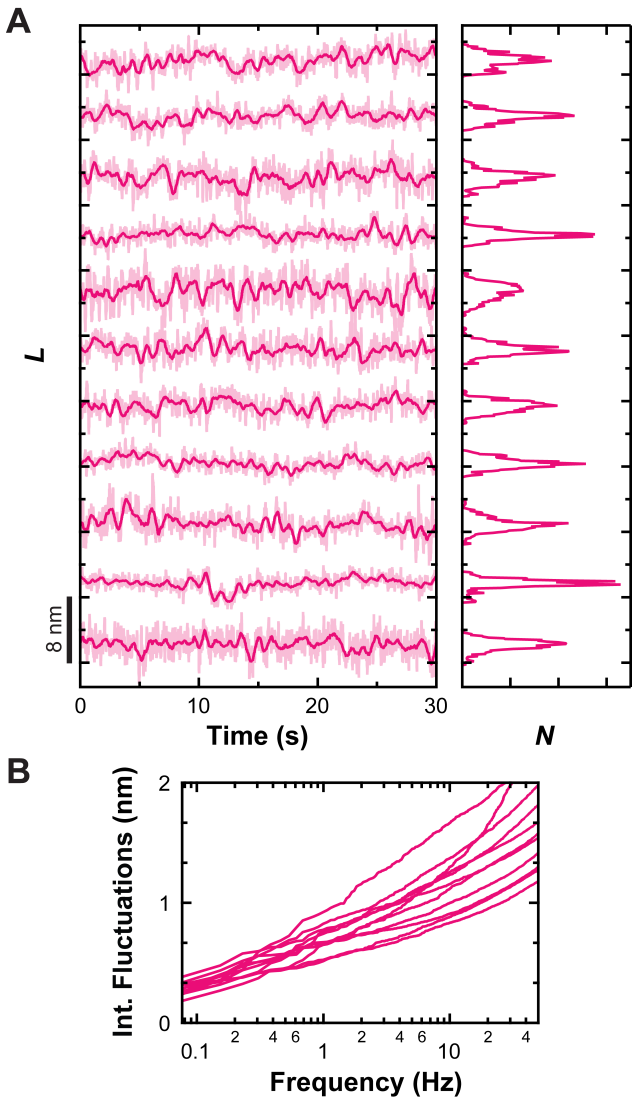

Figure C.23: RecBCD bound to GC-rich 5′-$(dT)_{10}$-tailed DNA at 6 pN. (A) DNA contour length versus time with corresponding histograms. Data were taken at $F = 6$ pN and smoothed with a Savitzky-Golay window to 10 Hz (*light pink*) and 1 Hz (*dark pink*). (B) Integrated fluctuations of the records in A.

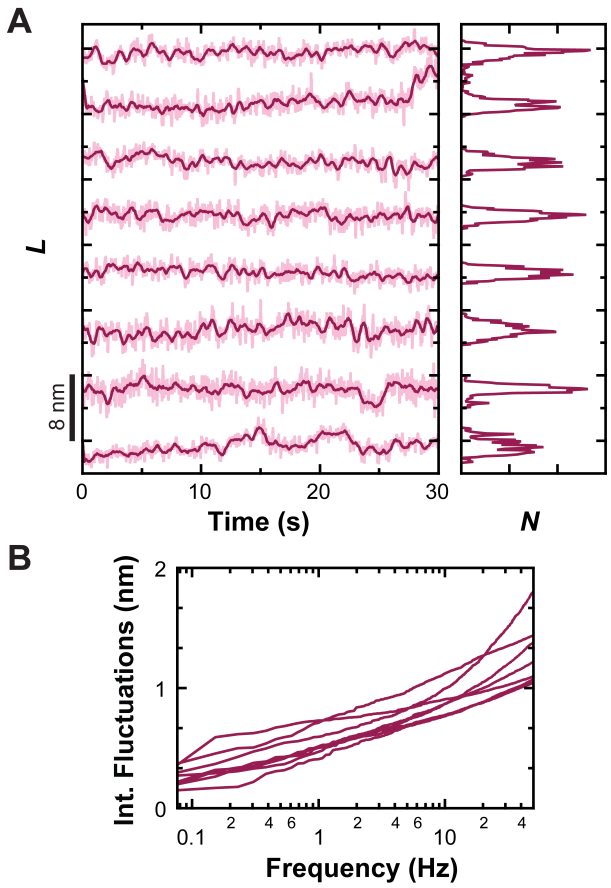

Figure C.24: RecBCD bound to GC-rich 5′-$(dT)_{10}$-tailed DNA at 10 pN. (A) DNA contour length versus time with corresponding histograms. Data were taken at $F = 10$ pN and smoothed with a Savitzky-Golay window to 10 Hz (*light magenta*) and 1 Hz (*magenta*). (B) Integrated fluctuations of the records in A.

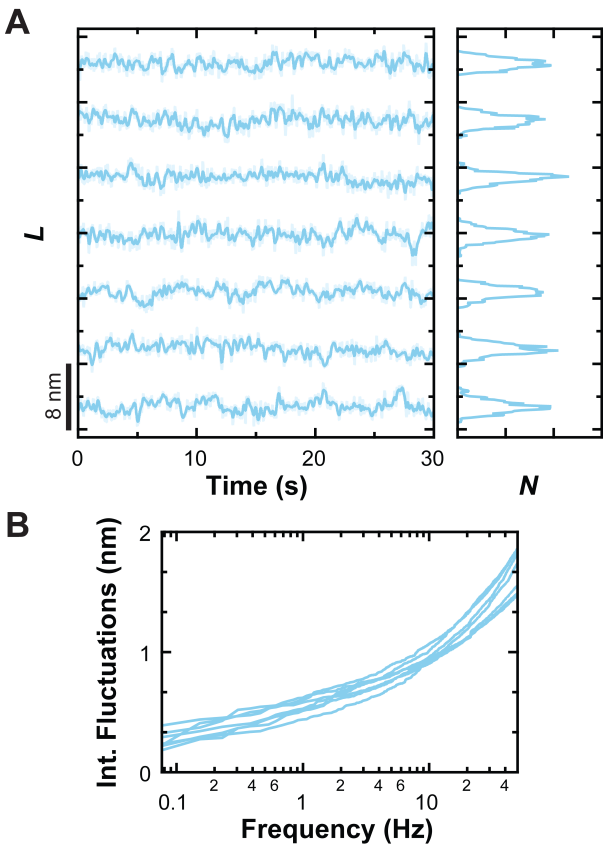

Figure C.25: RecBCD bound to AT cross-linked 5′-$(dT)_{10}$-tailed DNA. (A) DNA contour length versus time with corresponding histograms. Data were taken at $F = 6$ pN and smoothed with a Savitzky-Golay window to 10 Hz (*lighter blue*) and 1 Hz (*light blue*). (B) Integrated fluctuations of the records in A.

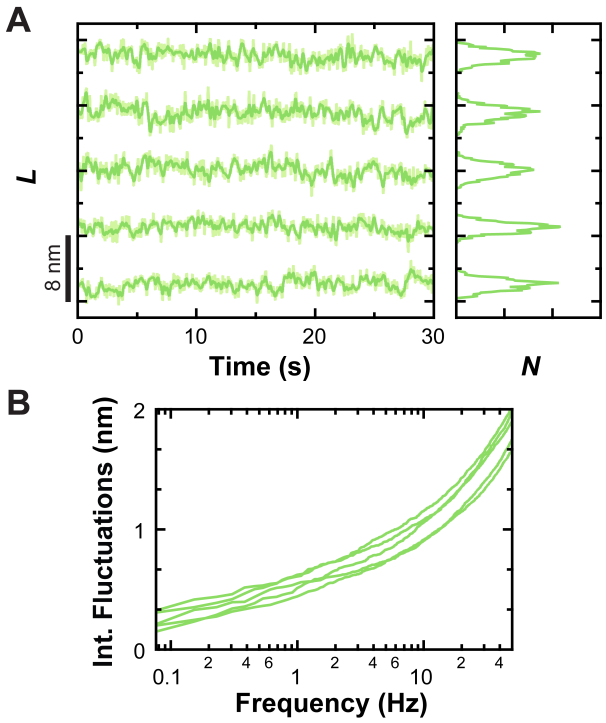

Figure C.26: RecBCD bound to GC cross-linked 5′-$(dT)_{10}$-tailed DNA. (A) DNA contour length versus time with corresponding histograms. Data were taken at $F = 6$ pN and smoothed with a Savitzky-Golay window to 10 Hz (*light green*) and 1 Hz (*green*). (B) Integrated fluctuations of the records in A.

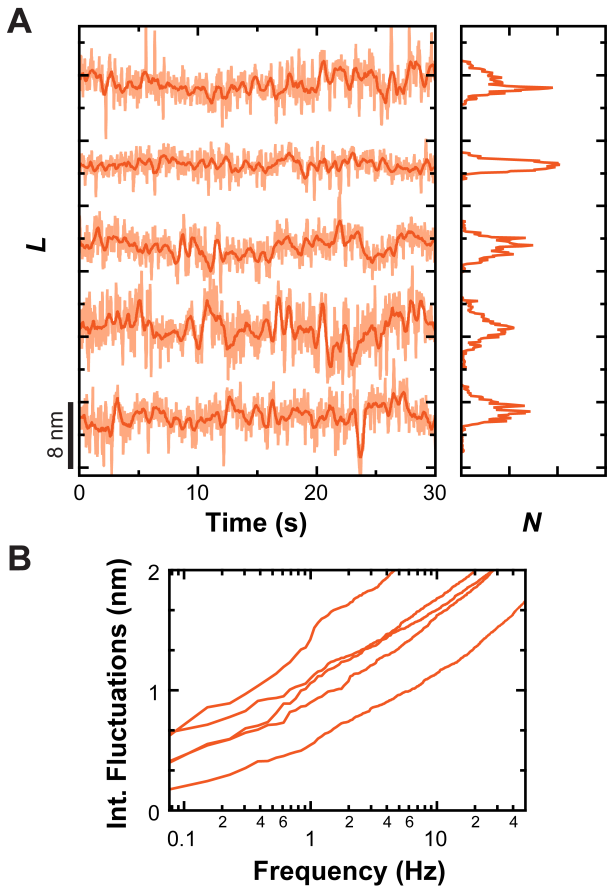

Figure C.27: RecBCD bound to Low-AT 5′-$(dT)_{10}$-tailed DNA. (A) DNA contour length versus time with corresponding histograms. Data were taken at $F = 6$ pN and smoothed with a Savitzky-Golay window to 10 Hz (*light orange*) and 1 Hz (*orange*). (B) Integrated fluctuations of the records in A.

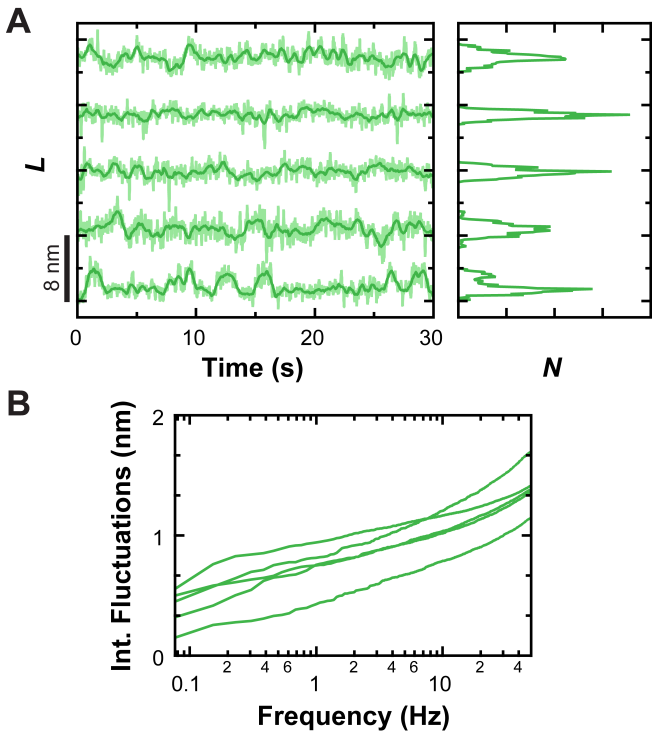

Figure C.28: RecBCD bound to Low-GC 5′-$(dT)_{10}$-tailed DNA. (A) DNA contour length versus time with corresponding histograms. Data were taken at $F = 6$ pN and smoothed with a Savitzky-Golay window to 10 Hz (*light green*) and 1 Hz (*green*). (B) Integrated fluctuations of the records in A.